A large white offshore wind turbine stands in the foreground, its three blades extending across the frame. The turbine is set against a backdrop of a vast, dark blue ocean under a cloudy, grey sky. In the distance, several other smaller wind turbines are visible on the horizon. The overall scene is a high-angle, wide shot of an offshore wind farm.

Seismic Inversion for Estimating Soil Material Damping for Offshore Wind Turbines

Matteo Ravasio

May 31, 2018

Seismic Inversion for Estimating Soil Material Damping for Offshore Wind Turbines

Master of Science Thesis

Author: Matteo Ravasio

Committee: Prof. Dr. A.V. Metrikine TU Delft - Chairman
Dr. Ir. K.N. van Dalen TU Delft
Ir. M. Armstrong Siemens Gamesa
Ir. W.G. Versteijlen TU Delft, Siemens Gamesa
Dr. Ir. D. J. Verschuur TU Delft

MAY 31, 2018

- CONFIDENTIAL -

Summary

Creating accurate engineering models for predicting the response of large structures often requires geotechnical modelling of soil behaviour. Soil material damping is an important input parameter for modelling the structural response and energy dissipation, especially for embedded and lightly damped structures, as in particular for offshore wind turbines. Non-invasive in-situ measurements like the multichannel analysis of surface waves, offer cost-effective solutions and estimations over a wider volume of soil. This research aims to demonstrate that MASW technique can be used to generate a reliable in-situ estimation of the soil damping in marine environments in the depth range of 0-30m.

A unique and high-quality dataset has been made available through a collaboration with the Norwegian Geotechnical Institute (NGI). Shear wave data are rarely available for offshore site investigations and have not been used before for a damping inversion from real surface waves measurements. Moreover, also the horizontal soil response was recorded in this measurements which allow for reducing the uncertainties of the results obtained by using the Scholte wave model. Therefore, two forward waves models are implemented in Matlab to reproduce both the in-line and cross-line measurements.

A reliable shear wave velocity profile is derived via the stiffness inversion method, after which the damping inversion is performed. A modal damping inversion method is developed and it uses a novel modified random search algorithm in order to estimate the material damping profile over depth. The attenuation coefficient is chosen as the reference parameter for the damping inversion and the misfit function for the damping inversion is defined as the normalized difference per frequency of the attenuation curves. The measured attenuation coefficient is extracted based on a modified half-power bandwidth method. The modelled attenuation curve is retrieved as the imaginary part of the complex wavenumber. The wavelet compression technique is employed to reduce the number of roots used in the inversion for both

the experimental and the theoretical curves. The identification requires solving an inverse problem with a global optimization method. To get a better understanding of the model and computational time, a combination of sensitivity studies, behaviours of the phase damping ratio curves and layer reduction were performed. Then, synthetic inversions are run to verify the validity of the proposed technique. Finally, the method is applied to the aforementioned collected data and two damping profiles (Scholte and Love models) are computed and they show good agreement in terms of both trend and magnitude.

The frequency dependence of the material damping ratio of the soil is analysed from the use of measured surface wave data. A novel technique is proposed for retrieving this relation starting from the results of the damping inversion and it shows that the material damping ratio is independent from frequency. Then, two new alternative approaches are proposed, which are based on a simplification of the traditional dependency relation. The first confirms the frequency independence of damping while, although it seems very promising, the second one cannot be tested due to computational limitations. The demonstrated frequency independence of the material damping is only valid based on the frequency ranges available in the dataset and cannot be generalized to cover all scenarios.

Preface

I would like to express my gratitude to the people who support me in this experience and help me in making this work.

First of all, I would like to thank my committee for the challenging topic and for guiding me to achieve this rewarding result. Michael, thanks for your hard work and especially for all of the meetings and the short discussions we had at your desk which have been essential for my understanding and the success of this work. Karel, thanks for being always available for explanations and discussions about the tough topics of this research. In the countless meetings we had, you gave me suggestions and deep insights in the theory which have been the backbone of my work. Pim, I would like to thank you for your fruitful supervision and for having pushed me every week to reach the 10% damping. Andrei, thanks for your expert guidance during the official meetings. Eric, thanks for the precious time you dedicated to me in our extensive meetings.

To my colleagues at Siemens Gamesa, thank you for sharing with me your knowledge and experience, for providing a professional and pleasant environment and especially for having made me crawl several and multiple times. It was my first time in a company and I hope that my future work experiences will be as stimulant and rewarding as sharing the office with you. Special gratitude to Walty, my life supervisor, who support me in every aspects at every time. Moreover, thanks to the fellow students for supporting me with discussions, beers and endless potje. Thankfulness to Corine and Ingmar for their precious works.

Immense gratitude to the friends I met during this long experience in the Netherlands, especially to Givi, la mi Marina, Lodo (lo zerbi), Walterino, Terun and Alina for your unconditioned support and for having been my family here. Sincere gratitude goes to Andrei, active part of this work having clarified my thoughts and ideas

with countless emails and calls.

Most of all, special gratitude to my Mom, my Dad, my uncle, my sister and Claudino for your strong support from distance and especially for having made all of this possible.

Matteo Ravasio
Den Haag, May 2018

Contents

Summary	i
Acknowledgements	iii
Nomenclature	ix
1 Introduction	1
1.1 Measurement techniques	2
1.1.1 Laboratory tests	3
1.1.2 Field tests	3
1.2 Review of previous work	5
1.2.1 Siemens Wind Power	5
1.2.2 First MSc at Siemens Wind Power	6
1.2.3 Second MSc at Siemens Wind Power	7
1.2.4 Third MSc at Siemens Wind Power	8
1.3 Research goal	10
1.4 Thesis outline	11
2 Theory and Derivations	13
2.1 Seismic waves	13
2.2 Elastic wave equation	16
2.2.1 Kinematic equation	17
2.2.2 Constitutive equation	18
2.2.3 Equilibrium equation	20
2.2.4 Equation of motion	21
2.3 Modal surface wave equations	21
2.3.1 Rayleigh waves	22

2.3.2	Love waves	28
2.3.3	Model comparison	31
2.4	Damping modelling	32
2.4.1	The visco-elastic model	33
2.5	Cylindrical coordinates	36
2.6	Layered model	37
2.6.1	Scholte waves	38
2.6.2	Love waves	39
3	Modal Inversion Method	41
3.1	Inversion analysis	41
3.2	Frequency-wavenumber domain	42
3.3	Modal root finding	47
3.3.1	Undamped roots	48
3.3.2	Damped roots	49
3.4	Attenuation analysis	51
3.4.1	Attenuation curve from the theoretical model	53
3.4.2	Attenuation curve identification methods from measured data	54
3.5	Damping inversion tool	58
3.5.1	Wavelet compression	60
3.5.2	Misfit function	62
3.5.3	Modal inversion algorithm	63
4	Model Studies	67
4.1	Sensitivity to stiffness	67
4.2	Sensitivity to damping	68
4.3	Time comparison	70
4.4	Merging layers	72
4.5	Synthetic inversions	74
4.5.1	Synthetic inversion: reduced frequency range	80
4.6	Understanding phase damping ratio curves	81
4.7	Conclusions on model studies	83
5	Stiffness Inversion	87
5.1	Gjøa dataset	87
5.2	Love wave model	88
5.2.1	Comparison of the stiffness profiles	90
5.3	Reduced profile	91
5.3.1	Scholte waves	93

5.3.2	Love waves	94
5.4	Conclusions on the stiffness inversion	95
6	Damping Inversion	97
6.1	Gjøa dataset: collection and processing	97
6.2	Gjøa damping inversion	103
6.2.1	Measured attenuation curve	103
6.3	Scholte waves inversion	105
6.4	Love waves inversion	108
6.5	Overestimation of the material damping	111
6.6	Conclusions on the damping inversion	114
7	Frequency Dependence of Damping	119
7.1	Background	119
7.2	Novel technique	120
7.3	Two alternative techniques	122
7.3.1	One parameter approach	123
7.3.2	Two parameters approach	124
7.4	Conclusions on frequency dependence of damping	125
8	Conclusions and Recommendations	127
8.1	Conclusions	127
8.2	Recommendations	129
A	Hysteretic Behaviour of a Visco-Elastic Material	133
B	Bessel Functions and Hankel Transform	135
B.1	Vertical displacement	136
B.2	Transversal displacement	137
C	Rectangular Windowing	139

Nomenclature

Latin symbols

$A(\omega)$	Measured attenuation curve	m^{-1}
c	Velocity	ms^{-1}
C_p	Pressure or P-wave velocity	ms^{-1}
C_s	Shear or S-wave velocity	ms^{-1}
c_R	Rayleigh wave velocity	ms^{-1}
c_S	Scholte wave velocity	ms^{-1}
c_{phase}	Wave phase velocity	ms^{-1}
c_{group}	Wave group velocity	ms^{-1}
D_p	Pressure material phase damping ratio	
D_s	Shear material phase damping ratio	
E	Elastic modulus	Nm^2
f	Frequency	Hz
\bar{f}	External force	
G	Shear modulus	Nm^{-2}
H_{zz}	Transfer function for vertical load	
$H(x)$	Heaviside function	
i	Imaginary	
J_v	Bessel function of order v	
K	Bulk modulus	Nm^{-2}
M	Coefficient matrix	
Q	Quality factor	
S_{uu}	Response spectrum	

s	Slowness	$m^{-1}s$
u	Displacement	m
t	Time	s
W	Energy	Nm
x	Scalar notation for x	
\bar{x}	Vector notation for x	
x_{ij}	Element (i,j) of the matrix X	
$x_{i,j}$	Vector x component i, derivative wrt j	
\tilde{x}	x transformed with Fourier transform	
x^{H_0}	x transformed with Hankel transform	

Greek symbols

α	Theoretical attenuation coefficient	m^{-1}
γ	Shear Strain	
δ_{ij}	Kronecker Delta	
ϵ	Strain	
ϵ	Misfit error	
ζ	Material damping	
η_p	Pressure material damping ratio	
η_s	Shear material damping ratio	
κ	Wavenumber	m^{-1}
κ^*	Complex wavenumber	
κ_{RE}	Real part of the wavenumber	
κ_{IM}	Imaginary part of the wavenumber	
λ	Lamé's first constant	Nm^{-2}
λ	Wavelength	m
μ	Shear modulus, Lamé's second constant	Nm^{-2}
ν	Poisson ratio	
ρ	Density	kgm^{-3}
σ	Stress	Nm^{-2}
τ	Shear stress	Nm^{-2}
Φ	Phase	
ϕ	Elastic dilational potential	m^2s^{-1}
ψ	Elastic rotational potential	m^2s^{-1}
ω	Circular frequency	$rads^{-1}$

Abbreviations

CG	Conjugate gradient minimization
CPT	Cone penetration test
DFT	Discrete Fourier Transform
DHT	Discrete Hankel Transform
ECK	Equilibrium-Constitutive-Kinetic
EOM	Equation of Motion
FD	Finite Difference
FFT	Fast Fourier Transform
F-K	Frequency-Wavenumber
LCoE	Levelized Cost of Energy
MASW	Multi-channel analysis of surface waves
N_{gen}	Number of generations in genetic inversion
N_{Pop}	Number of candidates in genetic population
N_{Dad}	Number of parents in genetic population
N_{Con}	Number of contestants in genetic population
N_{iter}	Number of iteration
N_{memb}	Number of members of the population
N_{soil}	Number of soil layers
NR	Non-resonance
NGI	Norwegian Geotechnical Institute
ODE	Ordinary Differential Equation
OWT	Offshore Wind Turbines
P-wave	Pressure wave
pFM	Probability of full mutation
PDE	Partial Differential Equation
RC	Resonant Column
RMS	Root Mean Square
SASW	Spectral Analysis of Surface Waves
S-wave	Shear wave
SGRE	Siemens Gamesa Renewable Energy
SH	Shear horizontally polarized
SV	Shear vertically polarized
SSI	Soil-Structure Interaction
TC	Tests Case
ZEAL	ZERos if AnaLYtic functions

Chapter 1

Introduction

Wind is the engine of climate on our planet. Due to the different pressure of the atmospheric gasses caused by the radiation of Sun, wind blows everywhere on the Earth with different intensity and duration. Wind energy has been used by humans since ancient times for several applications such as sailing or windmills. Nowadays, kinetic energy carried by wind is transformed into electrical energy by wind turbines which are usually clustered in wind farms. In the last decades, renewable energy has developed greatly and wind energy occupies a central role in this process and it is estimated that the wind energy production will increase from less than 1 trillion kilowatt-hours in 2015 to 2.5 trillion kilowatt-hours in 2040 [2]. At the end of 2015, the wind power generation capacity in the world has reached 435 GW and it has been developed in more than 100 countries meeting about 7% of the electricity requirements of our planet. The offshore wind energy production is more than 12 GW with 73 wind farms in 15 countries and more than 92% of all offshore wind installations are in European waters [12]. Actually, the goal of the “green” wind power companies is to reduce the costs in order to compete with the fossil fuels energy production which, nowadays, represent around 70% of the energy production [2] and contributes the most to the emission of harmful greenhouse gasses.

In the Green Deal Offshore Wind in 2011, the government and the market participants in the Netherlands agreed upon a 40% cost reduction target by 2020. The study of the TKI Wind op Zee [32] shows that the support structure could account to 8.7% Levelized Cost of Energy (LCoE) reduction. In particular, improving the knowledge and the modelling technique of the soil-structure interaction (SSI) and an integrated design of the tower and the foundation could save a considerably amount of steel used for the structure and contribute respectively to 1.1% and 1.7%

LCoE reduction.

The proposed research will be focused on the estimation of dynamic parameters of soil in order to get an effective reduction of the LCoE for offshore wind turbines (OWT). The overall goal of the thesis is to develop reliable methods which are able to estimate the soil damping profile in the depth range of 0-30m by using Multi-Channel Analysis of Surface Wave (MASW), a non-invasive technique with which is possible to investigate the soil parameters over the measurement area. Damping represents a key parameter for offshore monopile turbines which are structurally poorly damped because of their slenderness. In the current design, structural and soil damping is combined in a single conservative value obtained by heavily empirical methods. Therefore, a reliable estimation of the damping profile which reduces the uncertainty could have a beneficial impact on the current design approach.

1.1 Measurement techniques

This section is inspired by Chapter 6 of the book Geotechnical Earthquake Engineering by S.L.Kramer [21] and Chapter 4 and 5 of the book Soil Behaviour in Earthquake Geotechnics by K. Ishihara [18]

A large variety of laboratory and field tests are available in order to estimate the dynamic soil properties, each of them presents advantages and limitations. The choice of the suitable method requires a deep understanding of their characteristics and a careful analysis of the specific problem at hand. Stiffness and damping are considered to be the most important among the soil properties since they influence greatly the wave propagation; the other properties, such as density and Poisson's ratio, have less variability and affect less the results. The estimation of soil properties is affected by inevitable uncertainty. This can be attributed to several factors: the intrinsic variability of soils, intrinsic anisotropy, test anisotropy, sampling, inadequate test equipment and testing errors. The uncertainties should be carefully evaluated in order to give a better estimation of the properties.

The measurement techniques can be classified based on the strain regime reached: most of the field tests work in the small-strain regime whilst laboratory tests usually work in large-strain conditions. Soil exhibits nonlinear behaviour depending on the strain level, therefore it is important to choose the right test to characterize the theoretical model at the actual loading conditions. In this section, the discussion is focused on the tests which determine the properties of soil at low-strain level since this will be the approach applied in this work as explained in Chapter 2.

1.1.1 Laboratory tests

Laboratory tests are usually performed on small specimens which are assumed to be representative for a larger body of soil. This kind of test is able to provide accurate results if the initial in-situ and the loading conditions are known and well replicated. Unfortunately, no test can be represented for all the stress path and direction; the choice of the test depends on the property which has to be estimated and so, in order to have a general characterization of the problem, different test has to be performed. Moreover, laboratory tests are costly to conduct and subjected to sampling disturbance.

Low strain level tests include Resonant Column Test, Ultrasonic Pulse Test, Piezo-electric Bender Element Test. High strain level tests include Cyclic Triaxial Test, Cyclic Direct Simple Shear Test, Cyclic Torsional Shear Test. Finally, model tests can be useful to reproduce, in laboratory, the boundary conditions of a particular problem subjected to cyclic loading. These include Shaking Table Test and Centrifuge Test. No further discussion will be dedicated to laboratory tests since they are not relevant for the present work.

1.1.2 Field tests

Field tests allow the dynamic properties to be measured in situ, which means that they are affected by the existing conditions of the specific location. Field test are considered to be highly representative for soil investigation since they do not required sampling and the results are referred in average to large volumes of material rather than the laboratory tests which consider small specimens. On the other side, as mentioned, the actual conditions have a significant influence on the test and the "noise" created by them is not easily determinable. Tests which require drilling of boreholes are more expensive but need less post processing with respect to the surface tests which are cheaper and quicker to performed but they require a deeper interpretation of the results.

Low strain level tests include Seismic Reflection Test, Seismic Refraction Test, Suspension Logging Test, Seismic Cone Penetration Test, Spectral Analysis of Surface Waves. High strain level tests include Standard Penetration Test, Cone Penetration Test, Dilatometer Test, Pressuremeter Test.

MASW: Multichannel Analysis of Surface Waves

In this work, MASW setup (also referred to as Spectral Analyses of Surface Waves (SASW)) is used in order to estimated the dynamic soil properties of the soil. This

method is a seismic survey method for investigating the shallow layers (0-30 m range) of the ground which utilizes the dispersive properties of the surface waves in vertically non homogeneous media to evaluate dynamic properties. With respect to conventional seismic method, the present technique deals with low frequency content (e.g. 5-50 Hz).

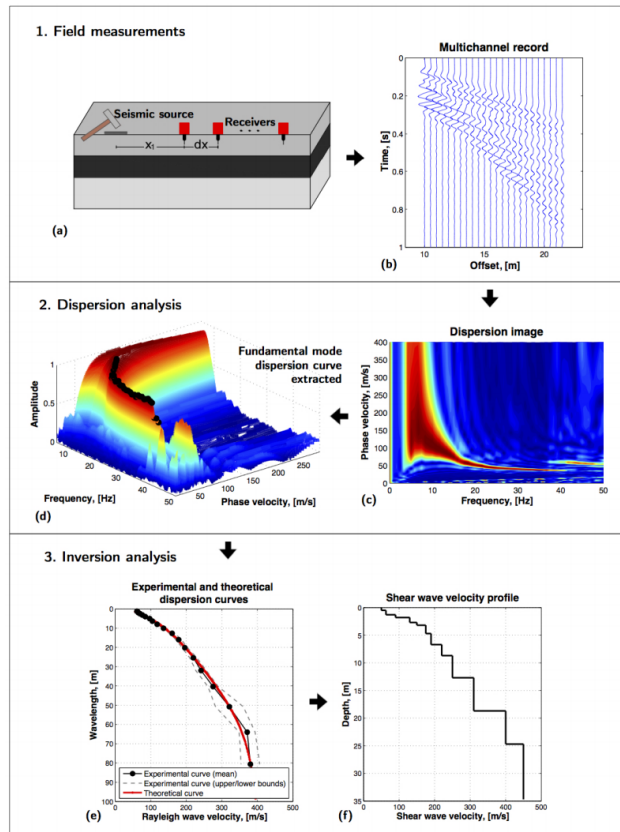


Figure 1.1: Overview of the MASW method [23].

This method was first introduced by Park et al. [33] and it is mainly made of three steps: acquisition of data, dispersion analysis and inversion analysis. First, in active MASW, the data are acquired on site by using receivers (geophones or hydrophones) which are lined up with a regular offset and register a vertical or an horizontal dis-

placement induced by propagating surface waves (Rayleigh, Scholte or Love waves) generated by an impulsive or a vibrating seismic source. The data obtained in the space-time domain are transformed in a different domain in order to highlight the dispersive properties of this measurements. The recorded signals can be converted for example in the phase velocity-frequency domain or in the wavenumber-frequency domain. The tricky part of this method is the post-processing of the data: the inversion analysis. It aims to give an accurate estimation of the shear wave velocity or the material damping ratio profile. The theoretical dispersion curve is obtained from a forward model where a certain amount of parameters is varied iteratively in order to get the best match between the measured dispersion curve and the forward model curve. The inversion analysis will be deeply discussed in Chapter 3. In Figure 1.1, a complete overview of the method is shown. With respect to SASW, in MASW, the noise source can be easily identify and filtered out in order to increase the accuracy of the data. Moreover, MASW can provide deeper investigation since this method can reach depth around 30m which is 10m more than SASW can achieve. Finally, MASW gives the possibility of including multimodal dispersion characteristics to the analysis.

1.2 Review of previous work

1.2.1 Siemens Wind Power

Siemens Wind Power, now Siemens Gamesa Renewable Energy (SGRE), is the leading company in the Offshore Wind Turbines Market in Europe (67.8% in 2016 [11]) and it has more than 25 years of experience. With over 2100 turbines installed offshore, it can provide a total capacity of roughly 7.3GW [3] offering sustainable and long-term solution for offshore wind power project. The company has participated in projects well known all over the world for capacity and greatness such as London Array (the largest wind farm in the world), DanTysk and Gemini.

The future goal of the company is to reduce the cost for offshore wind. Therefore, Siemens Wind Power is investing in this project in order to get an effective cost reduction in the pre-design phase of the production of the OWT.

This project will be built on the three previous MSc theses developed at Siemens Wind Power in The Hague and it aims to integrate and develop these works to improve the estimates of the dynamic properties of layered soils and use them to study the Soil-Structure Interaction (SSI) for OWT applications. The previous projects are briefly presented below.

1.2.2 First MSc at Siemens Wind Power

Corine de Winter [13] based her thesis on finding the best measurement set up for deriving information on dynamic soil properties and the best way to extract these properties from the measured data.

First, she presented the theoretical modelling of wave propagation through soil. Then, she applied Finite Difference Method (FDM) to evaluate different source-receiver combinations. Active and passive sources have been tested combining them with vertical and horizontal receiver arrays. It turned out that vertical arrays are practically difficult to install while horizontal arrays are able to measure the geometric dispersion which is sensitive to the subsurface stratification, so then, horizontal arrays are preferable. Moreover, passive sources are less attractive than active sources because of lack of information about the source. From this comparison, she concluded that the best setup is composed by a horizontal array with an active source. Secondly, she compared three types of forward methods (finite difference method, modal surface wave method, full waveform method). Full waveform (FW) method is recommended by Corine because it is suitable for automating the inversion method. Modal surface wave (MSW) method requires manual and expert mode-picking ability and the obtained response spectrum is discrete. In Finite difference (FD) method, the discretization plays an important role and the match with the analytical models is not guarantee.

In the second part of the thesis, the inversion problem is presented. Both FW and MSW method are used for the inversion and compared with each other. For the first method, the suitability is related to the correlation between the 2D response spectra; for the second method, the suitability function is related to the distance, along lines with constant frequency, between the theoretical and the measured dispersion curves. Some tests on sensitivity analysis are performed and it turned out that p-wave velocity has a small influence on the suitability and the shear wave velocity has the major impact on the shallow layers. Then, two inversion methods are presented: a conjugate gradient (CG) method and a genetic algorithm. The first one works well if the initial guess is close to the global minimum, while the second one is a global optimization method and it has been used in the subsequent analyses. She also suggested the possibility of implementing the CG after the genetic algorithm, since CG find the minimum quicker once close to the global one. Applying the inversion method for both FW and MSW, good results are obtained for a synthetic layered soil; moreover, Corine found that the error for MSW is higher probably because of the discrete nature of its suitability function. The Influence of background properties is tested performing several inversions changing the different properties separately. She found that density, layer thickness and p-wave velocity do have an impact on

the inversion process, however, more inversion tests are needed for generalizing the results. Additionally, some modelling experiments were performed to find the minimum contrast this method is able to invert for. After these tests, Corine concludes that shallowest layers have the largest impact on dispersion during the inversion because they are reached by all the wave while deeper layers are involved only for large wavelengths. Furthermore, a 5% uncertainty of the a-priori soil properties results in a maximum error of 12% and most of the results are acceptable because they have an error smaller than 5%.

Finally, Corine used finite difference method to produce synthetic measurements to invert. Adding intermediate layers and post-processing of the data are operations needed to improve the results of the FD method. The results obtained are not as good as the theoretical algorithm is able to yield, but the profile and the important contrasts are retrieved.

1.2.3 Second MSc at Siemens Wind Power

Ingmar Bolderink [8], basing his thesis on Corines work, applied the full waveform inversion method to the measured data from the IJsselmeer, the Netherlands.

First, he adapted the suitability function in order to make it source independent. A stabilization factor has been introduced and the objective function becomes more source independent with decreasing the factor itself. Moreover, the consequences of the truncation in the space-time domain are taken into account by applying windowing to the FFT algorithm which has been preferred with respect to a convolution algorithm because it resulted to be faster. Subsequently, synthetic inversions are performed for P- and S-wave velocity and they showed quite good results.

In the second part, in-situ measurements from IJsselmeer are considered. Measurements have been done by using 48 receivers spacing 1 m and five subsequent shots have been performed spacing 45m moving the source away from the receivers (hydrophones) in order to concatenate the shots and get a higher spatial resolution. At the end, it turned out that the streamer had a 15 degrees angle with respect to the line of the shots; locations were aligned by using direct arrival time of the pressure wave in water. Concatenation of the datasets required a mixed linear and parabolic Radon transform; in addition, noise was pushed out of the data as well. Moreover, the shot record has been scaled with RMS scaling in order to decrease the influence of the near field effects with respect to the far field ones. The dataset was also windowed by applying a Hanning window to decrease the sidelobing which results in a decrease of the spatial resolution and an increase of the influence of the first 16 traces among the first and last 100 traces. Finally, the visible response spectrum was limited up to 35 Hz and 0.1 m^{-1} .

In the last part of the thesis, the full waveform inversion of in-situ seismic data is performed. First, an initial model of the soil (8 layers and a halfspace) is estimated based on the CPT measurements performed by Fugro. To be consistent, the same windowing and scaling is applied to the modelled data. Some sensitivity runs are performed in order to find the influence of the number of layers and the amount of damping. In order to get the higher modes of the surface waves, the velocity of the halfspace is set at a high value. In the first runs, the results were not satisfactory and low values of the suitability function are found. By increasing the range of possibilities in the lower layers, the results were still not good. Finally, the best run was performed by increasing the velocity in the middle layers; the results showed a value of the suitability equal to 0.49 although the modelled response spectrum was visually quite different from the measured one. In conclusion, the high influence of damping was thought to be the cause of the big differences in the spectra and the full waveform method was stated to be a computationally expensive method.

1.2.4 Third MSc at Siemens Wind Power

Michael Armstrong [5] based his work on the modal surface wave analysis and he applied this method to the measured data in order to estimate the soil stiffness and damping profile.

Firstly, he presented a theoretical derivation of the wave propagation in a continuum focusing his attention on the modal surface wave equation (no forcing term, so then source independent) and he concluded that the roots of the determinant of the homogeneous system migrate in the complex plane. Subsequently, Michael made a comparison between the cylindrical and the Cartesian coordinate equations concluding that the 3D modelling has to be preferred because, dealing with Bessel function solutions, it can incorporate the geometric decay. Moreover, a new misfit function has been introduced. Indeed, the one proposed by Corine required to compute the roots of the theoretical model which is computationally very expensive. Michael used an objective function defined as the sum of the determinant at the modal positions picked from the measured data. A normalization based on the phase velocity is also applied to get a similar value for the determinant over the entire grid.

In the second part, some sensitivity tests were performed. Damping turned out to cause a shift of the location of the modal roots towards smaller wavenumbers, but it was noticed that the shift is relatively small for the expected amount of damping ratio of 0 – 10%. After having proven that the location of the modal roots has low sensitivity to damping, it was chosen to split the inversion for dynamic soil properties into 2 steps: a damping-independent method to find the stiffness profile, and then estimate the damping profile in a second step. Nevertheless, a correct stiffness

profile is a requisite for estimating the damping profile. They are not independent steps but can be taken subsequently. Later, testing the model for the sensitivity of the other parameters, it was found that, as expected, the model is highly sensitive to shear wave velocity and quite sensitive to thickness of the layers. Density and pressure wave velocity have a small influence on the model response spectrum too. Moreover, it has been found that layer splitting could become an interesting tool for experienced users to improve the inversion method, while a fine layer discretization is required to predict the modal dispersion curves; in particular, a resolution of 4 times smaller than the smallest wavelength is recommended. Then, the modal surface wave inversion was applied to the measured data from IJsselmeer in the Netherlands and to the Gjøa dataset available from a collaboration with NGI. The inversion has been performed by using the genetic algorithm created by Corine with some key modifications such as re-ranging, layer stripping and phased settings. Good results and practicability are found using the algorithm for synthetic data. For the IJsselmeer case, four different layered soil models are tested. In the end, it turned out that the modal inversion is significantly more successful than the full waveform process used in the first two theses. Satisfying results were found for a 21 layered soil model and a root set with semi-automated picking which only contained the 3 lower modes. For the high-quality dataset collected in Gjøa, only one layered soil models was analysed with two roots sets; the first used only the fundamental mode while the latter attributed progressive weight to the different modes. Excellent results are obtained for both the cases; in particular, in the latter model, a high level of certainty has been reached down to 15m. The plotted theoretical dispersion curves show that the fundamental mode matches well with the measured one while the higher modes present some deviations.

In the last part of the thesis, Michael focused his attention on the identification of the material damping. The objective function for the damping inversion has been based on the suitability between the modal damping curves of the measured data and the theoretical model. For the former, Michael reported four non-invasive technique used to determine the material damping from measured data; from the comparison between them, the Half-power Bandwidth method turned out to be the most suitable method for the problem in terms of accuracy and computational effort. Regarding the theoretical model, he chose the Phase Damping Ratio and he proved that it is equivalent to the curve derived from the method applied to measured data. Subsequently, in order to speed damping inversion up, the method of the Wavelet Compression is applied to reduced the number of points where the suitability function is computed. Then, the damping inversion is performed on synthetic cases. This has shown that the damping inversion is highly sensitive to the shallow layers and less to the half-space properties. Finally, it was not possible to apply the damping

inversion to the measured data because from a preliminary analysis the root finder tool turned out to be not robust and the complex roots could have not been reliably determined.

1.3 Research goal

As Michael shown, stiffness and damping inversions can be decoupled. Therefore, damping is not needed to estimate the shear velocity profile starting from surface wave analysis measurement. Nevertheless, soil damping represents a key parameter in the soil-structure interaction. The aim is to estimate the material soil damping profile starting from measured data. Different techniques are presented in literature for computing the attenuation curve and then estimating the soil damping profile through the inversion. These methods are shown and compared in this report in order to choose the most suitable one for the present attenuation analysis.

Moreover, analyses and studies must be performed in order to relate the analysis of surface waves to offshore wind turbine applications. Indeed, the source excitation in MASW is not fully comparable to the oscillation of the turbine in terms of frequency content and type of generated waves. To summarize, the research goal of this project can be expressed by the following two questions:

- *“Can modal surface wave analysis estimate the soil damping profile from measured data?”*
- *“How can results from MASW be related and applied to study Soil Structure Interaction (SSI) of Offshore Wind Turbines (OWT)?”*

Since the previous inversion model failed, to give answer to the first question, a reliable complex root finding tool has to be implemented first and tested with synthetic test cases. Then, the damping inversion can be performed on measured data after a parameter analysis and pre-processing on the dataset. Finally, the uncertainty or error associated to the damping profile must be characterized.

The second question aims to fill the gap between the MASW results and the offshore wind turbines applicability. In fact, the frequency range of the surface wave analysis is 5-50 Hz while the natural frequency of an offshore turbine is much below 1 Hz (about 0.1 or 0.2 Hz). In order to make such a relation, it is necessary to understand the dispersive behaviour of the parameters (frequency dependency) and how these parameters affect the SSI for OWT. Unfortunately, not much literature is presented for soil damping at low frequencies. This makes this project more challenging and topical.

1.4 Thesis outline

Chapter 2 gives an introduction to the wave propagation theory. Two wave models are presented along with the damping modelling. The wave modal analysis is reported and the governing system for a layered soil model is derived.

Chapter 3 presents the details of the modal inversion method developed in this work. First, the general concept of the inversion analysis is illustrated and the domain of interest is analysed. Then, the functions and the characteristics of the inversion tool are presented together with the specifics of the optimization algorithm used.

Chapter 4 presents the model studies and the sensitivity analyses to different parameters of the model. From these studies, the direct implications for the damping inversion are drawn.

In Chapter 5, the model layering is reduced and the stiffness profiles that are used in the estimation of the material damping are estimated. For the first time in this project, the Love wave stiffness inversion is proposed.

In Chapter 6, the modal damping inversion method is applied to in-situ measured data. The results of the two damping inversions are compared and discussed.

Chapter 7 focuses on the analysis of the relation material damping versus frequency by using measured data. Three methods are proposed for retrieving this relation and the advantages and the limitations are discussed.

In Chapter 8, the conclusions of the present thesis are drawn along with some recommendations in order to improve the method and the results in further researches.

Chapter 2

Theory and Derivations

This chapter illustrates the theory and the derivations which the project is based on. First, an overview of the four different types of waves propagating in a continuum is presented and the elastic wave equation is derived. Then, the wave modal analysis is introduced and discuss. Finally, the governing system for a layered soil model is shown. This chapter is mostly inspired by [21], [15], [35], [17], [38].

2.1 Seismic waves

In an elastic, isotropic and homogeneous soil system, two types of waves may propagate. One category is composed by the body waves which travel through the medium and they are identified as: P-waves and S-waves.

- P-waves: longitudinal waves which provoke compression and rarefaction of the material while passing through the medium. The motion of the particles is parallel to the direction of propagation of the waves. P-waves can travel through solid and acoustic media since both of them have compression strength.
- S-waves: transverse waves which cause shear deformation in the material. The motion of the particles is orthogonal with respect to the direction of propagation of the wave. Since acoustic media cannot experience shear stresses, S-waves can travel only in solid and fluid materials. They can be classified with respect to the direction of motion of the particles. SH-waves are horizontally polarized waves while, SV-waves are vertically polarized waves.

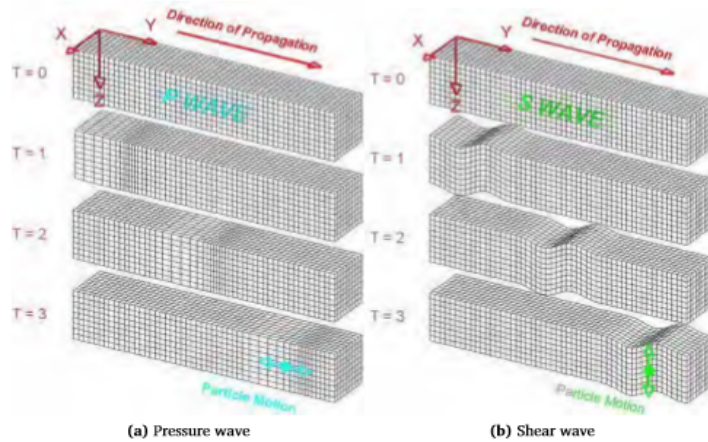


Figure 2.1: Particle motion in body waves.

Figure 2.1 shows the different behaviour of the two body waves. While, Figure 2.2 shows the decomposition of the S-waves. The wave velocity depends on the mechanical characteristic of the medium where they travel. Since soil is stiffer to compression, compressional waves are faster than the shear waves; indeed the former are called primary waves and the latter secondary waves. The dependency between the wave velocity and the characteristics of the soil can be expressed by using the mass-density ρ and the elastic Lamé' parameters μ and λ , as shown in Equation 2.1 and Equation 2.2.

$$C_p = \sqrt{\frac{\lambda + 2\mu}{\rho}} \quad (2.1)$$

$$C_s = \sqrt{\frac{\mu}{\rho}} \quad (2.2)$$

The other category of waves is composed by the interface waves which occur at the free surface (in this case, they are called surface waves) or at the interfaces between soil and another medium (fluid, air or even, in certain conditions, soil). When body waves appear at a boundary between two media, they can interfere and partly convert to each other giving rise to surface or interface waves. The most important interface phenomena are the so-called free interface waves that propagate along the surface between two media with subsequent delivery of energy from



Figure 2.2: Generic orthogonally polarized waves.

sources outside the interface [35]. Since surface waves are given by the composition of P-waves and S-waves (SV or SH), the interface waves can only exist if one of the two media is a solid (indeed presenting shear stiffness). By the composition of P-waves and SV-waves, three types of interface waves can be generated depending on the nature of the two media: Rayleigh waves (soil-vacuum), Scholte waves (soil-liquid), Stonely waves (soil-soil, they may propagate only under certain combination of parameters). In addition to that, by the appearance of SH-waves at the free surface, Love waves can be generated. Figure 2.3 shows a representation of the classification of the basic interface waves by [35]. In Figure 2.4, Rayleigh and Love waves are presented visually. Unlike Rayleigh waves, which have coupled P-SV type displacement, Love waves contain only SH motion. Love waves require a velocity structure that varies with depth, and cannot exist in a uniform half-space [36].

In this thesis, as will be deeply explained in 6, a high quality dataset which is obtained by using a prototype seabed-coupled shear wave vibrator is used for the damping inversion. In this measurement, the receivers are settled on the seabed, therefore, Scholte and Love waves are expected. In soil, Scholte waves generate an elliptic motion of the particle due to the shear stresses that cannot be taken by water and have a penetration depth of about one and a half wavelength of the propagating Scholte wave. The penetration in the fluid is small when the soil is very soft while, for water-rock combinations the penetration in the fluid is much higher



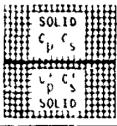
CLASS OF INTERFACE	TYPE OF FREE INTERFACE WAVE
VACUUM 	<u>RAYLEIGH WAVE</u> $c_R = n' c_S$ $0.875 \cdot n' \cdot 0.956$
LIQUID 	<u>SCHOLTE WAVE</u> $c_{Scl, \min} \left\{ \begin{matrix} c_p \\ c_s \end{matrix} \right.$
	<u>STONELEY WAVE</u> $\text{ind } x \left\{ \begin{matrix} c_R \\ c'_R \end{matrix} \right\} \quad c_{St} \quad \text{ind } y \left\{ \begin{matrix} c_S \\ c'_S \end{matrix} \right\}$

Figure 2.3: Classification of the basic interface-waves [35].

[14]. In water, the vertical and the horizontal displacement amplitudes decrease exponentially with the same magnitude generating a forward circular motion. In soil, the horizontal component presents a sign changing at the depth of about one-tenth of the Scholte wavelength, generating an elliptic retrograde motion in the upper layers and a forward elliptic motion in the lower layers. Both horizontal and vertical displacement present an asymptotic behaviour. Figure 2.5 shows the particle motion in the water column while, Figure 2.6 shows the particle motion in the soil column. On the other hand, Love waves move the ground from side to side horizontally meaning that they generate only a horizontal perpendicular motion of the particles. The amplitude, along with the strength, decreases exponentially with depth.

2.2 Elastic wave equation

In this section, the wave equation is derived for an elastic, homogeneous and isotropic continuum. The equation of motion for a 3 dimension wave is derived by using the ECK principle [17]. First, the kinetic equation is presented. Then, the constitutive equation is discussed. Thirdly, the equilibrium equations are derived. Finally, the 3D elastic equation of motion is obtained as a combination of the three mentioned

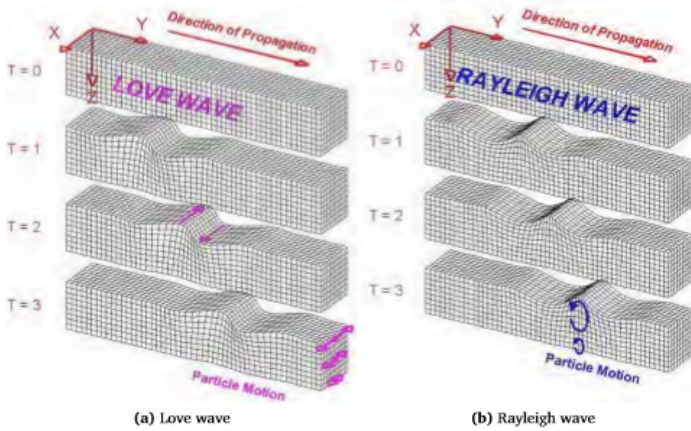


Figure 2.4: Particle motion in surface waves.

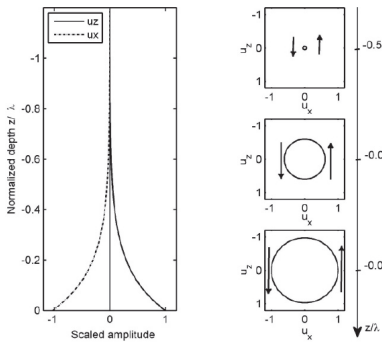


Figure 2.5: Particles displacements and orbits in water [14].

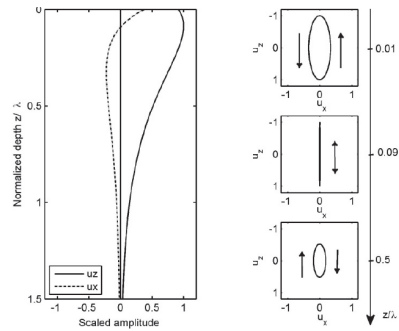


Figure 2.6: Particles displacements and orbits in soil [14].

relations. In this derivation, Einstein notation is applied where the comma denotes the partial differentiation with respect to a spatial coordinate.

2.2.1 Kinematic equation

The kinematic equation is the relation between the displacements and the strains. Considering the generic displacement u_i , it can be differentiated with respect to

the three directions x,y,z. By using Einstein notation, the kinetic relation can be summarized as following for $i, j = 1, 2, 3$:

$$\epsilon_{ij} = \frac{1}{2}(u_{i,j} + u_{j,i}) \quad (2.3)$$

Two types of independent deformations are possible. An isotropic compression, where the volume changes but the angles remain the same. A shear deformation, where the volume does not change but the angles do change. The shear deformation is noted with letter γ and it is defined for $i \neq j$ as:

$$\gamma_{ij} = \frac{\delta u_j}{\delta x_i} + \frac{\delta u_i}{\delta x_j} = 2\epsilon_{ij} \quad (2.4)$$

In three dimension, the small strain components give rise to the second order tensor ϵ_{ij} which is symmetric and therefore only six of the nine components are independent.

2.2.2 Constitutive equation

The constitutive equation is the relation between the strain and the stress and it depends on the mechanical characteristic of the considered material. When soil behaviour is expected to stay in the small strain regime (strain below 10^{-5} [18]), as for the level of deformation induced by seismic waves, it is possible to assume an elastic model and the shear modulus is a key parameter to properly model soil behaviour. The constitutive equation for an isotropic, homogeneous, linear elastic solid can be expressed by the generalized Hook's law. For the isotropic components of the tensors, the relation can be expressed in the vector notation as following:

$$\begin{pmatrix} \epsilon_{xx} \\ \epsilon_{yy} \\ \epsilon_{zz} \end{pmatrix} = \frac{1}{E} \begin{pmatrix} 1 & -\nu & -\nu \\ -\nu & 1 & -\nu \\ -\nu & -\nu & 1 \end{pmatrix} \begin{pmatrix} \sigma_{xx} \\ \sigma_{yy} \\ \sigma_{zz} \end{pmatrix} \quad (2.5)$$

where E is the Young's modulus and ν is the Poisson ratio which gives the relation between the deformations in different directions; most of the soil types present values between 0.1 and 0.5. The Equation 2.5 is called flexibility relation and it can be inverted in order to obtain the stiffness relation:

$$\begin{pmatrix} \sigma_{xx} \\ \sigma_{yy} \\ \sigma_{zz} \end{pmatrix} = \frac{E}{(1 + \nu)(1 - 2\nu)} \begin{pmatrix} 1 - \nu & \nu & \nu \\ \nu & 1 - \nu & \nu \\ \nu & \nu & 1 - 2\nu \end{pmatrix} \begin{pmatrix} \epsilon_{xx} \\ \epsilon_{yy} \\ \epsilon_{zz} \end{pmatrix} \quad (2.6)$$

By introducing the Lamé parameters which are defined as following:

$$\lambda = \frac{\nu E}{(1 - 2\nu)(1 + \nu)} \quad (2.7)$$

$$\mu = \frac{E}{2(1 + \nu)} \quad (2.8)$$

The stiffness relation can be expressed in this form:

$$\begin{pmatrix} \sigma_{xx} \\ \sigma_{yy} \\ \sigma_{zz} \end{pmatrix} = \begin{pmatrix} \lambda + 2\mu & \lambda & \lambda \\ \lambda & \lambda + 2\mu & \lambda \\ \lambda & \lambda & \lambda + 2\mu \end{pmatrix} \begin{pmatrix} \epsilon_{xx} \\ \epsilon_{yy} \\ \epsilon_{zz} \end{pmatrix} \quad (2.9)$$

It can be seen that μ is the shear modulus also defined as G . Moreover, the stiffness relation can be written by using the definition of the bulk modulus $K = \lambda + 2G/3$. In an isotropic linear-elastic medium, pure shear stress τ is related to pure shear strain γ by the following equation for $i \neq j$:

$$\tau_{ij} = G\gamma_{ij} = \mu\gamma_{ij} = 2\mu\epsilon_{ij} \quad (2.10)$$

By using the vector notation, the shear components of the stiffness relation can be expressed in the following form:

$$\begin{pmatrix} \sigma_{xy} \\ \sigma_{xz} \\ \sigma_{yz} \end{pmatrix} = \begin{pmatrix} 2\mu & 0 & 0 \\ 0 & 2\mu & 0 \\ 0 & 0 & 2\mu \end{pmatrix} \begin{pmatrix} \epsilon_{xy} \\ \epsilon_{xz} \\ \epsilon_{yz} \end{pmatrix}, \quad (2.11)$$

Using the Einstein notation, the full three dimension stress-strain relation can be summarized as:

$$\sigma_{ij} = \lambda\epsilon_{kk}\delta_{ij} + 2\mu\epsilon_{ij} \quad (2.12)$$

where δ_{ij} the Kronecker Delta defined as:

$$\delta_{ij} = \begin{cases} 1, & \text{if } i = j \\ 0, & \text{if } i \neq j \end{cases} \quad (2.13)$$

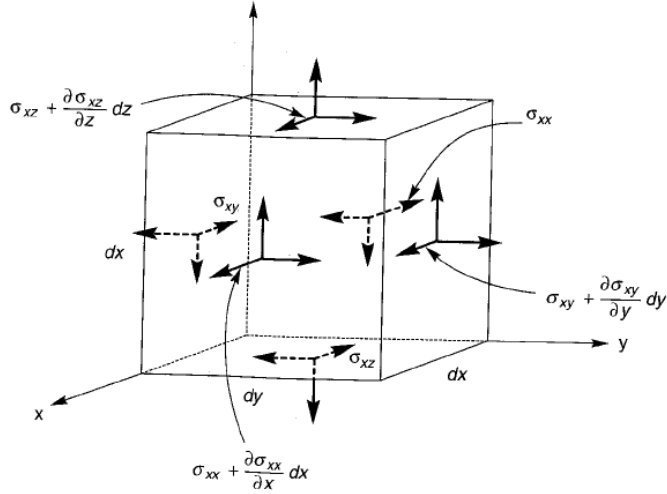


Figure 2.7: Stresses in x-direction on infinitesimal cube [21].

2.2.3 Equilibrium equation

The equilibrium equation is the relation between the internal stresses and the force applied to solid. By following the sign notation shown in Figure 2.7, the equilibrium of forces in x-direction is given by:

$$\Delta x_2 \Delta x_3 \left(\frac{\partial \sigma_{11}}{\partial x_1} \Delta x_1 \right) + \Delta x_1 \Delta x_3 \left(\frac{\partial \sigma_{21}}{\partial x_2} \Delta x_2 \right) + \Delta x_1 \Delta x_2 \left(\frac{\partial \sigma_{31}}{\partial x_3} \Delta x_3 \right) = \Delta x_1 \Delta x_2 \Delta x_3 \rho \frac{\partial^2 u_1}{\partial t^2} \quad (2.14)$$

Performing the equilibrium on all the directions and rearranging the equations lead to the following system of equations:

$$\begin{aligned} \frac{\partial \sigma_{11}}{\partial x_1} + \frac{\partial \sigma_{21}}{\partial x_2} + \frac{\partial \sigma_{31}}{\partial x_3} &= \rho \frac{\partial^2 u_1}{\partial t^2} \\ \frac{\partial \sigma_{11}}{\partial x_1} + \frac{\partial \sigma_{21}}{\partial x_2} + \frac{\partial \sigma_{31}}{\partial x_3} &= \rho \frac{\partial^2 u_1}{\partial t^2} \\ \frac{\partial \sigma_{11}}{\partial x_1} + \frac{\partial \sigma_{21}}{\partial x_2} + \frac{\partial \sigma_{31}}{\partial x_3} &= \rho \frac{\partial^2 u_1}{\partial t^2} \end{aligned} \quad (2.15)$$

With the index notation, the above system can be rewritten in the form:

$$\rho \ddot{u}_i = \sigma_{ji,j} \quad (2.16)$$

2.2.4 Equation of motion

The equation of motion (EOM) is derived by combining the kinematic equation (Equation 2.3), the constitutive equation (Equation 2.12) and the equilibrium equation (Equation 2.16). Substituting the first relation in the second one, the following equation is obtained:

$$\sigma_{ij} = \lambda u_{k,k} \delta_{ij} + \mu (u_{i,j} + u_{j,i}) \quad (2.17)$$

Then, Equation 2.17 can be substituted in the equilibrium equation, obtaining:

$$\rho \ddot{u}_i = \lambda u_{j,ji} + \mu (u_{i,jj} + u_{j,ij}) \quad (2.18)$$

This is the equation of motion in the three directions x , y and z . It represents a system of partial differential equations and it is second order with respect to time and second order with respect to the three spatial coordinates, therefore it requires 2 initial conditions and 2 boundary conditions for each spatial coordinate. Equation 2.18 can be written in the vector form and a generic external force can be included.

$$\rho \ddot{\bar{u}}_i = (\lambda + \mu) \nabla (\nabla \cdot \bar{u}) + \mu \nabla^2 \bar{u} + \bar{f}_{ext} \quad (2.19)$$

where the nabla operator $\nabla = [\delta_1, \delta_2, \delta_3]$ and the Laplace operator $\nabla^2 = \frac{\partial^2}{\partial x_1^2} + \frac{\partial^2}{\partial x_2^2} + \frac{\partial^2}{\partial x_3^2}$. Equation 2.19 is valid for soil. Since water cannot experience shear deformations, it is needed to introduce the acoustic equation to describe the motion of the particles in water which can be obtained from the elastic equation by setting the shear stiffness μ equal to zero.

$$\rho \ddot{\bar{u}}_i = \lambda \nabla \nabla \cdot \bar{u} + \bar{f} \quad (2.20)$$

2.3 Modal surface wave equations

In the present work, a modal approach is applied to the theoretical model. Therefore, in this formulation, the external excitation is not taken into account and the right

hand side is set equal to zero. The goal of the modal analysis is to find the dynamic properties of the system identifying the frequencies for which the system naturally resonates. This analysis highlights the intrinsic properties of the system which are independent from the exciting force.

By using MASW, both the two types of surface waves can be generated depending on the source involved in the measurements. If an air gun (in water) or a hummer (on the soil) is used to generate the seismic waves, longitudinal surface waves start to propagate on the surface by following a cylindrical symmetry with the axis centred in the point of action of the source. This means that in each direction it is possible to observe only Rayleigh or, equivalently, Scholte waves. On the other side, if a shear wave vibrator is involved in the measurements (this can only happen in the soil since water cannot take shear deformations), directivity is observed and the types of waves registered depend on the relative disposition of the source direction and the array of the receivers. If the two directions coincide, again Rayleigh or Scholte waves are registered. If the oscillation of the source is perpendicular to the direction of the array, Love waves are found. For the other cases, intermediate situations are observed where combinations of the different types of waves occur. For both longitudinal surface waves and shear surface waves, the tangent wavefront is perpendicular to the direction of the receivers, but the oscillation of the particles is different. With this premises, two models are implemented in this work to describe both the Rayleigh/Scholte wave and the Love wave propagation. The solutions will be presented for the two cases starting from the general 3D wave equation (Equation 2.19) setting the right hand side equal to zero.

2.3.1 Rayleigh waves

As said, Rayleigh waves are surface waves in which the particles experience an elliptic motion in the vertical plane parallel to the direction of propagation of the wavefront. They can be described by using a spherical or a cylindrical model since the source is point wise and the generated wavefronts are concentric circles. In the far field condition, the curvature of the circular wavefronts is so small that can be approximated to his tangent and the situation can be reduced to a planar wave problem. In this two-dimensional formulation, the wave propagates only in one direction, which will be called x_1 , and the oscillation of the particles belongs to the plane $x_1 - x_3$. Therefore, there is not motion on x_2 direction and the planar situation allows to neglect every differentiation depending on the out of plane direction: $\delta_2 = 0$. The displacement model is written as $u = u(x_1, x_3)$. In the next chapters of this thesis, Scholte waves will be treated most of time but, since the formulation is identical, Rayleigh waves are considered in this theoretical part for simplicity of the

model and in applying the boundary conditions.

The starting point of the derivation is the homogeneous equation of motion of a continuum written in the vector form (Equation 2.19):

$$\rho \ddot{\bar{u}}_i = (\lambda + \mu) \nabla (\nabla \cdot \bar{u}) + \mu \nabla^2 \bar{u} \quad (2.21)$$

where, \bar{u} is a 2x1 vector since $u = u(x_1, x_3)$. In order to decouple the two equations, as suggested by [38], the so-called Helmholtz decomposition of a vector is applied:

$$\bar{u} = \nabla \phi + \nabla \times \bar{\psi} = \bar{u}_p + \bar{u}_s \quad (2.22)$$

where ϕ is the scalar potential and the $\bar{\psi}$ is the vector potential. The first contains the compressional part and the second one the rotational part of the particle motion which is the the plane $x_1 - x_3$ and therefore only one axis of rotation is present. This is the one defined by the perpendicular direction to the motion plane, namely \bar{e}_2 . The following properties are valid for the potentials:

$$\begin{aligned} \phi &\sim \nabla \cdot \bar{u} \\ \bar{\psi} &\sim \nabla \times \bar{u} \end{aligned} \quad (2.23)$$

By substituting Equation 2.22 into Equation 2.21, it is found:

$$\rho \partial_t^2 (\nabla \phi + \nabla \times \bar{\psi}) = (\lambda + \mu) \nabla (\nabla \cdot (\nabla \phi + \nabla \times \bar{\psi})) + \mu \nabla^2 (\nabla \phi + \nabla \times \bar{\psi}) \quad (2.24)$$

Here, some relations have to be applied to simplify the previous equation:

$$\begin{aligned} \nabla \cdot (\nabla \times \bar{\psi}) &= 0 \\ \nabla \cdot \nabla &= \nabla^2 \\ \nabla^2 (\nabla \phi) &= \nabla (\nabla^2 \phi) \\ \nabla^2 (\nabla \times \bar{\psi}) &= \nabla \times (\nabla^2 \bar{\psi}) \end{aligned} \quad (2.25)$$

By applying Equations 2.25, Equation 2.24 can be rewritten in the following form:

$$\nabla (\rho \partial_t^2 \phi - (\lambda + 2\mu) \nabla^2 \phi) + \nabla \times (\rho \partial_t^2 \bar{\psi} - \mu \nabla^2 \bar{\psi}) = 0 \quad (2.26)$$

This equation is satisfied if the terms under the Nabla operator are both zeros. It is possible then to highlight two uncoupled equations that govern the system:

$$\begin{aligned} \rho \partial_t^2 \phi - (\lambda + 2\mu) \nabla^2 \phi &= 0 \\ \rho \partial_t^2 \bar{\psi} - \mu \nabla^2 \bar{\psi} &= 0 \end{aligned} \quad (2.27)$$

By introducing the definition of the body waves velocities C_p (compressional waves, Equation 2.1) and C_s (shear waves, Equation 2.2), the two equations appear in the form:

$$\begin{aligned}\frac{1}{C_p^2} \partial_t^2 \phi &= \nabla^2 \phi, & C_p &= \sqrt{\frac{\lambda + 2\mu}{\rho}} \\ \frac{1}{C_s^2} \partial_t^2 \bar{\psi} &= \nabla^2 \bar{\psi}, & C_s &= \sqrt{\frac{\mu}{\rho}}\end{aligned}\quad (2.28)$$

As mentioned before, a planar problem is considering with $u_2 = 0$ and $\partial_2 \bar{u} = 0$. From this assumption, it comes out that the vector $\bar{\psi}$ is such that $\bar{\psi} = \psi_2 \bar{e}_2 = \psi \bar{e}_2$ and therefore the second equation of 2.28 reduces to a scalar equation as following:

$$\begin{aligned}\frac{1}{C_p^2} \partial_t^2 \phi &= \nabla^2 \phi \\ \frac{1}{C_s^2} \partial_t^2 \psi &= \nabla^2 \psi\end{aligned}\quad (2.29)$$

Frequency-wavenumber domain

The solutions of the two PDEs are found in the frequency domain in which the equations turn to ODEs. In this case, the frequency domain is considered both in time and space since a wave propagation problem is handled. The first refers to the traditional time frequency which can be identified as an angular frequency $\omega = \frac{2\pi}{T}$ where T is the period or as the ordinary frequency $f = \frac{1}{T}$. The second refers to the spatial frequency of the wave, called wavenumber, which is related to the wavelength λ following to different definitions: the wavenumber which account for the number of wavelengths per unit distance is defined as $\nu = \frac{1}{\lambda}$, while the angular wavenumber is $k = \frac{2\pi}{\lambda}$. In this work, for the time frequency the symbol ω is adopted while for the wavenumber the symbol k is used. To avoid confusions related to quantities, units will be mentioned in the graphs.

In order to take the governing equations (Equation 2.29), the forward Fourier transform is applied:

$$\tilde{f}(\kappa_1, x_3, \omega) = \int_{-\infty}^{\infty} \int_{-\infty}^{\infty} f(x_1, x_3, t) e^{i(\kappa_1 x_1 - \omega t)} dx_1 dt \quad (2.30)$$

For completeness, the corresponding Fourier inverse transform definition is reported:

$$f(x_1, x_3, t) = \frac{1}{4\pi^2} \int_{-\infty}^{\infty} \int_{-\infty}^{\infty} \tilde{f}(k_1, x_3, \omega) e^{-i(k_1 x_1 - \omega t)} dx_1 dt \quad (2.31)$$

The Equations 2.29 appear in the Fourier domain in the following form:

$$\begin{aligned} -\frac{\omega^2}{C_p^2} \tilde{\phi} &= -k_1^2 \tilde{\phi} + \frac{d^2 \tilde{\phi}}{dx_3^2} \\ -\frac{\omega^2}{C_s^2} \tilde{\psi} &= -k_1^2 \tilde{\psi} + \frac{d^2 \tilde{\psi}}{dx_3^2} \end{aligned} \quad (2.32)$$

In these equations, it is possible to recognize the wavenumbers related to both the compressional wave velocity C_p and the shear wave velocity C_s :

$$\begin{aligned} k_p &= \frac{\omega}{C_p} \\ k_s &= \frac{\omega}{C_s} \end{aligned} \quad (2.33)$$

Finally, the ODEs can be written in the following form:

$$\begin{aligned} \frac{d^2 \tilde{\phi}}{dx_3^2} + (k_p^2 - k_1^2) \tilde{\phi} &= 0 \\ \frac{d^2 \tilde{\psi}}{dx_3^2} + (k_s^2 - k_1^2) \tilde{\psi} &= 0 \end{aligned} \quad (2.34)$$

The solutions to Equations 2.34 can be easily obtained:

$$\begin{aligned} \tilde{\phi}(k_1, x_3, \omega) &= A e^{-q_p x_3} + B e^{q_p x_3}, \quad q_p = \sqrt{k_1^2 - k_p^2} > 0 \\ \tilde{\psi}(k_1, x_3, \omega) &= C e^{-q_s x_3} + D e^{q_s x_3}, \quad q_s = \sqrt{k_1^2 - k_s^2} > 0 \end{aligned} \quad (2.35)$$

The conditions related to the square root of q_p and q_s are needed to assure that both are real-valued and therefore there are not propagating waves in x_3 direction. Indeed, considering the compressional part of the solution, it is possible to make some considerations about the values which k_1 can assume and their meaning; similar considerations can be applied to the rotational part. To simplify the analysis, an

homogeneous halfspace is assumed; so then, the second term of the solution is set to zero ($B = 0$) since it does not satisfy the Sommerfeld radiation condition: "No energy may be radiated from infinity into ... the field", (A. Sommerfeld, 1949). First, it is worth to recall the general solution as the combination of the Equations 2.31 and 2.35:

$$\tilde{\phi} e^{-i(k_1 x_1 - \omega t)} = A e^{-i(k_1 x_1 - q_p x_3 - \omega t)}, \quad q_p = \sqrt{k_1^2 - k_p^2} \quad (2.36)$$

If $k_1 = 0$, there is only propagation in x_3 direction and $q_p = k_p$ meaning that only vertical pressure waves propagate. When $0 < k_1 < k_p$, waves propagate in the plane $k_1 - k_3$ in both the direction resulting $k = \sqrt{k_1^2 + k_3^2} = \omega/C_p$. While, if $k_1 = k_p$, the propagation is only in x_1 direction since $q_p = 0$. The last condition is $k_1 > k_p$, which is the one met in Equation 2.35. In this case, the waves propagate in x_1 direction and are evanescent in x_3 direction along which they show an amplitude exponential decay. In the figure below, a schematic of the present analysis is reported.

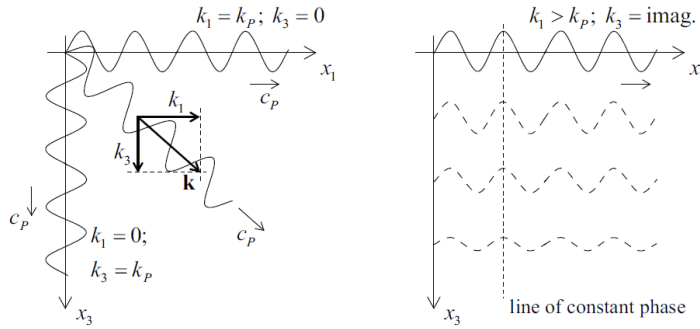


Figure 2.8: Harmonic waves in 2D. Left panel: propagating waves in x_3 direction. Right panel: evanescent waves in x_3 direction [38].

Once the solutions of the EOMs are derived, the boundary conditions can be applied in order to find the unknowns appearing in Equations 2.35. Considering a halfspace, two conditions are needed. For Rayleigh waves, the free surface is stress free meaning that both the compressional and shear stress are equal to zero:

$$\sigma_{33}(x_1, x_3 = 0, t) = \sigma_{31}(x_1, x_3 = 0, t) = 0 \quad (2.37)$$

By recalling the Helmholtz decomposition (Equation 2.22) and the general solution (Equation 2.36), it is possible to write the two displacements u_x and u_z in the

following form:

$$\begin{aligned} u_1(x_1, x_3, t) &= \partial_1 \tilde{\phi} - \partial_3 \tilde{\psi} = -ik_1 \tilde{\phi} - \partial_3 \tilde{\psi} \\ u_3(x_1, x_3, t) &= \partial_3 \tilde{\phi} + \partial_1 \tilde{\psi} = \partial_3 \tilde{\phi} - ik_1 \tilde{\psi} \end{aligned} \quad (2.38)$$

The stresses can be found by applying Equation 2.17:

$$\begin{aligned} \sigma_{33}(x_1, x_3, t) &= \lambda(\partial_1^2 \tilde{\phi} + \partial_3^2 \tilde{\phi}) + 2\mu(\partial_3^2 \tilde{\phi} + \partial_{13}^2 \tilde{\psi}) \\ &= \lambda(-k_1^2 \tilde{\phi} + \partial_3^2 \tilde{\phi}) + 2\mu(\partial_3^2 \tilde{\phi} - ik_1 \partial_3 \tilde{\psi}) \\ \sigma_{31}(x_1, x_3, t) &= \mu(2\partial_{13}^2 \tilde{\phi} + \partial_1^2 \tilde{\psi} - \partial_3^2 \tilde{\psi}) \\ &= \mu(-2ik_1 \partial_3 \tilde{\phi} + \partial_1^2 \tilde{\psi} - \partial_3^2 \tilde{\psi}) \end{aligned} \quad (2.39)$$

Equation 2.37 represents a system of equations which can be written in the matrix form by introducing Equation 2.39 as:

$$\begin{pmatrix} 2k_1^2 - k_s^2 & 2ik_1 q_s \\ -2ik_1 q_p & 2k_1^2 - k_s^2 \end{pmatrix} \begin{pmatrix} A \\ C \end{pmatrix} = \begin{pmatrix} 0 \\ 0 \end{pmatrix} \quad (2.40)$$

In this formulation, the governing system is homogeneous because no forces has been applied since a modal analysis is considered. In general, in order to get non-trivial solutions for the unknowns A and C which guarantee the existence of the surface waves, the determinant of the coefficient matrix must be zero. This leads to the secular Rayleigh equation:

$$4k_1^4 - 4k_1^2 k_s^2 - 4k_1^2 q_p q_s + k_s^4 = 0 \quad (2.41)$$

The solution to this equation is known as modal solution and represents the combinations of ω and k_1 for which the system resonate. By substituting $k_1 = \omega/c_1$, which is the same definition previously given to k_p and k_s , it is possible to find the solution $C_1 = C_r$ where C_r is the Rayleigh velocity and it respects the condition $C_r < C_p, C_s$. It is worthy to highlight that for a halfspace C_r is frequency independent, also referred to as non-dispersive behaviour.

The next steps have been derived by following [38] and [36]. Since the right hand side is a zero vector, the solution for A and C of the eigenvalue problem cannot

be found but it is possible to find the ratio between the eigenvectors related to the eigenvalues by choosing one of the two equations:

$$\frac{C}{A} = \frac{2k_1^2 - k_s^2}{2ik_1q_s} \quad (2.42)$$

Substituting this relation into Equation 2.38 and considering the displacements at the free surface $x_3 = 0$, it is possible to find the ratio between the horizontal and the vertical displacement of the particles, as shown by [38]:

$$\frac{u_1(x_3 = 0)}{u_3(x_3 = 0)} = -2i \frac{\sqrt{1 - \frac{C_r^2}{C_s^2}}}{2 - \frac{C_r^2}{C_s^2}} = |E|e^{-i\frac{\pi}{2}} \quad (2.43)$$

From the above relation, it can be deduced that the horizontal motion has a phase lag of $\pi/2$ and the motion is retrograde since the ratio is negative. Obviously, this solution gives only information about the ratio between the displacements. In order to find the amplitudes, a force must be added and the non homogeneous system has to be solved to find the values of A and C .

2.3.2 Love waves

In order to describe the response of a soil system on which a shear vibrator is acting, a full 3D wave model is desirable since a directivity behaviour is introduced by the source and no symmetry can be retrieved. A.V. Vostroukhov [40] has proposed a 3D method of analysis of the steady-state response of a layered halfspace due to a horizontal load. This model is defined in cylindrical coordinates and the solution is found in the frequency domain by using the Hankel transform. All the three displacements are considered (radial, tangential and vertical) and, for each interface, six conditions are imposed concerning continuity of displacements and stresses (compressional and shear in two directions). Therefore, the modal solutions include both the Rayleigh and the Love waves. Figure 2.9 shows the modal solutions for a three layers overlying a halfspace soil system. As can be observed, a (green) straight line is presented in the graph. It is necessary to highlight that this does not represent resonance combination of f - k for the body waves - since body wave velocities are frequency independent, no dispersion should expect in the f - k domain - instead they are fake roots without any physical meaning. In fact, as explained before, the solutions are found by setting the determinant of the coefficient matrix of the general solution to zero. Since the determinant is not unique, not all the zeros of the determinant equation have to be considered as belonging to the dispersion curve. The

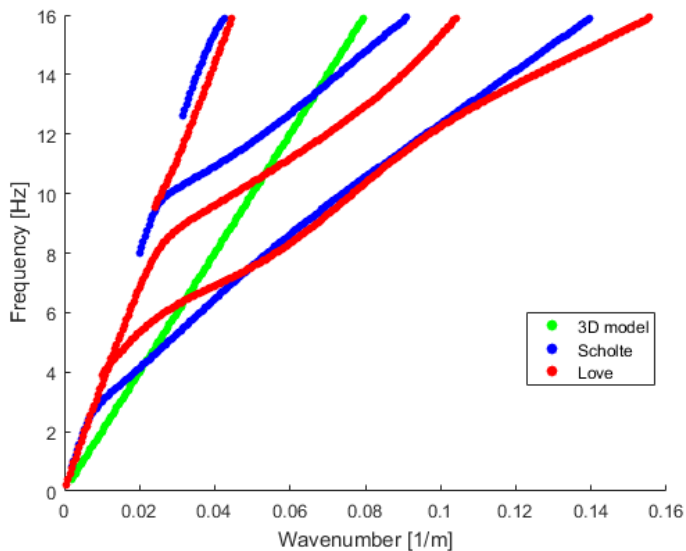


Figure 2.9: Modal solutions of the full 3D model. Identification of the different contributors.

“true” zeros are the ones which remain zero under at least one possible excitation of the system.

This model is able to capture the complexity of the problem at hand and it can be reduced to a form of a single integral that can be taken numerically. Nevertheless, for the present application, this formulation is not feasible because it is computationally very expensive - as it will be shown later this represents an important issue - and the modal solutions of the Rayleigh and the Love waves in the f - k domain tend to be very close or even to overlap resulting difficult to distinguish them in order to be useful for the damping inversion. Moreover, in a MASW test which aims to register Love waves, the streamer is dislocated in a unique direction that is perpendicular to the oscillation of the source and this is sufficient for reducing the situation to a 2D plane problem in Cartesian coordinates. Indeed, any cylindrical wave can be represented as an infinite superposition of plane waves, meaning that the plane wave analysis is representative for the present case.

As it has been done for the Rayleigh waves, the formulation of the 2D plane Love wave problem starts from the homogeneous equation of motion of a continuum

written in the vector form (Equation 2.19):

$$\rho \ddot{\bar{u}}_i = (\lambda + \mu) \nabla (\nabla \cdot \bar{u}) + \mu \nabla^2 \bar{u} \quad (2.44)$$

Love waves contain only SH motion of the particles, so then the only displacement considered is $u_2 = u_2(x_1, x_3, t)$. Moreover, the planarity conditions allows to neglect any derivative in the x_2 direction. The previous equation simplifies as:

$$\rho \ddot{u}_2 = \mu \nabla^2 u_2 \quad (2.45)$$

By following the analogous steps taken for the derivation of the Rayleigh waves, it is possible to proof that the general solution for a wave propagating in x_1 direction is given by the form:

$$u_2(x_1, x_3, t) = [Ae^{-q_s x_3} + Be^{q_s x_3}] e^{i(k_1 x_1 - \omega t)} \quad (2.46)$$

where, $q_s = \sqrt{k_1^2 - k_s^2}$. In order to satisfy the Sommerfeld radiation condition, the displacements for a halfspace is obtained from Equation 2.46 by setting $B = 0$. From this consideration, it is immediately clear that Love waves cannot exist in just a homogeneous halfspace. They need a soil structure where the shear wave velocity varies with depth (namely, at least a layer over the halfspace). In fact, in a uniform halfspace, the stress free condition at the free surface is not compatible with the model since it brings to find that also A is equal to zero. Therefore, the derivation is developed considering a single layer over a uniform halfspace system. The two solutions are detected as:

$$\begin{aligned} \text{Layer}(1) : u_2(x_1, x_3, t) &= [Ae^{-q_{s1} x_3} + Be^{q_{s1} x_3}] e^{i(k_1 x_1 - \omega t)} \\ \text{Halfspace}(2) : u_2(x_1, x_3, t) &= Ce^{-q_{s2} x_3} e^{i(k_1 x_1 - \omega t)} \end{aligned} \quad (2.47)$$

The boundary condition at $x_3 = 0$ is the free stress condition:

$$\sigma_{x_3 x_2, L}(x_1, x_3 = 0, t) = \frac{\partial u_2(x_1, x_3, t)}{\partial x_3} = 0 \quad (2.48)$$

This equation leads to find that $A = B$. The interfaces conditions are the continuity of the displacements and the shear stresses at $x_3 = H$:

$$\begin{aligned} u_{2,1}(x_1, x_3 = H, t) &= u_{2,2}(x_1, x_3 = H, t) \\ \mu_1 \sigma_{x_3 x_2, 1}(x_1, x_3 = H, t) &= \mu_2 \sigma_{x_3 x_2, 2}(x_1, x_3 = H, t) \end{aligned} \quad (2.49)$$

By rearranging the Equations 2.49, the following 2x2 system of equations is obtained:

$$\begin{pmatrix} 2\cosh(q_{s1}H) & -e^{-q_{s2}H} \\ 2\mu_1 q_{s1} \sinh(q_{s1}H) & \mu_2 q_{s2} e^{-q_{s2}H} \end{pmatrix} \begin{pmatrix} A \\ C \end{pmatrix} = \begin{pmatrix} 0 \\ 0 \end{pmatrix} \quad (2.50)$$

The modal solutions are the zeros of the determinant equation of the coefficient matrix. The determinant equation is given by the following:

$$2\cosh(q_{s1}H)\mu_2q_{s2}\exp(-q_{s2}H) + 2\exp(-q_{s2}H)\mu_1q_{s1}\sinh(q_{s1}H) = 0 \quad (2.51)$$

Which can be rewritten by using the property of the Hyperbolic tangent ($\tanh(x) = -i \tan(ix)$), as:

$$\tan(iq_{s1}H) = \frac{\mu_2q_{s2}}{i\mu_1q_{s1}} \quad (2.52)$$

The parameter q_s can expressed as a function of the shear and Love wave velocities:

$$q_s = \sqrt{k_1^2 - k_s^2} = \sqrt{\frac{\omega^2}{c_L^2} + \frac{\omega^2}{c_s^2}} = k\sqrt{1 - \frac{c_L^2}{c_s^2}} \quad (2.53)$$

To ensure that all the terms in Equation 2.52 are real, the condition $c_{s1} < c_L < c_{s2}$ has to be respected. By introducing Equation 2.53 into Equation 2.52, the following is obtained:

$$\tan(\omega H \sqrt{c_{s1}^{-2} - c_L^{-2}}) = \frac{\mu_2 \sqrt{c_L^{-2} - c_{s2}^{-2}}}{\mu_1 \sqrt{c_{s1}^{-2} - c_L^{-2}}} \quad (2.54)$$

By defining $t = \sqrt{c_{s1}^{-2} - c_L^{-2}}$, it is possible to find the solution to Equation 2.54 in a graphic way. This equation represents the condition of existence of the Love waves. For each frequency, intersections between the two curves are found and those represent the modal solutions corresponding to different branches of the dispersion curves. From this graphical solution, it is possible to retrieve the well known phase velocity-frequency graph, which is a useful tool for the dispersion analysis. This concept will be extensively explained in Chapter 3. Figure 2.10 shows the solutions for $\omega = 1.256\text{rad/s}$, $H = 3\text{m}$, $C_{s1} = 150\text{m/s}$, $C_{s2} = 500\text{m/s}$ and $\mu_2/\mu_1 = 1.2$.

2.3.3 Model comparison

The full 3D model proposed by [40] has been implemented in Matlab by the author in order to compare the modal solutions corresponding to the Love waves with the ones obtained by using the 2D plane model. As expected, the roots of the two models line up perfectly showing a correct formulation of the 2D model. As an example, Figure 2.11 shows the modal solutions for a system composed of a layer over a halfspace. Figures 3.5a and 3.5b presents the Rayleigh and the Love roots

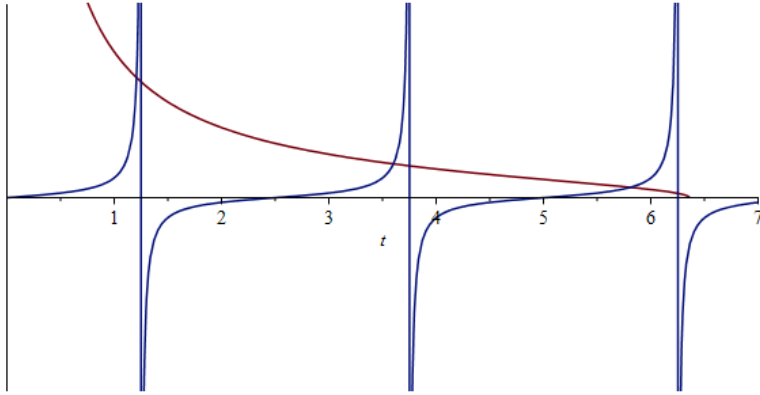


Figure 2.10: Graphical solution of the Equation 2.54.

obtained respectively with the Rayleigh model developed in Section 2.3.1 and the Love model implemented in this section. Figure 2.11c shows the solutions of the full 3D model and Figure 2.11d checks that the roots of the two 2D models coincide with the one of the 3D model.

2.4 Damping modelling

While propagating into a medium, a wave is subjected to attenuation. Two types of attenuations contribute to the amplitude decay [7]: geometric damping and material damping. The first is due to the spreading of energy over the wavefront which increases travelling away from the source while the second refers to the energy dissipation within the material due to the material properties. In soil, the latter can be attributed to many factors including inter-particle sliding and friction, structure rearrangement, and pore fluid viscosity (in a porous media model) [6].

The formulations proposed in the previous sections refer to linear elastic soil media, namely no effect of the material damping has been considered. In this section, the focus lies on giving an overview of some models presented in literature which are able to include this attenuation in the problem formulation. This section is mainly inspired by Chapter 2.7 by S.A. Badsar [7].

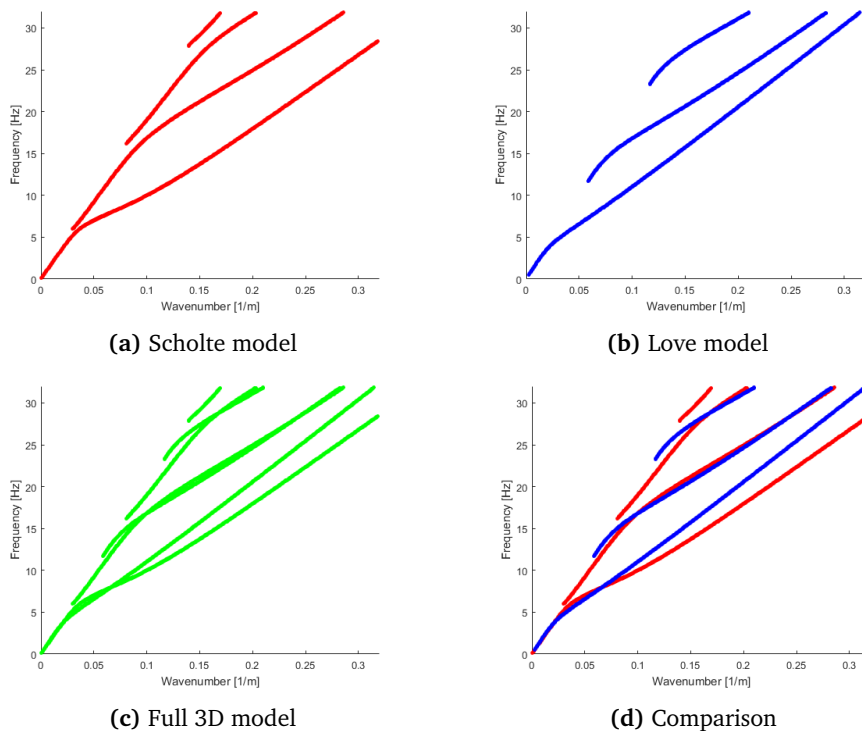


Figure 2.11: Modal solutions for a one layer overlying a halfspace soil system.

2.4.1 The visco-elastic model

For medium shear strain ratio ($10^{-5} < \gamma < 10^{-3}$), the linear visco-elastic model is commonly used for describing the material behaviour. In this range of strain, the level of deformation is still small enough to consider that both the shear modulus and the material damping ratio remain constant in cyclic loading; this behaviour is also called non-degraded hysteresis type [18]. The general formulation of this model starts from considering a sinusoidal shear stress applied to a soil mass.

$$\tau = \tau_0 e^{i\omega t} \quad (2.55)$$

where τ_0 is the shear stress amplitude. The resulting complex strain is given by:

$$\gamma = \gamma_0 e^{i(\omega t - \phi)} \quad (2.56)$$

where γ_0 is the shear strain amplitude and ϕ denotes the delay due to the presence of damping. Clearly, this is zero if damping is not considered. Now, it is possible to compute the complex shear modulus following its definition:

$$\mu^* = \frac{\tau}{\gamma} = \frac{\tau_0}{\gamma_0} e^{i\phi} = \frac{\tau_0}{\gamma_0} (\cos \phi + i \sin \phi) \quad (2.57)$$

By defining the following quantities:

$$\begin{aligned} \mu &= \frac{\tau_0}{\gamma_0} \cos \phi && \text{Elastic modulus} \\ \mu' &= \frac{\tau_0}{\gamma_0} \sin \phi && \text{Viscosity} \end{aligned} \quad (2.58)$$

The complex shear modulus can be rewritten as:

$$\mu^* = \mu + i\mu' \quad (2.59)$$

with amplitude $|\mu^*| = \sqrt{\mu^2 + \mu'^2}$ and phase $\phi = \tan^{-1}(\mu'/\mu)$. The ratio μ'/μ is also known as the loss factor η , which is a measure of the material damping D that is related to η by a factor 2 ($\eta = 2D$).

Several methods are presented in literature for defining the complex shear modulus. In this section, two models are proposed to include damping in the problem formulation. One is frequency dependent and one is frequency independent. The derivations about the hysteretic behaviour of the visco-elastic material model concerning the quantities related to the hysteretic stress-strain curve are treated in Appendix A.

Kelvin-Voigt model

The Kelvin-Voigt model is the simplest way to describe the visco-elastic material model. It is the composition two elementary models: a Hookean linear spring (stiffness) which is connected in parallel with a Newtonian viscous dashpot (damping). The damping force is proportional to the velocity while the amount of energy dissipated is related to the frequency and the amplitude. Due to the connection in parallel, both the elementary models experience the same strain level and the total shear stress is given by the sum of the two contributes:

$$\tau = G\gamma + G' \dot{\gamma} \quad (2.60)$$

By introducing Equations 2.55 and 2.56 in equation above, it is possible to find the following:

$$\tau_0 e^{i\phi} = \gamma_0 (G + i\omega G') \quad (2.61)$$

Considering Equation 2.61 and remembering that $\eta = \mu' / \mu$, it can be deduced that the complex shear modulus can be written as:

$$\mu^* = \mu(1 + i\omega\eta) \quad (2.62)$$

In analogy, the same holds also for the elastic modulus λ which can be written as:

$$\lambda^* = \lambda(1 + i\omega\eta) \quad (2.63)$$

In this formulation, the viscosity μ' is directly proportional to the frequency. This means that the damping increases linearly with the frequency loading. From the literature review, it has been found that for low frequencies the material damping has no frequency dependency [4]. Therefore, the viscous model seems not to be representative for the soil behaviour.

Hysteretic Kelvin-Voigt model

Ishiara [18] states that: “The energy dissipation in soils is mostly rate-independent and of hysteretic nature, and the damping ratio can be used to represent the energy absorbing properties of soils.” Therefore, in this section, the Hysteretic Kelvin-Voigt model, in which the viscosity is frequency independent, is presented. The modification can be applied directly to the viscosity coefficient dividing it by the frequency:

$$\mu' = \frac{\eta_s \mu}{\omega} \quad (2.64)$$

In order to incorporate this material model in the present formulation, it is necessary to express the complex moduli as a function of the elastic moduli and the damping coefficient:

$$\begin{aligned} \lambda_* &= \lambda_0(1 + 2iD_p) \\ \mu^* &= \mu_0(1 + 2iD_s) \end{aligned} \quad (2.65)$$

where $D_p = \eta_p/2$ and $D_s = \eta_s/2$ are respectively the frequency independent hysteretic compressional and shear material damping ratio. The derivation of the relation between D and η is reported in Appendix A.

The equations 2.65 are introduced in the theoretical model when the coefficient matrix is computed for each frequency and wavenumber in the f-k domain and they represent a direct way to add the damping in the model by using the material damping ratio.

As will be explained in Chapter 3, when damping is introduced the system the solutions of the complex determinant equation are complex. This means that the

modal wavenumber solution will be composed by a real and an imaginary part. The first represents the wavenumber of the propagating wave in x_1 direction while the latter gives rise to an exponential decay along direction x_1 and which is representative of the attenuation due to the material damping.

$$\tilde{\phi} e^{-i(k_1 x_1 - \omega t)} = e^{-i(k_{1,RE} x_1 - \omega t)} e^{-q_p x_3} e^{-k_{1,IM} x_1} \quad (2.66)$$

2.5 Cylindrical coordinates

As explained in Chapter 1, the main focus of this work is on getting a reliable estimation of the material soil damping profile from measured dataset. In order to do that, a better understanding on how damping behaves in the formulation is needed. As said, damping is composed by two combined contributors: geometric and material damping. The goal is to properly model the geometric damping in order to only highlight and treat the material damping. A different approach in the formulation is therefore needed.

In a undamped 2D homogeneous halfspace situation with line source, the harmonic components of the Fourier transform do not decrease in space and continue to infinity. Indeed, in this case, no geometric radiation appears since there is not spreading to the lower halfspace or laterally. This leads to the conclusion that the waves are not subject to any amplitude decay. This simplified model is therefore not able to include the geometric spreading.

Considering instead the situation proposed in Section 2.3.1, the point source conditions allows to use cylindrical coordinates in the formulation resulting in a Cylindrical ODE problem. Bessel functions arise as solutions of potential problems in cylindrical coordinates. These functions are able to naturally incorporate the geometric spreading since they are in the form of a combination between a sinusoidal function and an exponential decay. The Bessel functions appears in the Hankel transformation which is the operation used by this approach to take the governing equation to the frequency domain; the derivation is then analogous to the one reported for the Scholte wave solution. This approach is not applicable to the actual formulation of the Love wave model since only a 2D plane analysis as been presented. In the Table 2.1, a comparison between the solution for displacement and stresses in both Cartesian and Cylindrical coordinates is presented.

As can be seen from the table, the magnitude of the solutions is the same for both the formulation. Notwithstanding, it is possible to observe that the integration kernel of the inverse transform is different and this gives rise to a different solution in terms of spatial decay in the space-time domain. Moreover, the effect of the

Table 2.1: Displacement and stress equations in 2D and 3D [5].

	Cartesian	Cylindrical
u_1	$(-ik_1)\tilde{\phi} - \partial_3\tilde{\psi}$	$-(k_r)\tilde{\phi} - \partial_3\tilde{\psi}$
u_3	$\partial_3\tilde{\phi} + (-ik_1)\tilde{\psi}$	$\partial_3\tilde{\phi} + (k_r)\tilde{\psi}$
σ_{31}	$\mu(2(-ik_1)\partial_3\tilde{\phi} + (-k_1^2)\tilde{\psi} - \partial_3^2\tilde{\psi})$	$\mu(-2(k_r)\partial_3\tilde{\phi} + (-k_r^2)\tilde{\psi} - \partial_3^2\tilde{\psi})$
σ_{33}	$(\lambda + 2\mu)\partial_3^2\tilde{\phi} + \lambda(-k_1^2)\tilde{\phi} + 2\mu(-ik_1)\partial_3\tilde{\psi}$	$(\lambda + 2\mu)\partial_3^2\tilde{\phi} + \lambda(-k_r^2)\tilde{\phi} + 2\mu(k_r)\partial_3\tilde{\psi}$

choice of the transform method is reflected in the width of the peaks in the energy spectrum response. A deeper understanding on how the transformations work will be presented in Section 6.1 where the collected measured data are pre-processed before being used in the inversion algorithm.

Nevertheless, in this work, a full waveform response is not computed for the theoretical model since the forward analysis is only about the modal solutions. Therefore, there is not difference if the coefficient matrix and so the determinant are computed by using the cartesian or the cylindrical coordinates because the coefficients are not affected by the different transformation used.

2.6 Layered model

In the previous sections, the surface wave propagation problem has been presented for a homogeneous halfspace (Scholte waves, Section 2.3.1) and for a single layer over a halfspace (Love waves, Section 2.3.2). Now, the formulation has to be extended to a vertically inhomogeneous halfspace modelled as a horizontally layered soil system. Each layer is characterized by the governing equations (potentials or displacement) and the interface conditions which relate displacements and stresses to the ones of the contiguous elements. The top layer expects boundary conditions and the halfspace has to respect the non-radiation condition. The dimension of the global coefficient matrix depends on the number of layers and the surface wave model used.

In the implementation, the coefficients are firstly computed with the symbolic software Maple and then loaded into the Matlab function. In fact, Matlab was not giving satisfying computational time results while using its built-in symbolic tool. To speed up the computation again, the coefficient matrix is built by using the Matlab function *sparse matrix* which avoids the software to store the zero elements of the matrix. This is useful since the matrix results to have the non-zero values located

close to the principal diagonal and many zero elements due to the fact that non-contiguous layers do not have any coupling.

2.6.1 Scholte waves

In the Scholte waves model, explained in Section 2.3.1, the governing equations for each layers are written in terms of potentials. The expressions of the potentials for the j -th layer, in local coordinates with x_1 along the horizontal direction and x_3 pointing downwards, are the presented in Equation 2.67. In order to help the numerical computation the positive exponential along x_3 is limited to be equal to 1 at the bottom layer boundary as shown in the following:

$$\begin{aligned}\tilde{\phi}_j(x_{3,j}) &= A_j e^{-q_{pj} x_{3,j}} + B_j e^{q_{pj}(x_{3,j} - thk_j)}, \quad q_{pj} = \sqrt{k_1^2 - k_{pj}^2} > 0 \\ \tilde{\psi}_j(x_{3,j}) &= C_j e^{-q_{sj} x_{3,j}} + D_j e^{q_{sj}(x_{3,j} - thk_j)}, \quad q_{sj} = \sqrt{k_1^2 - k_{sj}^2} > 0\end{aligned}\quad (2.67)$$

In the model, a layer of water above the top soil layer needs to be introduced to describe the situation present in the measured data. This determines also the fact that Scholte waves (interface waves between soil and fluids) are used in this formulation. As said before, water is an acoustic medium and therefore only the acoustic potential $\tilde{\phi}$ is considered since $\mu = 0$ and so $\psi = 0$.

$$\tilde{\phi}_j(x_{3,j}) = A_j e^{-q_{pj} x_{3,j}} + B_j e^{q_{pj}(x_{3,j} - thk_j)}, \quad q_{pj} = \sqrt{k_1^2 - k_{pj}^2} > 0 \quad (2.68)$$

The displacements for an acoustic layer are the following:

$$\begin{aligned}u_{1|j}(k_1, x_{3,j}, \omega) &= -ik_1 \tilde{\phi}_j \\ u_{3|j}(k_1, x_{3,j}, \omega) &= \partial_3 \tilde{\phi}_j\end{aligned}\quad (2.69)$$

The compressional and shear stresses are expressed as:

$$\begin{aligned}\sigma_{33|j}(k_1, x_{3,j}, \omega) &= -k_1^2 \lambda \tilde{\phi}_j + 2\mu \partial_3^2 \tilde{\phi}_j \\ \sigma_{31|j}(k_1, x_{3,j}, \omega) &= -2ik_1 \mu \partial_3 \tilde{\phi}_j\end{aligned}\quad (2.70)$$

While, for the soil layers, the displacements and stress expressions have been presented in Section 2.3.1.

Boundary and Interface Conditions

The global system is assembled by considering the conditions about displacements and stresses that hold between the different layers of the model. The conditions which give rise to the governing system and therefore the coefficient matrix are listed below:

- Water-air interface
 - Pressure at the free surface equals zero.
- Water-soil interface
 - No shear stress can be transferred at the soil-liquid interface - soil shear stress equal to zero.
 - Continuity of vertical stresses.
 - Continuity of vertical displacements.
- Regular soil-soil interface
 - Continuity of horizontal and vertical displacements.
 - Continuity of horizontal and vertical stresses.
- Halfspace
 - No inward radiation at the infinite boundaries.

This set of equation forms a system having the number of the equation corresponding to the number of unknowns being equal to $2 + 4N_{soil} + 2$, where the first term is due to the acoustic layer, N_{soil} is the number of regular soil layers and the last term corresponds to the unknowns of the halfspace.

2.6.2 Love waves

In the Love wave model, as presented in Section 2.3.2, the governing equations are written in the form of displacements. Following the same coordinate system used for the previous case, the displacement model for the j-th layer is the following:

$$u_{2,j}(x_{3,j}) = [Ae^{-q_{sj}x_{3,j}} + Be^{q_{sj}(x_{3,j}-thk_j)}] \quad (2.71)$$

The shear stresses for the Love wave model are:

$$\sigma_{x_3x_2,j}(x_{3,j}) = q_{sj}[-Ae^{-q_{sj}x_{3,j}} + Be^{q_{sj}(x_{3,j}-thk_j)}] \quad (2.72)$$

In this case, considering that water is not able to experience shear stresses, the water layer over of the top soil layer does not play any role. Indeed, no conditions can be imposed at the water-soil interface in order to find the unknowns of the acoustic layer. Therefore, water will not be included in the Love wave model.

Boundary and Interface Conditions

The boundary and the interface conditions which give rise to the governing system and therefore the coefficient matrix of the Love wave model are listed below:

- Water-soil interface
 - No shear stress can be transferred at the soil-liquid interface - soil shear stress equal to zero.
- Regular soil-soil interface
 - Continuity of horizontal displacements.
 - Continuity of horizontal stresses.
- Halfspace
 - No inward radiation at the infinite boundaries.

In this modelling, the set of equation is smaller since less conditions have to be enforced to solve the problem (in the regular interfaces, half of the conditions are needed). The number of equations is equal to $2N_{soil} + 1$, where N_{soil} is the number of regular soil layers and the last term corresponds to the unknown of the halfspace. The dimension of the coefficient matrix of the Scholte model is generally more than twice as bigger as the one of the Love wave model.

Chapter 3

Modal Inversion Method

This chapter treats in details the several aspects of the Modal Inversion Method applied in this work. Firstly, the general concept at the basis of the inversion analysis is presented. Secondly, the properties of the frequency-wavenumber domain are analysed and the methods for computing the modal roots (both with and without damping) are explained. Then, the functions and characteristics of the inversion tool are presented together with the specifics of the algorithm used.

3.1 Inversion analysis

The inversion theory is well known and applied in the field of the Geophysics since it is a useful technique for retrieving the valuable information conveyed by the geophysical signals. The goal is to determining the geological structures from the measured data. The results of the process is highly influenced by the modelling of the system and in particular by its parametrization (the minimal set of parameters needed for characterizing the system).

In the formulation of a physical problem, two approaches can be followed: the forward and the inverse problems. In the forward model, the characteristics of the model which parametrize the physical reality are known and, given an input, it is possible to compute the response associated to the premises. In the inverse problem, some parameters of the model are unknown and they can be estimated by using an experimental dataset which works as a reference that has to be reproduced by the theoretical model. The unknown parameters are allowed to vary in order to match the theoretical model and the measured data. Indeed, the inversion problem

can be seen as an optimization (or minimization) problem in which the key aspect is represented by the objective function that will be presented in Section 3.5.2. In Figure 3.1, a schematic of a general inversion method is shown.

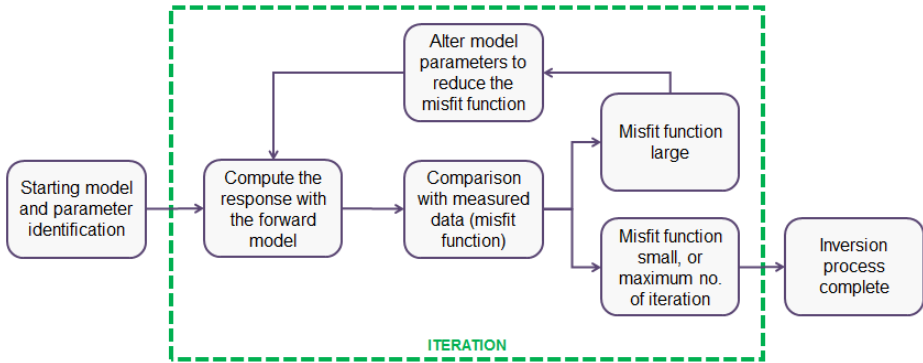


Figure 3.1: Flow chart of the inversion method analysis.

A drawback of a general inversion problem is that the solution is not unique. This means that different members of the searching domain can give the same solution. A good way to limit this eventual problem is to have a well educated guess in the choice of the ranges of the parameter domains.

3.2 Frequency-wavenumber domain

De Winter [13] confirmed the high sensitivity of the surface wave response spectrum to the shear-wave velocity profile of the stratified soil. In particular, this sensitivity could be well retrieved in the Frequency-wavenumber domain. In section 3.4, also the sensitivity to damping will be proved.

As previously explained in Chapter 2, the f - k domain is the results of a 2D Fourier transform over time and space and corresponds to the response energy spectrum. The dispersion curves (organised in different branches) are the results of the wave-field transformation process in the fk domain. Foti [15] reports: "The phenomenon of geometric dispersion is caused by the effects of constructive interference occurring in media that are either bounded or inhomogeneous. It is responsible for the existence of several modes of propagation each travelling at a different phase and

group modal velocity”. The dispersion is basically the way the surface waves spread out as they travel along the surface. It depends on the characteristic of the medium and its consequence lays in the fact that the phase velocity of the surface wave is not constant but it varies with frequency. The phase velocity gives the speed of a single sinusoidal travelling wave but this is not enough to describe the problem. Therefore, the group velocity is introduced to describe the velocity with which the modulation of the wave travels. In the fk domain, the group velocity is visualized as the slope of the dispersion curve. The mathematical definitions of the two velocities are expressed as following:

$$\begin{aligned} \text{Phase velocity : } c_{\text{phase}} &= \frac{f}{k} \\ \text{Group velocity : } c_{\text{group}} &= \frac{df}{dk} \end{aligned} \quad (3.1)$$

Another characteristic of the energy spectrum is that the feeling to the different layers depends on the wavelength ($\lambda = 1/k$) of the propagating wave. In particular, low wavenumbers feel deeper while high wavenumber are more influenced by the shallow layers. It is important to remember that the depth of feeling is generally assumed to be approximately equal to the wavelength of the propagating wave. An extended study on the mode shapes of the shear stresses versus depth has been performed by Armstrong [5], and it has shown that:

- Moving along a branch of the dispersion curves: the shape remains the same and the deeper layers sensitivity increases.
- Moving along constant frequency: the deeper layers sensitivity increases with increasing the wavenumber and the stress shapes become more oscillatory (switching between positive and negative values).
- Moving along constant wavelength: the deeper layer feeling slightly increases in the higher modes and the stress shapes become more oscillatory.

An interesting consideration that can be linked to this study concerns the low wavenumber range of the dispersive curve. Indeed, it can be observed that some consecutive straight lines appear in this region giving rise to a non-dispersive attitude of the curves. This is due to the fact that the wavelength is so large that the wave is feeling almost only the halfspace. In this situation, the system can be seen as a reduction of the original system where the shallow layers are merged together and negligible with respect to the halfspace dimension. Indeed, the surface waves travel in that region with the Scholte velocity of the halfspace. This velocity can be

computed by using the formulas given by [31], where the Scholte velocity is equal to $v_{Sch} = 1/Re(s)$ and the slowness s is such that it satisfies the following formula valid for a homogeneous halfspace:

$$(s^2 + \beta^2)^2 - 4\alpha\beta s^2 + \frac{\rho_f \alpha}{v_s \rho_s \gamma} = 0 \quad (3.2)$$

where $\alpha = \sqrt{s^2 - 1/v_p^2}$, $\beta = \sqrt{s^2 - 1/v_s^2}$, $\gamma = \sqrt{s^2 - 1/v_f^2}$, v_p is the pressure wave velocity, v_s is the shear wave velocity, v_f is the acoustic wave velocity, ρ_f is the fluid density and ρ_s is the soil density of the halfspace. Figure 3.2 gives a graphical proof of what has just been explained. The straight dashed line represents the Scholte wave velocity of the halfspace of TC3 profile (see Chapter 4 for the description of the synthetic soil profile).

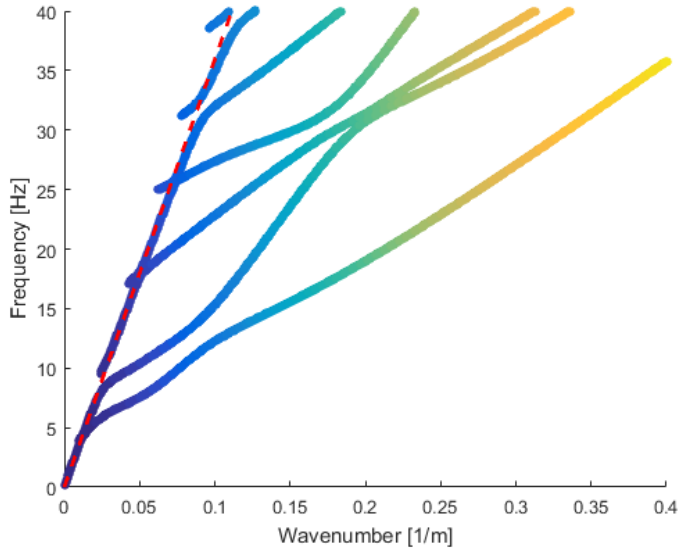


Figure 3.2: Scholte wave velocity of the halfspace - TC3 profile.

Moreover, by plotting the shear stresses (Figure 3.3), it is possible to observe that, even if the two points seem to belong to the same branch of the dispersion curve (see previous considerations), the mode shape is completely different highlighting the atypical behaviour of this region. In summary, the so-called non dispersive part

of the f-k domain is very sensitive to the characteristic of the halfspace, as will be visualize in Section 4.5.1.

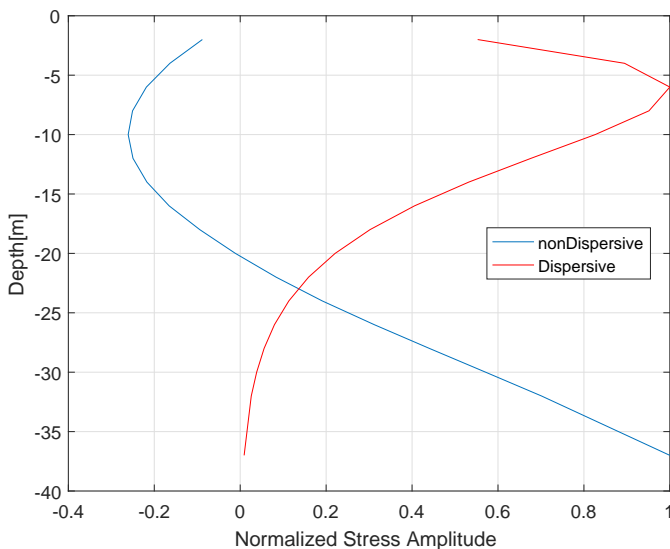


Figure 3.3: Mode shapes of two resonance f-k combinations belonging to the same branch of the dispersion curves: one in the non-dispersive region and one on the dispersive part - Linear C_s velocity profile

An analogous consideration can be made for the high wavenumbers (short wavelength). Considering the fundamental branch of the dispersion curves, it can be proved that the tangent to it at high wavenumbers is passing through the origin of the f-k domain and the slope corresponds to a halfspace with velocity equal to the Scholte wave velocity of the top soil layer (Figure 3.4). Considering the stress shape of the fundamental mode, this occurs because this branch for very short wavelengths it is almost only sensitive to the shallow layer and the others results to be negligible.

It is necessary to highlight that this behaviour starts to happen when the wavelength is such that it is at least equal to the thickness of the top soil layer. For completeness, it has been verified that this situation occurs also for Love waves even if they actually cannot exist in an homogeneous halfspace as proved in Section 2.3.2. This condition has to be met when, in a measured spectrum, the roots of the fundamental mode are picked in order to choose the proper fundamental one. This

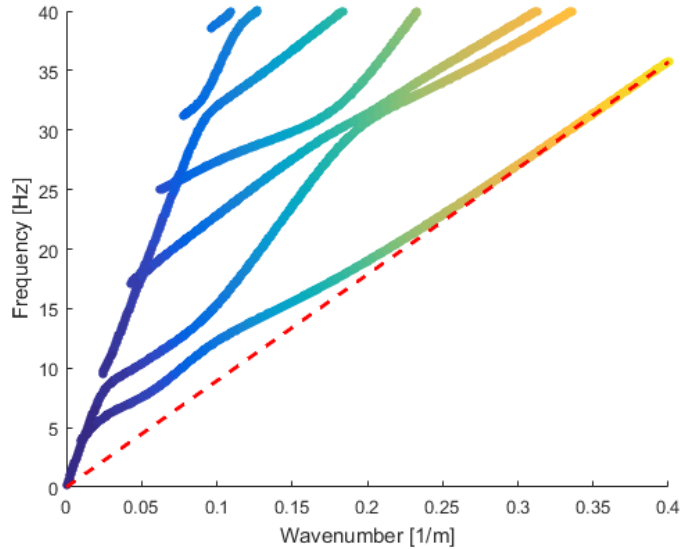


Figure 3.4: Scholte wave velocity of the top layer - TC3 profile.

concept will be extended in Section 5.1 for the used dataset.

Moreover, it can be observed in some models that the dispersion curves present many oscillations. This happens when the relative shear velocity profile presents sudden jumps indicating the presence of layers with different stiffness and different geotechnical characteristic (sand, clay or silt). In a smooth varying soil profile the branches are more regular and they tend to stay distant to each other. A comparison between two representative model is presented in Figure 3.5. This qualitative considerations have a clear importance since from them it is possible to get ideal guess of the possible result of the inversion and use it as a reference. Besides, a further investigation it is needed to understand the portions of the dispersion curves where the group velocity stays constant while the phase one varies; this occurs mostly in the non-smooth shear velocity profile.

Another interesting event that can appear in the f - k domain is the the so-called “mode kissing phenomenon”. It occurs between the modes at low frequencies when the dispersive energy of the lower mode visually meets the one of the higher mode, practically speaking the modal roots of are very close between the modes. It may cause mode misidentification, and as a result, lead to a larger overestimation of S -

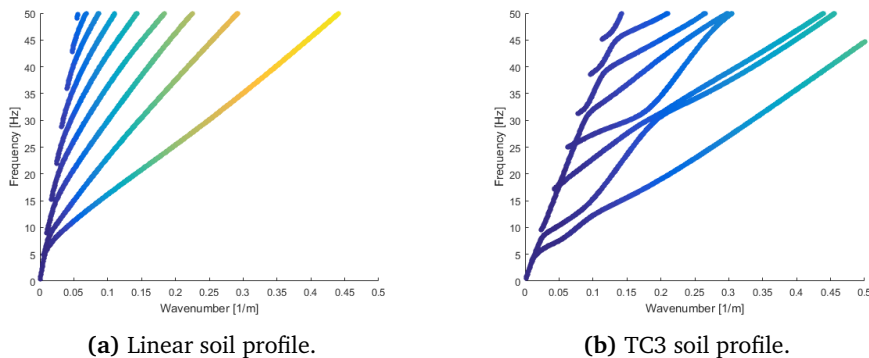


Figure 3.5: Visual comparison between C_s smooth and step varying soil profiles.

wave velocity and error on depth [16]. The reason for this behaviour can be found in the strong S-wave velocity contrasts between the different layers. Indeed, it is more likely to find this phenomenon in profiles with thick layers having a large difference in the shear wave velocity values rather than in profiles with a smooth varying of S-wave velocity. For a more extended explanation see paper by L.Gao et al. 2015 [16].

Some final considerations are made about the general characteristics of the f-k domain. In the present work, the focus is on the slow wave events (propagation of surface waves) and therefore the area of analysis is located in the right part of the graph. Moreover, it is possible to observe that the dispersion curves are limited on the left side by the maximum shear wave velocity of the soil system. Indeed, the propagation velocity of surface waves depends on the elastic constants near the surface and it is always less than the shear velocity. As an example, the ratio between the Rayleigh velocity and the shear velocity is given by $c_R/c_S = (0.862 + 1.14\nu)/(1 + \nu)$ (Freund, 1998), which is, for linear elastic material (poisson ratio $\nu > 0$), always less than 1. All the other events, such as pressure body waves or guided waves, which appear for velocities greater than the maximum shear wave velocity are not in the interest of this thesis.

3.3 Modal root finding

As presented in 2, the modal analysis is based on the identification of the natural modes and frequencies that a system assume during free vibration. In the present

case, the modal conditions are all the frequency-wavenumber combinations that lead the determinant equation to be equal to zero. It can be written implicitly as [15]:

$$\Phi[\lambda(x_3), \mu(x_3), \rho(x_3), k, \omega] = 0 \quad (3.3)$$

where λ , μ , ρ are respectively the first Lamé' parameter, the second Lamé' parameter and the the material density varying in depth. This equation is a highly nonlinear and a transcendental function of the arguments. It states that, in vertically inhomogeneous media, the velocity of propagation of surface Love and Scholte waves is a multivalued function of frequency. In the following two sections, the two methods used to computed the roots (both undamped and damped) are explained together with some considerations about other applicable techniques.

3.3.1 Undamped roots

By setting damping equal to zero, the roots of the complex secular equation are real and they will be called in this thesis undamped roots. The undamped roots correspond to the points where the response of the system is maximum, theoretically infinite since an undamped system can resonate. The location of the roots can be determined by searching for a sign switch on both the real and imaginary part of the determinant equation. In order to do that, the determinant is first computed on a grid defined in the fk domain and then, the search is performed along lines with constant wavenumber. In this way, a larger amount of roots can be found with a coarse mesh since the different mode are usually disposed quite horizontally because surface waves are slow events and the modes have a low slope in the f - k domain.

In this work, the core of the undamped root finder tool developed by [5] is used since it showed to give quite satisfying results. However, some improvements have been made in order to reach a better precision in the location. Indeed, it has been found that the Matlab function *fmincon* was not working as expected for this application and the roots having the same frequency were not merging to a unique one. In fact, more roots were founding for different wavenumbers since the mesh on the frequency axis was not fine enough to highlight the difference in the peaks considering the low slope of the curves. Therefore, a finer mesh for the frequency is introduced in order to the remove the "stair step" behaviour of the elastic roots as shown in Figure 3.6. By using this method, the total number of roots is increased since different roots are not any more merged into one. However, the computational time highly increases because using a fine mesh means that the determinant has to be computed for a larger amount of points but, since the elastic roots have to be

found only once at the beginning of the inversion problem, this does not largely affect the total computational time.

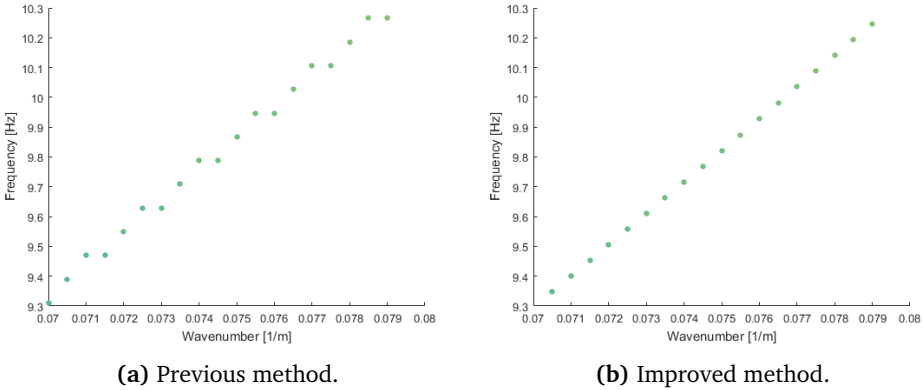


Figure 3.6: Zoom on the roots of the fundamental mode of TC3 soil profile.

3.3.2 Damped roots

Rix and Lai [24] state that: “As a result of using a general linear viscoelastic constitutive model, the wavenumbers and Rayleigh secular function become complex valued. In general, the problem of computing the zeros of a complex-valued function of a complex variable is not trivial, particularly if the function is highly nonlinear and known only numerically, as is the case for the Rayleigh secular function in vertically heterogeneous media. No general methods are available. They proposed a new technique which permits the determination of the complex roots based on the Cauchy residue theorem of complex analysis”. In this section, three methods will be discussed.

First, the author has implemented a tool in Matlab inspired on the theoretical basis of software package of Kravanja et al. (2000) [22] named Zeal (Zeros of Analytic functions) also based on Cauchy's Theorem. The solutions of the determinant equation are found by defining an associated polynomial which has the same roots of the original function. The basic idea of the program starts from the behavior of the roots when damping is applied. Indeed, as [5] shown, each complex root moves in the complex plane $k_{RE} - k_{IM}$ starting from the undamped one proportionally with the amount of damping and presents a slight shift towards the lower wavenumbers.

For weakly dissipative media, the location of the undamped roots can be used as a starting point for searching the damped ones. The search is developed for all the different undamped roots which are computed as explained in the previous section. A searching box is built in the complex plane $k_{RE} - k_{IM}$ starting from the location of the elastic root. Then, the winding number is computed to find the number of roots in the box. Computationally, it is profitable to work with boxes containing just one root, therefore, for winding numbers greater than one, a random grid is defined in the original box in order to find single root sub-boxes. Once found all the boxes, the root can be computed. This method requires the computation of the derivative in order to find the coefficients of the associated polynomial. Since the determinant equation is known only numerically, the derivative can only be computed numerically, which gives rise to many errors and inaccuracy.

Then, an alternative tool has been developed following the second part of the ZEAL algorithm. This method does not require the computation of the derivative and it is based on the theory of the formal orthogonal polynomials by defining a symmetric bilinear form which substitutes the derivative in the computation of the coefficients of the associated polynomial. This method has been tested with analytic mathematical functions giving very satisfying results. Unfortunately, it did not give reasonable results for the Rayleigh secular equation in the present work. Indeed, the winding number tool has shown inconsistencies and some roots were even visually wrong being out of the searching domain. These errors have been investigated by the author and some considerations are presented here. The method used as the basis for the algorithm is developed for solving analytic function while the determinant equation is only known numerically. This means that numerical integration methods are needed to compute the coefficients of the associated polynomial and a satisfying approximation is highly computationally demanding and cannot be reached with the available hardware in a reasonable amount of time. This precision is needed because the map from the Newton sums to the coefficients is ill-conditioned so then: "The polynomials that arise in practice may be such that small changes in the coefficients produce much larger changes in some of the zeros [22]."

Finally, another approach has been applied which can be seen as an iterative numerical method. It is based on the idea of building a box in the complex plane $k_{RE} - k_{IM}$ and compute the determinant on the grid points of the box. Once the minimum of the first iteration is found, a new finer grid is built around the first result and the new minimum is computed which will be the starting point for the next refinement. The procedure continues till the defined tolerance is reached. Any erroneous numerical zero are almost avoided by choosing the closest minimum along the k_{re} axis. The key part of the method is setting the appropriate values for the tolerance, the grid steps and the number of refinements in order to satisfy both

the precision needed and a reasonable computational time. For example, for the Gjøa profile, the number of steps is equal to 20 and the refinements are 5. It is already worth to highlight that the computational time is one of the main issues of the damping inversion as it will be explained in the Section 6. This method has given satisfying results with all the theoretical soil profiles tested in this work and therefore it will be used in the following applications for computing the damped roots. Figure 3.7 shows an example of the shape of the determinant function in the complex plane $k_{RE} - k_{IM}$ for TC3 for the elastic root (0.1759rad/m,38.38rad/s).

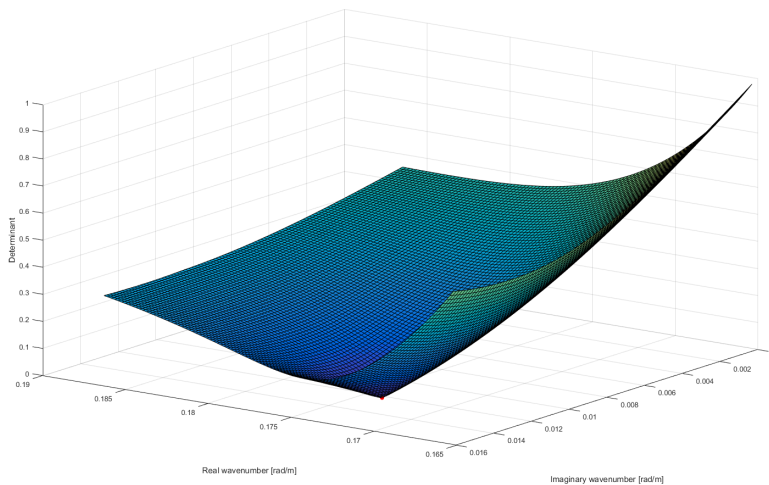


Figure 3.7: 3D plot of the determinant equation in the complex plane $k_{RE} - k_{IM}$ for TC3 soil profile - Elastic roots (0.1759rad/m,38.38rad/s) .

3.4 Attenuation analysis

Surface waves experience two types of spatial attenuation while propagating away from the source. One is associated with the geometry and it is called geometric spreading while the other one is associated to the intrinsic energy dissipation of the medium and it is named as material damping. These two contribute to the overall attenuation of the signal in the space domain. In the frequency-space domain, the

spectral amplitude for a single mode of an homogeneous half-space in the far field can be approximated by the following:

$$A_n(\omega, r) = A_{n,0}(\omega)\zeta(\omega, r)e^{\alpha_n(\omega)r} \quad (3.4)$$

where $\zeta(\omega, r)$ is the geometric damping and $\alpha(\omega)$ is the the attenuation coefficient. The attenuation coefficient is a wave propagation parameter. It describes the spatial amplitude decay of the surface wave as it propagates in an anelastic medium [30]. The attenuation analysis is generally performed on MASW measured data. The procedure requires accurate measurements of the amplitude of the surface wave particle motion and it is essential that the effect of noise is minimized or identified and removed afterwards [15].

Spatial decay

The geometric damping depends on the type of waves and the shape of the associated wavefront. The spatial decay corresponds to an amplitude attenuation of the waves which increases with the distance from the source; it is also called radiation damping. For an isotropic homogeneous halfspace, the spatial decay is proportional to $1/r^2$ for hemispherical body waves travelling on the free surface, $1/r$ for body waves in the interior fo the medium and $1/\sqrt{2}$ for cylindrical surface waves. The geometric attenuation coefficient becomes frequency dependent for a layered soil system and it is not possible to give a direct explicit expression a priori. In this work, the unknown geometric spreading is indicated as $\zeta(\omega, r)$.

Material damping

As previously said in Chapert 2, the soil material damping is an intrinsic characteristic of the material and it is related to various factors including inter-particle sliding and friction, structure rearrangement, and pore fluid viscosity. This parameter represents also the main focus of this research since the goal is to estimate the material damping profile of a layered halfspace i.e. find the characteristic value of the material damping for each layer.

It is interesting to highlight that Badsar [7] found out that with increasing frequency, the effect of the material damping in the amplitude decay becomes more significant with respect to the contribution of the geometric spreading. In the next sections, the methods for retrieving the attenuation coefficient from theoretical and measured data will be presented and discussed. They represent the theoretical basis of the damping inversion tool presented in Section 3.5.

3.4.1 Attenuation curve from the theoretical model

As shown in Chapter 2, the linear elastic wave problem can be converted in the viscoelastic domain by substituting the elastic moduli with the correspondent complex-valued moduli. In analogy with that, the homogeneous surface wave equation is extended to the viscoelastic media using the model complex wavenumber as presented by Misbah and Strobbia [30]:

$$k_n^* = k_n - i\alpha_n \quad (3.5)$$

where, n defines the number of the mode, k_n is the physical wavenumber, and α_n is the attenuation coefficient. Both the real and the imaginary part of the wavenumber k are frequency dependent and so Equation 3.5 can be rewritten as:

$$k_n^* = \frac{\omega}{v_n^*} = \left(\frac{\omega}{v_n} - i\alpha_n \right) \quad (3.6)$$

where, v_n is the physical phase velocity. The complex roots, also called damped roots, of the theoretical model can be computed using the complex root finding tool presented in Section 3.3.2 and therefore the modal attenuation curve of the theoretical model $\alpha_n(\omega)$ can be determined for the different modes.

Another parameter which is relevant for the attenuation analysis and often used in soil dynamics is the phase damping ratio $D(\omega)$ [30]. It is defined as the ratio between the energy dissipated and the average stored energy in one cycle of harmonic loading. The phase damping ratio is related to the quality factor Q defined by Borcherdt (1973) as following:

$$Q = \frac{1}{2D} \quad (3.7)$$

The relation between the Q factor and the complex wavenumber for homogeneous waves is delivered by Carcione [10]:

$$Q = \frac{Re[k^{*2}]}{Im[k^{*2}]} \quad (3.8)$$

Therefore the phase damping ratio $D(\omega)$ is defined as:

$$D(\omega) = \frac{Im[k^{*2}]}{2Re[k^{*2}]} \quad (3.9)$$

The phase damping ratio (also called Rayleigh phase damping ratio) is a modal property related to the material damping ratio of the subsurface layers. The variation

of modal damping as a function of the frequency is related to the geometric dispersion. These two presented parameters (attenuation coefficient and phase damping ratio) are equivalent [15].

3.4.2 Attenuation curve identification methods from measured data

Several methods are presented in literature for the identification of the material damping ratio, and consequentially the attenuation curve, from measured data obtained with MASW. In his work, Badsar [7] compares two existing methods and proposes a new technique. In this section, these three techniques are summarized and analysed.

Phase and amplitude regression in the frequency-space domain

The first method has been developed by Lai et al. (2002). The experimental dispersion curve $C_R^E(\omega)$ and attenuation curve $A_R^E(\omega)$ are determined subsequently in a phase and amplitude iterative regression scheme, by using the transfer function in the frequency-space domain. For a vertical harmonic load at the surface, the transfer function $h_{zz}(r, \omega)$ is the following form:

$$h_{zz}(r, \omega) = \zeta(r, \omega) \exp\left(-i \frac{\omega}{C_R^E(\omega)} r\right) \exp(-A_R^E(\omega)r) \quad (3.10)$$

The first term $\zeta(r, \omega)$ accounts for the geometric spreading. As presented in Section 3.4, this factor is set equal to $1/\sqrt{r}$ (as for an homogeneous half-space) in the first iteration since the stratification is unknown. The second factor represents a harmonic function depending on the phase velocity $C_R^E(\omega)$. The third factor is an exponential decay due to material damping, expressed with the attenuation coefficient $A_R^E(\omega)$. In the first step, an amplitude and a phase regression are performed separately in order to get the starting values of the two unknowns $C_R^E(\omega)$ and $A_R^E(\omega)$. In the second step, the regression is repeated but both the parameters are allowed to vary. Since, the result objective function has many local minima, well-chosen starting points are necessary to find the actual global minimum. Then, an inverse problem is solved to determine the experimental dispersion curve and this profile is used to update the geometric spreading. The method is iterated till convergence. Finally, an inversion problem is solved to determine the material damping profile. It is important to highlight that, this method can deal only with a single mode, no multiple modes are considered.

f – *k* analysis and amplitude regression

This method was developed by Rix et al.(2000). This method does not require any iteration since all the parameters are estimated in a direct way. Firstly, the dispersion curve $C_R^E(\omega)$ is estimated by analysis the data in the *f* – *k* domain. Secondly, an inversion problem is solved to determine the shear wave velocity profile which is used to estimate the spreading factor $\zeta(r, \omega)$. Then, a regression on the experimental and measured transfer function is applied to determine the experimental attenuation curve $A_R^E(\omega)$. Finally, an inversion problem is solved to find the estimated material damping profile.

f – *k* analysis combined with the half-power bandwidth method

This method is proposed by Badsar [7]. It uses the half-power bandwidth method or Q factor method to estimate the attenuation curve from measured data. It is based on the width of the peaks in the *f* – *k* domain. In analogy with the SDOF system, if the attenuation is weak, the peak is high and narrow while if the attenuation is strong, the peak is low and wide.

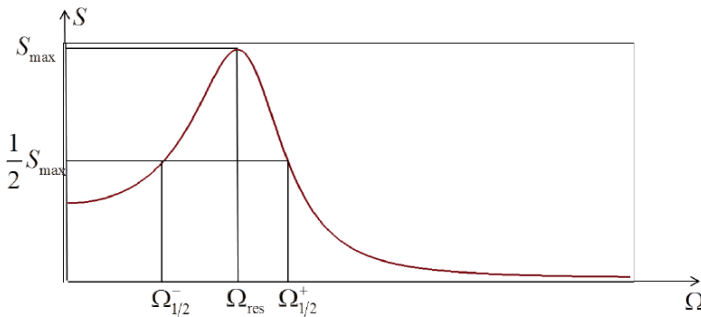


Figure 3.8: Half-power bandwidth method for SDOF [29].

In structural dynamics, the quality factor method is used to determine the modal damping ratio from the width of the peaks in the frequency domain at the magnitude of $1/\sqrt{2}$ times the peak value. Equation 3.11 refers to a weakly damped SDOF system:

$$\zeta = \frac{\Delta\omega}{2\omega_{res}} \tag{3.11}$$

where, ω_{res} is the resonance frequency for the undamped system. The temporal decay rate can be then computed, considering that $A = \omega_{res}\epsilon$, as following:

$$A = \frac{\Delta\omega}{2} \quad (3.12)$$

The method can be extended to MDOF systems with widely spaced resonance frequencies ω_{res_n} . In order to avoid mixing of peaks, a more general formula is proposed where the parameter γ , which defines the magnitude where the bandwidth $\Delta\omega$ is calculated.

$$A = \frac{\Delta\omega}{2\sqrt{\gamma^{-2} - 1}} \quad (3.13)$$

where, γ is allowed to vary between 0 and 1 and must be chosen carefully. If γ is too low, mixing of peaks can happen while, if γ is too high, due to the resolution of the measured data, errors in the actual width of the peaks can be introduced. Equivalently, the half-power bandwidth method can be applied to the response of a layered half-space in the $f - k$ domain. In this case, at every frequency ω , the peaks of each mode is identify and the corresponding bandwidth of the peak is determined along the wavenumber axis, resulting in $\Delta k_r(\omega)$. The general definition of the modal spatial decay or attenuation curve is given by Equation 3.14.

$$A_R^E(\omega) = \frac{\Delta k_r(\omega)}{2\sqrt{\gamma^{-2} - 1}} \quad (3.14)$$

This method can be also applied to multi-mode analysis since each attenuation curves can be computed separately and then used simultaneously together for the damping inversion. It is also worthy to report that, starting from the measured data, it is possible to define the phase damping ratio $D(\omega)$ as:

$$D(\omega) = \frac{A_R^E(\omega)}{k} \quad (3.15)$$

Since the measured data are limited, a truncation is introduced in the integration which causes a widening of the peaks. Indeed, a limitation in the spatial sampling due to a limited range of measurement leads to a widening of the spectrum and therefore in an overestimation of the material damping. In order to get rid of this error, an artificial exponential window $\hat{w}(r, \omega)$ can be applied in the space-frequency domain. This is basically an introduction of additional damping. The window $\hat{w}(r, \omega)$ is defined as following:

$$\hat{w}(r, \omega) = e^{-\hat{A}_{art}(\omega)r} \quad (3.16)$$

where $\hat{A}_{art}(\omega)$ is the decay rate for the exponential window. For each frequency, this rate is computed as the smallest non-negative value that satisfies the following inequality which limits at q that the amplitude ratio between the farthest and the nearest receiver:

$$\frac{|\hat{w}(r_{max}, \omega) \hat{H}_{zz}^E(r_{max}, \omega)|}{|\hat{w}(r_{min}, \omega) \hat{H}_{zz}^E(r_{min}, \omega)|} \leq q \quad (3.17)$$

where r_{min} and r_{max} are respectively the position of the nearest and farthest receiver and $\hat{H}_{zz}^E(r, \omega)$ is the transfer function which is assumed in this work to be equal to the response spectrum since the source spectrum is almost constant in the range of interest (remember $\hat{H} = \hat{S}_{uu} / \hat{S}_{FF}$, where \hat{S}_{uu} is the response spectrum and \hat{S}_{FF} is the source spectrum). This consideration will be extended and applied to the measured data in Chapter 6 together with choice of the parameter q .

Then, the attenuation curve is computed by using the Equation 3.14 and the true attenuation curve, which is used for estimating the material damping, can be retrieved by subtracting the artificial decay $\hat{A}_{art}(\omega)$ to the computed curve $A_R^E(\omega)$.

Comparison of methods

Badsar [7] uses three benchmark problems to compare the proposed techniques: a regular soil profile (a soft layer over a stiffer half-space), an irregular soil profile (a soft layer between the stiffer top layer and the half-space), and a profile with a smooth variation (stiffness increasing with depth). From the comparison, it turned out that the new simplified method (half-power bandwidth method) yields to equal or even better results for all the three considered profiles especially due to the fact that this method can deal with the occurrence of higher modes treating them separately.

Moreover in the new technique, the computation of the geometric attenuation coefficient is not requested since a smart wavenumber transformation is applied, therefore, this method is not affected by the error introduced in the first two techniques due to the computation of the geometric spreading. Moreover, this work aims at including also the higher modes in the analysis so then this method is suitable for this purpose. Therefore, in this thesis the half-power bandwidth method will be used to estimate the attenuation curves from measured data.

It seems worthy to highlight a final remark. The estimation of the attenuation curve is not affected by the estimation of the shear velocity (which comes from the stiffness inversion) since it is derived directly from the measured data.

3.5 Damping inversion tool

In this section, the characteristics of the damping inversion tool are reported. First, an overview of the proposed tool is presented along with some specifics of the implementation. Then, the main steps of the inversion are extensively discussed. Finally, three specific functionalities (wavelet compression, misfit function and inversion algorithm) are explained in details.

The proposed damping inversion tool follows the general characteristics of the inversion method reported in Section 3.1. The goal of this tool is to find the best match between the measured attenuation curve (see Half-power Bandwidth Method) and the theoretical attenuation curve derived with the surface wave models presented in Chapter 2. In this case, the set of parameters that is allowed to vary is the material damping ratio of each layer which is included in the theoretical model with the relation 2.65. The other parameters are not allowed to vary since it has proved by [5] that they do not largely affect the results.

The Tool has been developed in order to run on the in-house cluster (5125 cores available) which highly increases the computational power and drastically reducing the time needed for each iteration. The program uses an executable file, which is the main core of the inversion process containing all the functions needed for the computing the objective function, and it is run for each member of the searching domain. Each iteration is performed by using a batch file which includes the executable file and the input file for each soil profile.

The Damping Inversion Tool is made of three principal steps (pre-processing, iterative process and post-processing) which contain several sub-steps; some are performed only once while others are repeated for each iteration. A schematic of the Damping Inversion Tool is presented in Figure 3.9.

The pre-processing deals with the operations that has to be taken in order to compute the so-called measured attenuation curve. It is assumed that the collected data are already taken in the f-k domain by using a Hankel transform which gets rid of the geometric damping. Then, the half-power bandwidth method is applied to compute the measured attenuation coefficient as a function of the frequency. In this step for each frequency, the roots are found directly on the measured spectrum and the maximum (which corresponds to the roots) is estimated by using a finding peaks tool implemented by the author. If a multimodal analysis is requested, the different attenuation curves have to be calculated separately considering each mode. In this operation, a crucial importance is given to the choice of the γ value: due to the limited resolution of the data it is suggested to use the standard value $\gamma = 1/\sqrt{2}$ in order to have a better characterization of the peak. The amount of

data collected in this phase is too high for performing a damping inversion with the actual computational power. Indeed, it has to be considered that for each iteration of the main process, the complex roots have to be computed for each member of the population and this requires the calculation of the determinant in the complex wavenumber plane (see 3.3.2) which is the most expensive part computationally speaking. Depending on the dimension of the coefficient matrix, each root may take between 30 and 60 seconds to be computed. If it is considered a standard situation with 300 roots, 80000 members and 10 iterations, it is easy to understand that this is not meaningful in practical terms, especially on a local computer. A more detailed study on the computational time is presented in Section 4.3. So, it is necessary to describe the attenuation curve with a reduced amount of points. For this reason, the wavelet compression method (explained in Section 3.5.1) is applied to the measured attenuation curve. The attenuation curve as function of the frequency and the location of the elastic roots are the two set of data that are used as a reference in the next step of the Damping Inversion Tool. Finally, it is also possible to attribute to the pre-processing step the generation of the first population, see 3.5.3.

The iterative process is the part of the tool which repeats certain action in each iteration whose number is set by the user. Each iteration includes all the steps that lead to the computation of the theoretical attenuation curve for each member of the population, the comparison with the measured one and the generation of the new population for the next iteration. The elastic roots picked from the response spectrum are used as the starting point for computing the damped roots of the theoretical model with the method explained in Section 3.3.2. The determinant of the coefficient matrix depends on the type of the wave which is under analysis (see Chapter 2). The theoretical attenuation coefficient is computed as explained in Section 3.4.1. The key component of the inversion problem is the objective function, see Section 3.5.2. It is used to compare the two attenuation curves and is computed for each member of the population. Then, starting from the a best percentage of the results of the actual searching domain, a new population is generated and the next iteration is ready to run. The iterative process is based on a modified random search method (see Section 3.5.3) which uses some properties of the searching domain in order to reduce the number of iterations and guarantee a faster convergence.

The last step of the Damping Inversion Tool is the post-processing. Once the number of iteration is reached, the final estimated material damping profile is computed and the estimated attenuation curve is visually compared with the measured ones to identified the discrepancy as a function of the frequency which is the starting point for the frequency damping dependency analysis presented in Chapter 7.

In the next sections, specific details will be presented about the wavelet compression, the misfit function and the inversion algorithm.

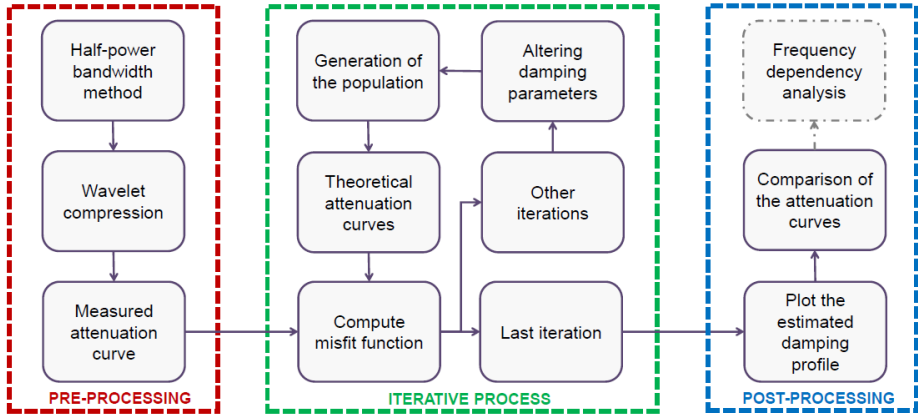


Figure 3.9: Flow chart of the implemented Damping Inversion Tool.

3.5.1 Wavelet compression

Generally, it has been noticed that an inversion process on measured data is more sensitive to the shallow layers of a layered half-space since most of the information can be gained from the fundamental mode (where most of the energy lies) which is mostly affected by the shallow layers as shown in Section 3.2. Moreover, as presented in Section 4.3, the runtime of the damping inversion is proportional to the number of roots included into the analysis. In order to overcome this two issues, it is necessary to find a smart way of selection of the roots to give more weight to the layers with less sensitivity (deeper layers and half-space) and reduce the overall number of roots and therefore save time. To achieve this result, a data compression technique is needed.

Inspired by [26], the wavelet compression method is applied to the present problem. In analogy to the compression which can be applied to the Fourier transform by eliminating some of the frequencies which compose the signal without degrading the original signal itself, the wavelet compression is an iterative process which uses local polynomial functions (linear or quadratic) in order to map a function with size and resolution determined locally. This means that the compression parameters can be set finer for in the locations where it is needed and this helps to solve the first problem presented in this section. How does the wavelet compression works? First, the signal is sampled with a generic mesh (in the present application the function is already sampled since it is composed by a finite number of points/roots, therefore

the resolution is defined), then locations where to apply the compression are evaluated and the needed tolerance is set. The compression scheme is defined in Figure 3.10 where an intermediate iteration of the wavelet compression scheme is shown. In the first iteration, only the odd points (green points) are considered and a linear polynomial is determined between each of them. If the distance between the even points is higher than the tolerance the points are kept otherwise they are discarded. In the next iterations, the process is perfectly repeated considering the remaining points from the previous iteration.

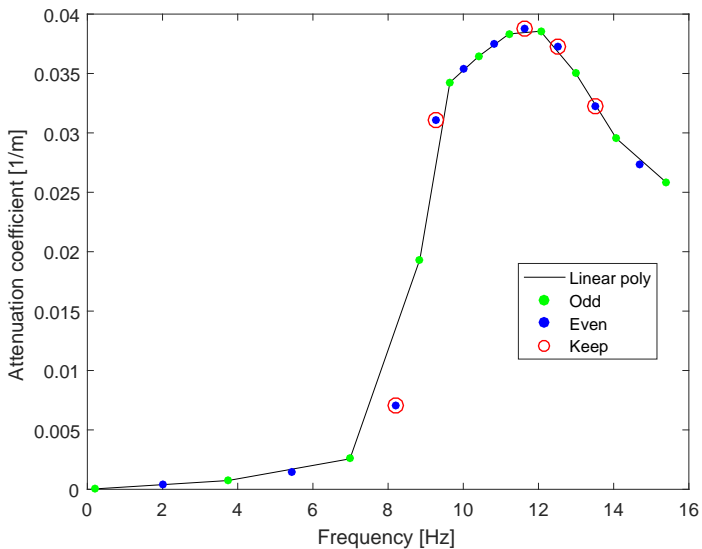


Figure 3.10: Intermediate iteration of the wavelet compression method for a generic attenuation curve.

In the different iterations, lies the multi resolution nature of the wavelet compression method. The resolution determines the detail of the signal while the tolerance controls the quality of the approximation. In this work, the resolution is determined by the grid in the fk domain while the tolerance is set in order to preserve the peaks of the attenuation curves and give more weight to the deeper layers and the half-space by keeping more roots in the low frequency range. An example is shown for TC3 profile in Figure 3.11.

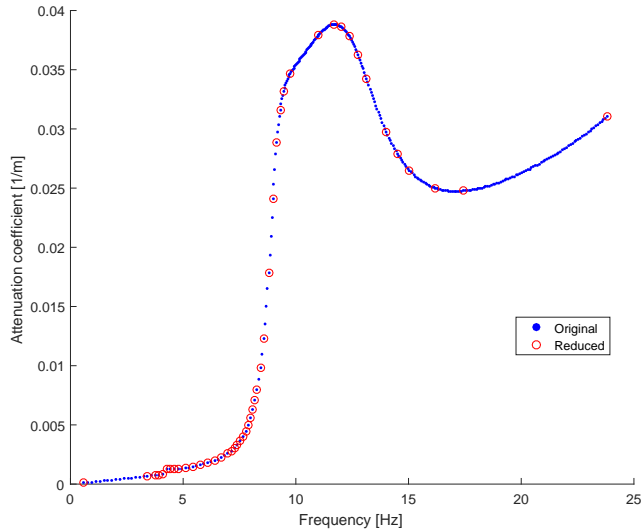


Figure 3.11: Original and reduced attenuation curve for TC3 soil profile.

3.5.2 Misfit function

As said in Section 3.1, the inversion problem can be seen as an optimization problem in which the misfit function (or objective function) has to be minimized by varying the material damping ratio of the layers of the system. In the previous thesis [5], the phase damping ratio was chosen for defining the objective function of the damping inversion. Considering the definition of the damping ratio in Equation A.7, it is possible to observe that it presents a ratio of the imaginary part and the real part of the complex wavenumber both elevated to the power of 2. The location of the roots - real part of k - is picked from the measured data spectrum and the imaginary part is computed with the method proposed, therefore they are both subjected to uncertainties, related to the resolution of the data and the numerical nature of the root finder, which blow up when they are elevated to the power of 2. Thus in this work, the attenuation coefficient has been chosen as the key parameter for the damping inversion. It is defined by Equation 3.5 as the imaginary part of the wavenumber. This helps in reducing the errors related to the computation of both the theoretical attenuation curve (as just explained) and the measured one since the damping ra-

tio from the data can be computed as $\zeta = A_R^E(\omega)/k$, where k is again subjected to uncertainties.

The misfit function is defined as the normalized difference between the measured and the theoretical attenuation curves:

$$\epsilon = \frac{1}{N} \sum_{i=1}^N \left| \frac{A_R^E(\omega)_i - \alpha(\omega)_i}{A_R^E(\omega)_i} \right| \quad (3.18)$$

where N is the number of roots (points which define the attenuation curve), $A_R^E(\omega)_i$ is the measured attenuation coefficient of the i -th root and $\alpha(\omega)_i$ is the theoretical attenuation coefficient of the i -th root.

The properties of the misfit function have been studied using the test profile TC1 whose characteristics are specified in Table 3.1.

Table 3.1: Properties for TC1 soil profile.

Layer	Thickness [m]	C _p [m/s]	C _s [m/s]	ζ_p	ζ_s	ρ [Mg/m ³]
Water	5	1500	0	0.00	0.00	1.0
1	5	1000	100	varying	varying	2.0
Half-space	∞	1000	200	varying	varying	2.0

In Figure 3.12, the misfit function of the TC1 profile is presented as function of the material damping of the two layers. It is possible to observe that the function presents just one minimum and it has a clear smooth trend. No local minima are observed. This property is used in the construction of the inversion algorithm which will be presented in the next section.

3.5.3 Modal inversion algorithm

In this section, the novel inversion algorithm is presented along with its more relevant features. The present algorithm can be seen as a modified random search method. A classic stochastic methods is useful when the problem is ill-structured and there are many unknown parameters involved and it guarantees the convergence in probability. As for the random search algorithm, in the proposed method, the samples are taken arbitrarily in the searching region but the convergence is ensured by the properties of the objective function combined with a constriction of the searching domain and not by simply iterating the process in the same region till the probability convergence is reached. Therefore, the modified method guarantees a faster convergence with respect to a classic random search method. The proposed

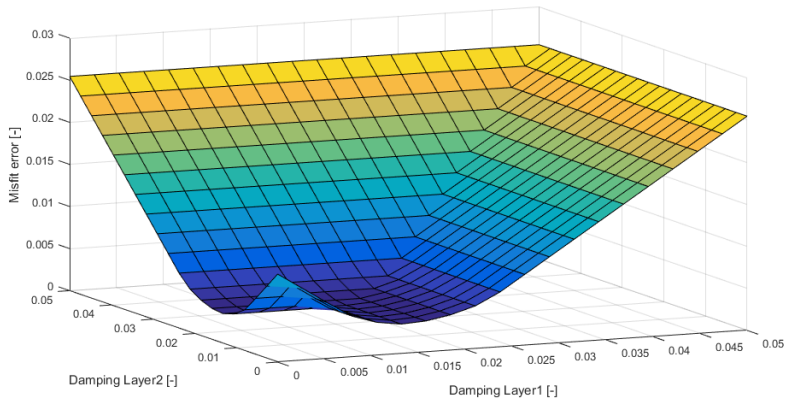


Figure 3.12: 3D plot of the objective function - TC1 profile.

algorithm is subdivided into three main parts: pre-processing, computation of the misfit error, post-processing.

The pre-processing is the phase which includes the definition of the searching domain and the generation of the population. For each layer, the searching domain represents the range of values between defined extremes that the material damping ratio can assume in each different iteration. The initial ranges can be defined by an educated guess deriving by qualitative understanding of the problem or by a blind guess allowing the material damping ratio to vary in a wider region. To generate the population, some values are picked from each domain in order to create combinations (with different layers) which give rise to material damping profiles. Two properties of the searching domain are relevant for reducing the number of iterations and the computational time: discretization and re-ranging. The values of the material damping of each layer is chosen by using a equally spaced grid which covers uniformly the domain. With respect to the traditional random methods, this characteristic guarantees that the values are well spread in the whole domain and not randomly picked. Considering the smoothness of the objective function (see Section 3.5.2), the assumption of determining a small number of points in the ranges is reasonable because no other minima are present and then there is not risk of falling into a local minimum. On the other hand, the re-ranging is used to reduce the ranges of searching of the next generation. Therefore in each layer, the searching domain is reduced at the beginning of each iteration by setting new boundaries defined in the

post-processing or the iteration itself. It can be easily notice that this feature uses the smoothness of the objective function to get a faster convergence of the algorithm. Once the searching domain is defined, the population is bred. The population is the set of soil profiles in which only the damping profile is different and it corresponds to the one of the combination generated previously. Basically, the tool attributes to each member (i.e. soil profile) of the population one of the possible damping combination defined in the searching domain. The population is then sent to the second step of the inversion algorithm. The disadvantage of the proposed algorithm is that the population must be very large in order to cover uniformly the entire domain. Nevertheless, the total number of iterations is reduced due to the aforesaid properties.

The second part of the algorithm computes the misfit error - or equivalently the suitability $s = 1 - \epsilon$ - between the attenuation curve generated by each member of the population and the reference attenuation curve of the measured data. First, the algorithm computes the attenuation curve of the forward model in which damping is introduced following the material damping profile corresponding to the present member. Second, the misfit error is computed by using Equation 3.18. Finally, this value is then stored associated to the relative damping profile. Once all the members of the population have been treated, the algorithm moves to the last step.

In the post-processing, the algorithm performs some statistics on the results collected in the previous phase and defines the ranges of search for the next iteration. In order to have a representative number of data, it has been chosen to consider the best 3% of the population for computing the results of each iteration. This assumption comes from sensitivity study on the synthetic damping inversion performed. In those cases, it came out that the 3% of the population - which will be called "best population" - was suitable for giving reliable results. In this phase, the mean value and the standard deviation of each layer of the best population are computed. These represent the parameter with which the new boundaries of searching domain are defined. For each layer, the ranges are set as the mean value \pm the standard deviation. Then, they are used in the pre-processing phase of the next generation to create the new domain. In the last iteration, the mean results in the final estimated value of the material damping and the standard deviation defines the confidence interval of the obtained inversion results.

Few remarks on the inversion algorithm are added in conclusion. In a preliminary analysis, a genetic algorithm has been judged unsuitable by the author for the present application due to its intrinsic randomness and its slow convergence speed (usually a decent size of the population and many generations are needed for convergence). A gradient based algorithm has been tested during the implementation

but it resulted unsuccessful. It is possible that it was requesting very small increments to get convergence, which is not suitable for the computational time of the damping inversion, and also the convergence speed is strictly related to the initial guess. Moreover in further research, it would be worthy to test other types of algorithm as a flocking based algorithm or the Genetic Flock Algorithm proposed by [9], which is a combination of a genetic algorithm and a particle swarm optimization. Finally, it can be also suggested the use of a combined technique by applying first the proposed global method and then a local optimization method to increase the convergence speed and the precision when the solution is already close to the minimum.

Chapter 4

Model Studies

This chapter aims to achieve a better understanding of the model presented in Chapter 2 by performing sensitivity analyses and inversion tests. Moreover, some limitations of the model are investigated. In conclusion, the direct implications for the damping inversion are discussed.

4.1 Sensitivity to stiffness

As [5] shown in his work, stiffness and damping analyses can be considered uncoupled since the shifting of the dispersive response in the f - k domain depends on the amount of damping and, for realistic damping values (0–10%), the averaged shifting is less than 2%. This leads to a more robust estimation since stiffness and damping are computed separately: the stiffness is first estimated and then the damping is estimated. In this section, sensitivity tests to stiffness are performed on the attenuation curves in order to get a better understanding of how an error in the computation of the elastic roots may affect the damping estimation. In these tests, the stiffness (in terms of shear wave velocity) is incremented by steps $\Delta C_s = 5\%$ in the range 0–25%. The soil profile chosen for this analysis presents a water layer with thickness equal to 5m, three intermediate layers 3m thick and a half-space. TC3 soil profile is shown in Table 4.1, presents an overall normally dispersive shear waves velocity profile with an inversion in the middle layers and a decreasing soil damping profile.

From Figure 4.1, it is possible to observe that the forward model behaves as expected since, by increasing the stiffness, the response moves to higher frequencies. In analogy with a single degree of freedom SDOF, it is useful to recall the expression

Table 4.1: Properties for TC3 soil profile

Layer	Thickness	Cp	Cs	ζ_p	ζ_s	ρ
Water	5	1500	0	0	0	1.0
1	3	1500	100	0.05	0.05	1.8
2	3	1500	200	0.035	0.035	2.2
3	3	1500	100	0.02	0.02	1.8
Half-space	∞	1500	400	0.01	0.01	2.3

of the eigenfrequency $\omega_n = \sqrt{\frac{k}{m}}$ since each of the points of the graph represents a couple wavenumber-frequency for which the undamped system resonates. The formula underlines that a stiffer system resonates at higher frequencies, in agreement with Figure 4.1. Varying the stiffness, the amount of damping does not change, indeed only a horizontal shift is observed. This is a confirmation of the uncoupling between damping and stiffness which is at the basis of the 2 steps inversion method proposed in this work and in [5]. The analysis has shown (Figure 4.2) that the average horizontal percentage shift is linearly related to the homogeneous percentage increase of the stiffness profile and the variation ratio (percentage shift over increasing of stiffness) is about 1/9.

4.2 Sensitivity to damping

In this section, the sensitivity to damping of the attenuation parameter chosen for describing the present model is verified and analysed. The study is carried out by using the TC3 soil profile. First, the damping ratio is incremented homogeneously by steps $\Delta D = 5\%$ in the range 0 – 25%. The results can be observed in Figure 4.3.

As expected, the visible shift is only vertical meaning that the roots move proportionally towards the complex plane $k_{re} - k_{im}$ when the material damping is increased. Moreover, the curves show a direct reaction to the variation of damping since, e.g. a 5% of variation in damping causes a 5% shift for the attenuation coefficient (Figure 4.4). Also, the sensitivity of the homogeneous variation of damping is equal for the different modes as shown in Figure 4.5. The graphs shows the percentage variation of the migration of the attenuation curves for a homogeneous +/-20% variation of the material damping. The percentage variation is intended as a percentage change of the reference value of each soil layer of the TC3 profile. The small oscillations can be attributed to numerical errors or local failure of the root finder tool but the overall trend clearly shows a similar behaviour of the three

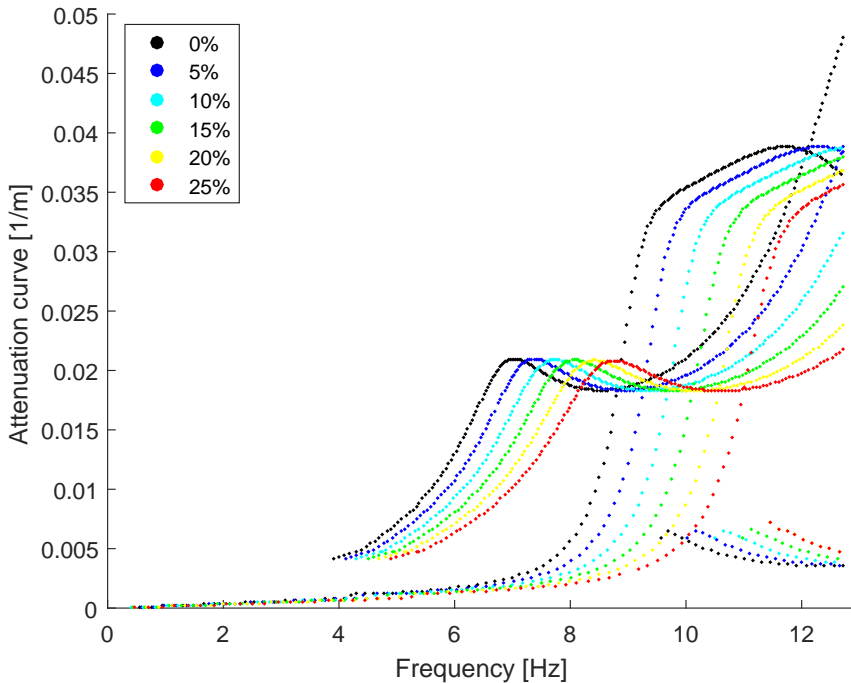


Figure 4.1: Phase damping ratio curves migration under the influence of increasing soil stiffness for TC3 soil profile

modes. Finally, a differentiated damping variation per layer is applied to the fundamental mode. The material damping is varied per soil layer keeping the others unmodified. Figure 4.6 shows the results of the analysis for a 5% damping variation for the fundamental branch of the attenuation curves. Clearly, it is possible to observe that the shallow layers (first and second layer) present an impact on the phase damping curves for mid-high frequencies while the sensitivity to the halfspace lays in the lower frequencies, where for very small frequency contents the impact is almost direct (5% variation in damping determines a 5% variation in the attenuation curves). These curves have a lower sensitivity with respect to the middle layers, in fact the percentage variation of the third layer is lower than 0.5%. The mentioned aspects should be taken into account while applying the wavelet compression 3.5.1.

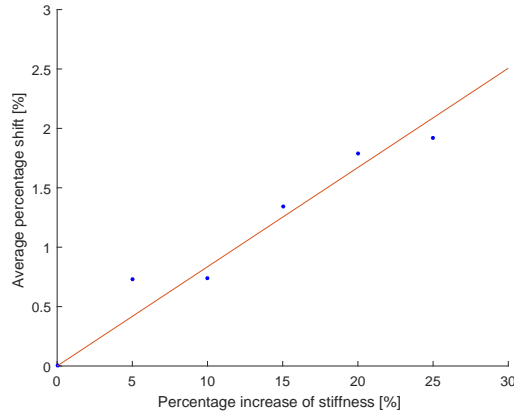


Figure 4.2: Average horizontal percentage shift versus percentage increase of stiffness for TC3 soil profile.

4.3 Time comparison

In this section, TC3 is used for performing a computational time analysis for optimizing the inversion process. In particular, two parameters are considered: the number of member of the population (see Section 3.5.3) and the number of roots kept by the wavelet compression (see Section 3.5.1). Together with the number of layers which determines the dimension of the coefficient matrix and cannot be extremely reduced, these variables affect mostly the inversion computational time. The first determines the number of computations of the misfit error in each iteration which is given by the number of points selected per layer to the power of the number of layers. While, the number of roots affects the duration of each computation. Since an ideal inversion considering an high amount of members and roots is not feasible for time reasons (consider that the damping inversion for Gjoa dataset could take around two weeks on a local computer), this study aims to gain a better understanding on which parameter has to be increased more. The analysis consists of nine simulations combining three levels for both the members and the roots. On the out of plane coordinate, a combination of the computational time, the percentage error and standard deviation of the top 3% of the results is presented. The simulations are

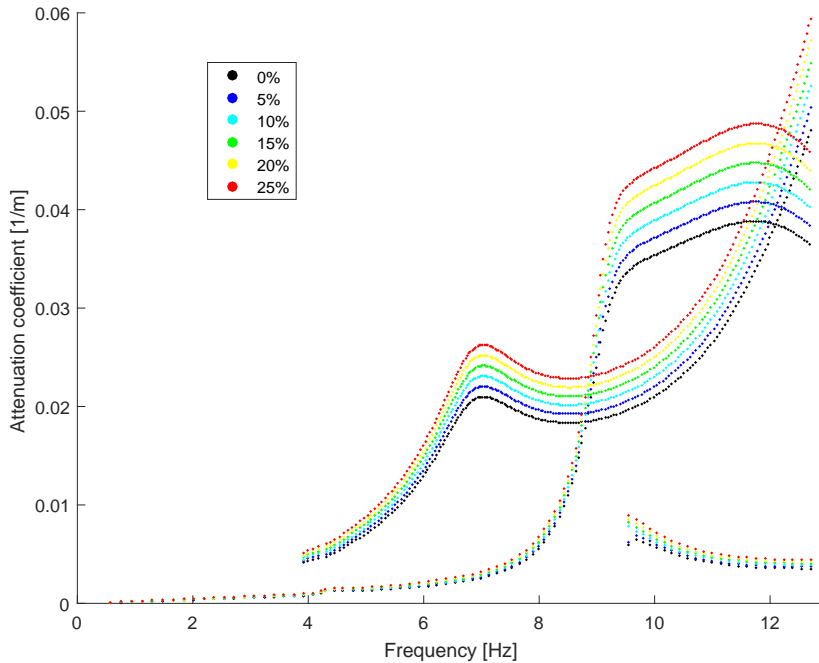


Figure 4.3: Attenuation curves migration under the influence of increasing material damping for TC3 soil profile - (Homogeneous percentage change of the reference value of the material damping).

performed on a local computer on a i5-4300M CPU of 2.60Hz using Matlab Parallel Pool with 2 workers. In Figure 4.7 the results of the analysis are presented.

From the graph, it is possible to observe that the best combination appears for the maximum number of roots and members of the population. As said, this combination is not feasible for the damping inversion. On the other hand, it can be noticed that good results can be obtained for a medium value of roots/members combined with the highest values for members/roots; the suitability is about 0.85. Developing the roots finder tools, it has been found that the computation of the damped roots is very expensive therefore, the combination medium number of roots and high number of members of population will be applied to the measured data inversion. However, the

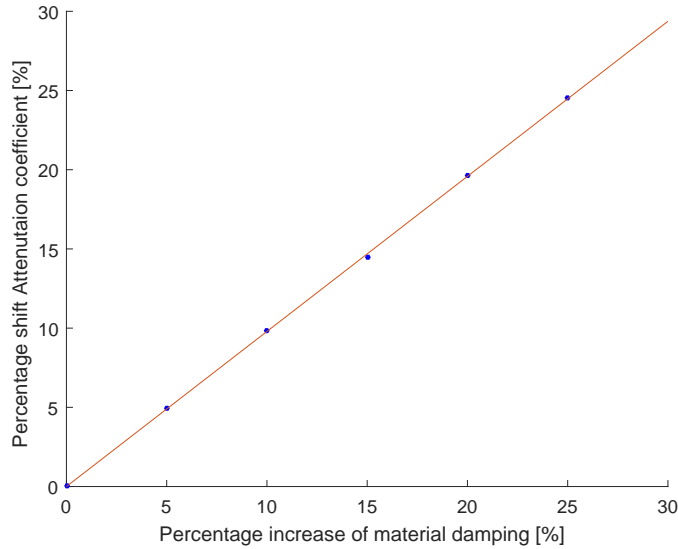


Figure 4.4: Percentage shift of the attenuation curves versus the homogeneous percentage change of the reference value of the material damping.

results are really close to each other since the bar shows that the minimum of the normalized variable is about 0.75. Nevertheless, this analysis should be considered only as an indicative study because the real damping inversion could be affected by other uncertainties. Moreover, other runs and combinations as well as different soil profiles are needed to draw definitive and quantitative conclusions.

4.4 Merging layers

As said in the previous section, the computational effort of the damping inversion is mostly related to the number of layers of the theoretical model. Indeed, it affects both the dimension of the population and the dimension of the coefficient matrix that has to be calculated for each root in the inversion process. In the present case, the Gjøa stiffness profile derived by [5] during the stiffness inversion is not feasible for the proposed damping inversion. In fact, a 12 layers overlying a halfspace soil system in which the damping value of each layer is allowed to assume 5 different

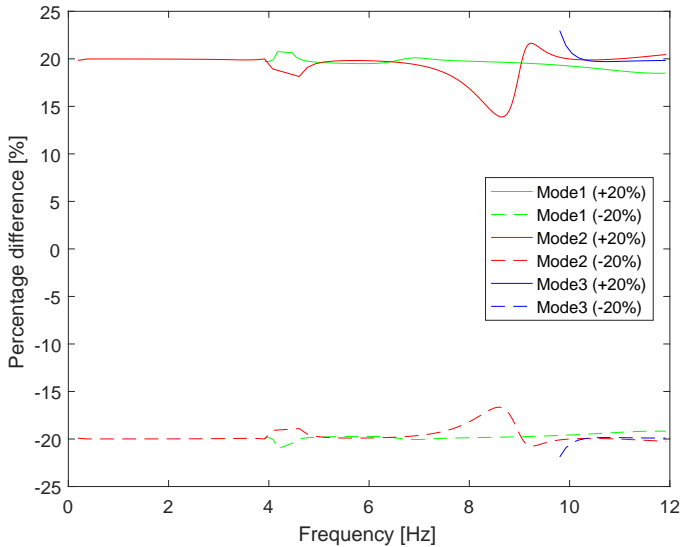


Figure 4.5: Percentage migration of the different branches of the attenuation curves for a $\pm 20\%$ variation of the material damping for TC3 soil profile.

values in each iteration gives rise to 1.220.703.125 members of the population which is computationally inoperable. In this section therefore, an analysis about how to merge the layers of the estimated stiffness soil profile (Table 4.2) is performed in order to study the effects on the attenuation curve. A definite reduction of the number of layers for the Gjøa profile will be proposed in Section 5.3.

In this study, 12 profiles have been generated starting from the reference one and, in each of them, two adjacent layers were merged together and the resulting properties have been obtained by using a weighted arithmetic mean. Then, the attenuation curve of the fundamental mode of each profile is computed and compared with the original curve in Figure 4.8. Moreover, the average percentage errors for each combination are presented in Table 4.3.

Visually, it is possible to notice that most of the attenuation curves are very close to the original one especially for high frequencies where they overlap. Two cases (combinations 23 and 34) present a prominent separation. This would suggest that merging layer 3 with the adjacent layers has a high impact on the attenuation curve. This trend is indeed confirmed also by the results shown in Table 4.3. Similar judge-

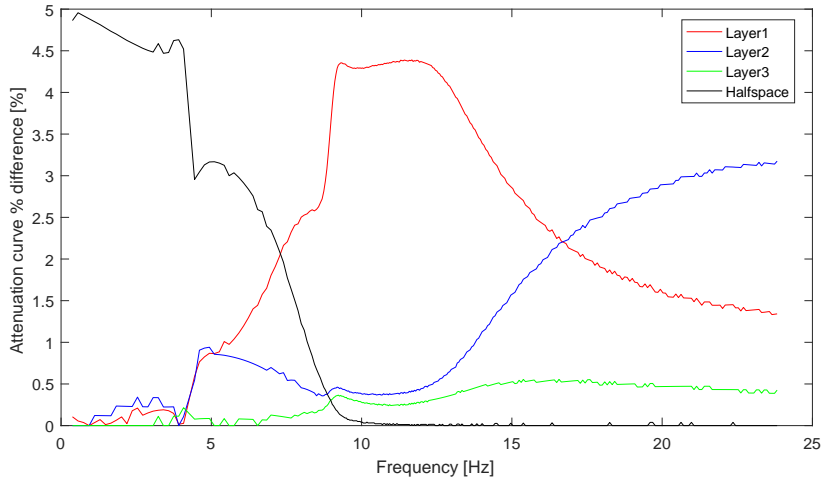


Figure 4.6: Percentage migration of the fundamental branch of the attenuation curves for a +5% variation of the material damping for each different layer for TC3 soil profile.

ments may rise comparing the other combinations such as combination 4-5 which has an error higher than 8%. Starting from these analyses and considering that it is requested a better resolution in the shallow layers, it is possible to define a new profile which will be characterized by 6 layers overlying a halfspace. The different layers are merged by considering the sensitivity of the attenuation curve to the different layer combinations. The final proposed profile is presented in Table 4.4. This will be then used in the stiffness inversion tool to estimate the associated C_s velocity profile and later used for the damping inversion.

4.5 Synthetic inversions

In order to test the damping inversion algorithm, two inversions on synthetic data are performed by using the profiles TC3 and TC5. Both the analysis are carried out considering only the fundamental mode since a single mode inversion will also be the first attempt of the measured data inversion. Figure 4.9 shows graphically the results of the damping inversion of the TC3 soil profile while Table 4.5 shows the

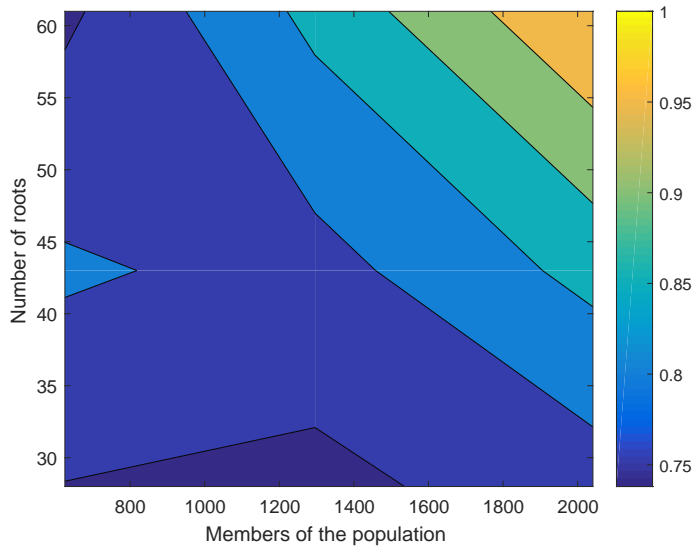


Figure 4.7: Results of the computational time analysis on TC3 soil profile. The colour bar represents a normalized variable from 0 (worst) to 1 (best).

percentage errors. For this run, 3 iterations are performed with 625 members of the population. An initial blind guess is applied considering for each layer a searching domain between 0 – 5% material damping ratio.

From Figure 4.9, it is possible to observe that the best profile matches perfectly the true synthetic profile and the average error of the Top 3% is lower than 5% with a maximum error equal to 11% for the third layer. The convergence is faster for the top layer while the confidence interval is higher for the intermediate layers. At the end of the simulation, the confidence intervals are at least reduced by 80% of the initial blind guess highlighting a quick convergence of the algorithm as expected. Considering the limited amount of both the members and the iterations, this can be assumed as a good starting point for the developed damping inversion tool and it was also useful for verifying that all the features of the novel inversion algorithm were working properly.

A second synthetic inversion has been performed by using the TC5 soil profile (Table 4.6). The results are shown in Figure 4.10 and Tab. 4.7. In this case, the best

Table 4.2: Gjoa soil profile derived by [5].

Layer	Thickness	Cp	ρ	Cs Mean
Water	364.6	1500	1025	0
1	1	1500	1650	44.5
2	2	1500	1700	55.2
3	4	1500	1800	71.5
4	4	1500	1800	126.0
5	4	1500	1900	227.4
6	4	1500	1900	309.8
7	4	1500	2000	302.0
8	4	1500	2000	351.9
9	4	1500	2100	368.3
10	4	1500	2100	401.4
11	4	1500	2100	448.8
12	4	1500	2100	470.3
Halfspace	∞	1500	2100	493.9

Table 4.3: Average errors in the attenuation coefficient obtained by merging sequentially couples of layers for Gjoa soil profile.

Combination	Thickness	Cp	ρ	Cs Mean	Av. error [%]
1-2	3	1500	1683	49.8	3.6
2-3	6	1500	1767	65.2	15.6
3-4	8	1500	1800	98.8	17.9
4-5	8	1500	1850	176.7	8.2
5-6	8	1500	1900	268.6	6.0
6-7	8	1500	1950	305.9	5.4
7-8	8	1500	2000	327.0	6.0
8-9	8	1500	2050	360.1	5.2
9-10	8	1500	2100	384.9	5.1
10-11	8	1500	2100	425.1	6.2
11-12	8	1500	2100	459.6	4.7
Ext HS	∞	1500	2100	493.9	4.8

profile matches perfectly the true profile except for the second layer which presents an error equal to 4.3%. It is interesting to observe that the confidence intervals are wider for the shallow layers rather than the deeper ones. In particular, the value of

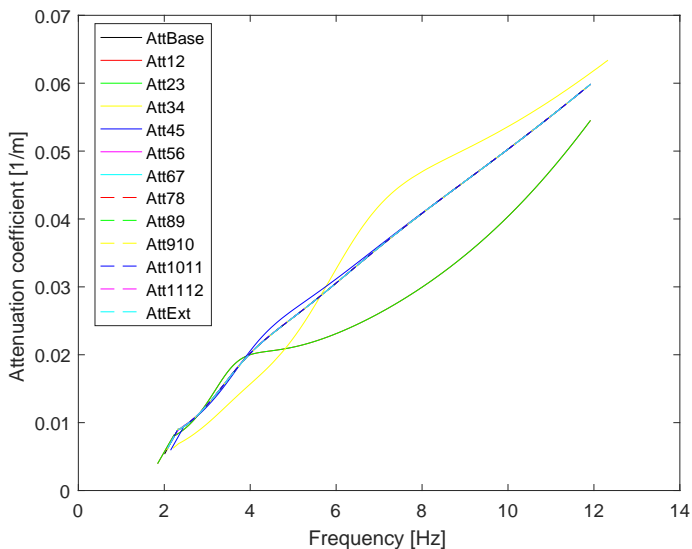


Figure 4.8: Comparison between the attenuation curves obtained by merging sequential couples of layers for Gjøa soil profile.

Table 4.4: Proposed reduced profile for Gjøa dataset.

Layer	Combination	Thickness	C_p	ρ
Water	-	364.6	1500	1025
1	1-2	3	1500	1683
2	3	4	1500	1800
3	4	4	1500	1800
4	5-6	8	1500	1900
5	7-8-9	12	1500	2000
6	9-10-11-12	12	1500	2100
Halfspace	-	∞	1500	2100

the halfspace is retrieved perfectly also for the top 5% of the population. This can be caused by the choice of the points kept by the wavelet compression. Indeed, this may affect largely the inversion if the distribution of these points tends to be very non uniform. Nevertheless, this reduction of points seems not to spoil the global

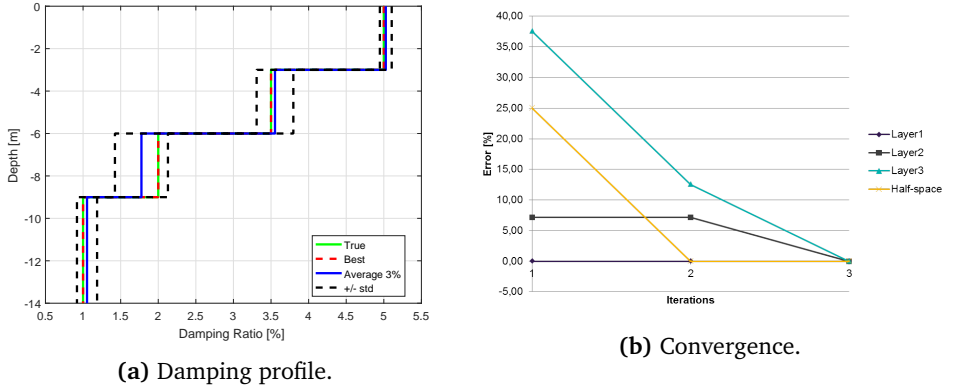


Figure 4.9: Damping inversion results for TC3 synthetic soil profile.

Table 4.5: TC3 Synthetic Damping Inversion Results.

Damping best profiles TC3					
	True	Best	Top 5%	Top 3%	Top 1%
Layer 1	5.0	5.0	5.0	5.0	5.0
Layer 2	3.5	3.5	3.6	3.6	3.5
Layer 3	2.0	2.0	1.7	1.8	2.0
Halfspace	1.0	1.0	1.1	1.1	1.0

Percentage error best profiles TC3					
	True	Best	Top 5%	Top 3%	Top 1%
Layer 1	-	0.0	0.8	0.6	0.0
Layer 2	-	0.0	2.6	1.4	1.1
Layer 3	-	0.0	13.0	11.0	0.0
Halfspace	-	0.0	5.0	5.0	0.0
Mean error	-	0.0	5.3	4.5	0.3

result of the inversion since the average error of the top 3% is very promising being lower than 4%.

Table 4.6: Properties for TC5 soil profile

Layer	Thickness	C_p	C_s	ζ_p	ζ_s	ρ
Water	5	1500	0	0	0	1.0
1	3	1500	100	0.03	0.03	1.8
2	3	1500	200	0.04	0.04	2.2
3	3	1500	300	0.02	0.02	1.8
Half-space	∞	1500	400	0.01	0.01	2.3

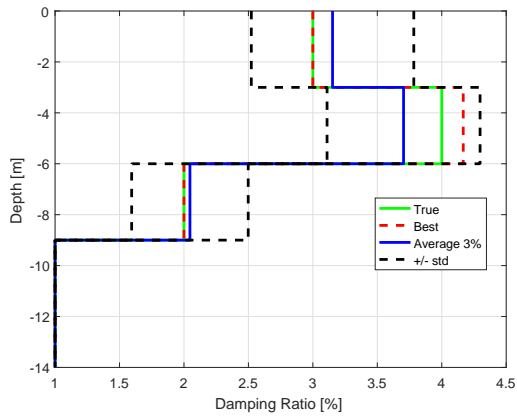


Figure 4.10: Damping inversion results for TC5 synthetic soil profile: material damping profile (3 iterations).

Table 4.7: TC5 Synthetic Damping Inversion Results.

Damping best profiles TC5					
	True	Best	Top 5%	Top 3%	Top 1%
Layer 1	3.0	3.0	3.1	3.2	3.1
Layer 2	4.0	4.2	3.6	3.7	3.9
Layer 3	2.0	2.0	2.1	2.1	2.0
Halfspace	1.0	1.0	1.0	1.0	1.0

Percentage error best profiles TC5					
	True	Best	Top 5%	Top 3%	Top 1%
Layer 1	-	0.0	3.3	5.0	3.7
Layer 2	-	4.3	10.0	7.5	3.0
Layer 3	-	0.0	7.0	2.5	0.5
Halfspace	-	0.0	0.0	0.0	0.0
Av error	-	1.1	5.1	3.8	1.8

4.5.1 Synthetic inversion: reduced frequency range

Before performing a damping inversion on measured data, a further observation needs to be mentioned and a new test to be carried out. Indeed, in the previous synthetic inversions, the attenuation curve of the fundamental mode has been considered in frequency range of 0-20Hz. In the Gjøa response spectrum instead, the data usable (where there is enough energy) for the inversion are only in the range 3-12Hz and especially they do not include any point in the non-dispersive region of the frequency-wavenumber domain. As explained in Chapter 3 and proved in Section 4.2, the very low frequencies of the fundamental mode are very sensitive to the halfspace properties and in particular to material damping ratio. A test inversion on TC5 profile is performed in order to estimate the error related to this lack of data. The inversion has the same characteristics of the previous test inversion on TC5 but the roots are picked only on the dispersive part of the fundamental mode in the frequency range 7-12Hz. In Figure 4.11, the results of the inversion are presented.

It is possible to observe that, after 5 iterations, the value of the material damping in the halfspace presents an error about 80% for the Top 3%. While, the error of the shallow layers is lower than 2%. This analysis shows that the lack of data in the non-dispersive part of the f-k response of the measured data will affect the results of the halfspace leading to an erroneous value. On the other side, no implications are noticed for the shallow layers while, for the deeper layer the error is increased

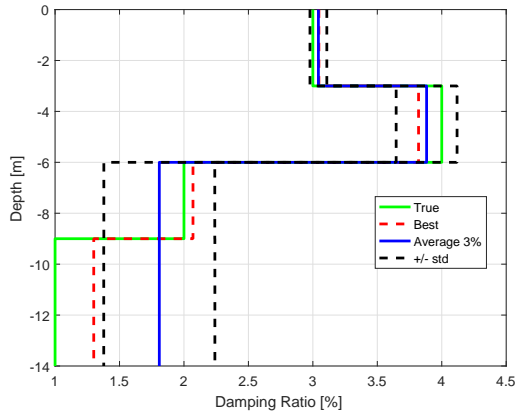


Figure 4.11: Damping inversion results with limited amount of frequency (7-12Hz) for TC5 synthetic soil profile: material damping profile (5 iterations).

with respect to the previous inversion even if the number of iterations is higher. This means that reducing the range of frequency considered, also the deeper layers are affected since, as shown in Chapter 3, the properties of these layers are caught by relative high wavelength (namely low wavenumbers or low frequencies). As smart use of the wavelet compression function is then needed in order to limit this unavoidable error.

4.6 Understanding phase damping ratio curves

Foti [15] states: “The phase damping ratio curves allow an intuitive assessment and evaluation of the attenuation data”. In fact, as it will be presented here, it is possible to retrieve crucial information about the material damping values in the extreme layers or the potential trend of the damping profile over the depth.

Recalling the considerations stated in Chapter 3, it is possible to say that the phase damping ratio curves give direct indications depending on the feeling of depth of the correspondent wavelength. To clarify this concept, the TC3 soil profile is considered and, in Figure 4.12, the phase damping ratio curves of the first three modes and the non dispersive part are shown as function of the wavenumber. It is important to remember that low wavenumbers (long wavelengths) feel deeper into the soil while high wavenumbers feel the shallow layers.

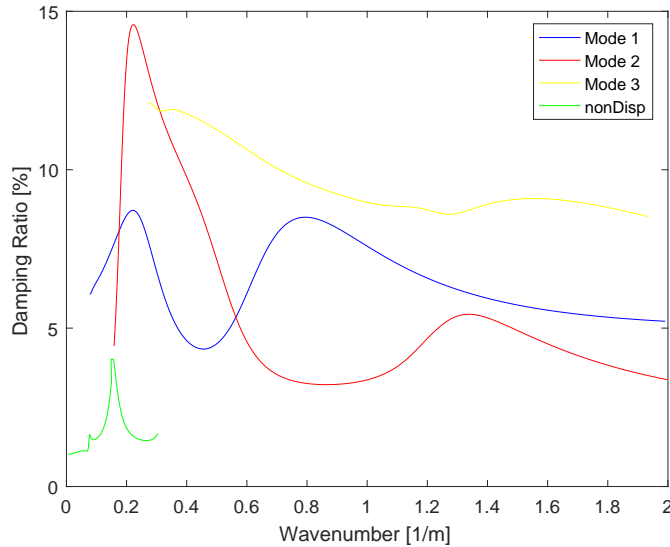


Figure 4.12: Phase damping ratio curves of the first 3 modes and the non-dispersive part of TC3 soil profile.

First, the non dispersive part is considered. As said in Chapter 3, the non-dispersive part feel mostly the halfspace properties. An extreme of this concept can be found by analysing what happens to the (green) curve when the wavenumber approaches zero. In this situation, the curve is feeling only the halfspace and indeed it reaches the value of the material damping ratio of the halfspace (1%). Then, considering the opposite extreme and the “mode shape” of the fundamental mode as shown by [5], it is clear that the (blue) curve associated to the fundamental mode approaches the value of the material damping (5%) of the top layer for high wavenumbers since the curve is only feeling the shallowest layer. For wavenumbers in between the two mentioned extremes, the phase damping ratio curves can be considered as the results of many contributions coming from the different layers depending on the “shape over the depth” of the mode itself. Nevertheless, due to this complex combination, it is hard to make further useful considerations in this region of the graph. For an ideal measurement in which the available data are spread over a very wide range of frequencies, the analysis proposed in this section can lead to an estimation of the material damping of the top layer and the halfspace without

actually performing any damping inversion.

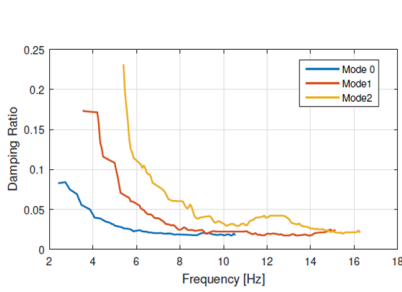
The phase damping ratio curves can also be used to get a qualitative prediction of the resulting material damping profile before performing the inversion. This analysis has been applied directly to the measured Gjøa dataset in order to get a qualitative guess which will be then compared with the profile obtained in the inversion process. Figure 4.13a shows the extracted modal damping curves from the Gjøa site. These are used as a reference for the present analysis. Then, three different theoretical models are generated by using the C_s velocity profile derived by [5] in the stiffness inversion for the Gjøa dataset. The first model presents a linearly increasing damping profile (from 1% to 7%) with depth which will be called the irregular profile. The second shows a linear decreasing damping profile (from 7% to 1%) and it is referred to as the regular profile. The third presents a constant value for the damping (3%) for each layer and it is called homogeneous profile. For each model, the phase damping ratio curves are calculated and shown in Figure 4.13 together with the extracted curves.

From Figure 4.13, it is observed that the extracted curves (Figure 4.13a) present few huge oscillations and never intersect each other. In the irregular profile (Figure 4.13b), the curves are separated and very smooth. In the regular profile (Figure 4.13c) instead, many oscillations and intersections are present. The homogeneous profile (Figure 4.13d) represents an intermediate situation. By performing a visual comparison, it is possible to observe that the extracted curves present some characteristics which are shared partly with the irregular profile and partly with the homogeneous one. Considering that there seems to be a smooth transition between the curves proposed by the different profiles, it is reasonable to assume that the resulting material damping profile for the Gjøa dataset is expected to be an intermediate combination between the irregular and the homogeneous profile.

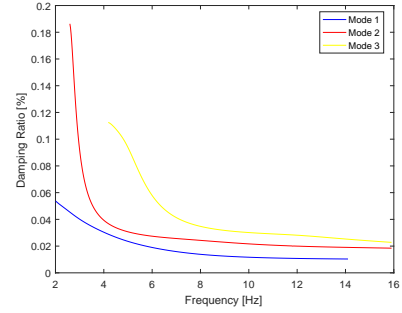
4.7 Conclusions on model studies

This section aims to study the proposed method in order to understand the possible implication for the measured data damping inversion. Here, some conclusions are presented.

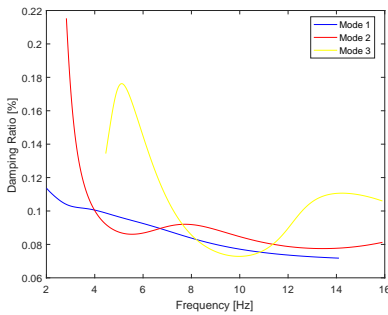
- The stiffness has a minimal impact on the phase damping ratio curves. The uncoupling of the inversion process can be confirmed in the fact that the homogeneous increase in the stiffness brings only a frequency shift of the phase damping ratio curves which is in average equal to 10% of the stiffness increase



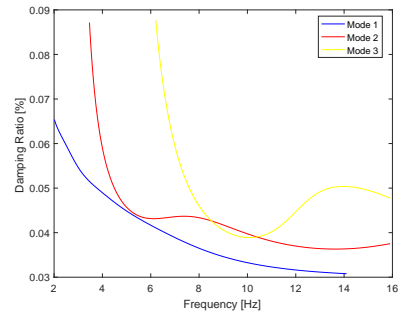
(a) Extracted phase damping curves [5]



(b) Phase damping curve of the irregular profile.



(c) Phase damping curve of the regular profile.



(d) Phase damping curve of the homogeneous profile.

Figure 4.13: Modal solutions for a one layer overlying a halfspace soil system.

itself.

- As expected, the damping ratio curves shows a direct impact of the homogeneous increase of the material damping with a variation ratio equal to 1 and a similar trend for each mode.
- The layers affect in a different way the phase damping ratio curves. The shallow layers influence mostly the mid-to-high frequencies while the sensitivity to the halfspace lays in the lower frequencies. These curves have a lower sensitivity with respect to the middle layers which is possible to understand when considering the wavelengths.

- Merging the layers of Gjøa profile is not only a compulsory action to take before the damping inversion, but can also give interesting information about the stratification of the soil. Further investigations are needed to compare the presented analysis with real estimated profiles. The reduction of the profile has been performed by taking into account the effect of this reduction on the attenuation curve. New stiffness inversions will be run to get the reduced shear wave velocity profiles for both Scholte and Love models.
- Synthetic damping inversions have revealed an excellent performance of the developed method yielding errors, in most of the cases, smaller than 5%. As expected, the highest errors are in the middle layers (error $\sim 11\%$).
- In order to get reliable results for the halfspace, information about the non-dispersive part of the f - k domain are needed. The lack of this data brings about large mistakes. A way to limit this error is to apply a smart wavelet compression (see Section 3.5.1) keeping more roots in the lower frequency range. Nevertheless, this cannot completely solve the problem. It is necessary to realize that, with this limited amount of data, the estimation of the damping material value of the halfspace is less reliable with respect to the other layers. However, it is also important to remember that, for practical purposes, the focus is more on the shallow layers which are the ones which contribute more to the soil-structure interaction damping.
- From the analysis of phase damping ratio curves, it is possible to directly retrieve, without performing any inversion, the material damping ratio of the extremes layers. Nevertheless, to do that, a large range of data, in terms of frequency/wavenumber content, is needed. This is rarely available in practice.
- Studying the shape of the extracted phase damping ratio curve, it is possible to predict qualitatively the trend of the material damping profile. In this case, for the Gjøa profile, a combination of a linear increasing and a constant profile is predicted.

Chapter 5

Stiffness Inversion

In the stiffness inversion process, the goal is to estimate the C_s velocity profile by finding the best match between the forward model and the measured results. In this chapter, the stiffness inversion is performed by using the inversion tool implemented by de Winter [13] and refined by Armstrong [5]. The aim is to derive new stiffness profiles that will be then used in the estimation of the material damping. For the first time in this project, the Love wave stiffness inversion is proposed. Moreover, the layering of the soil profiles is reduced according to the considerations presented in Chapter 4. Finally, some remarks and conclusion are discussed together with possible further improvements.

5.1 Gjøa dataset

The Gjøa dataset will be extensively presented in Chapter 6 along with the characteristics of the data collection and the post-processing needed before using the data in an inversion application. In this section, the focus is on the choice of the fundamental mode from the measured response spectrum shown in Figure 5.1. In order to do that, it is necessary to recall the considerations stated in Chapter 3. For definition, the tangent to the fundamental mode at high wavenumbers is passing through the origin of the f - k domain. Generally, the fundamental branch of the dispersion curve in a measured response spectrum can be identified as the first curve, moving from low to high frequencies, where a huge amount of energy is concentrated. In this case, it seems that the tangent to the fundamental branch (which has been picked by [5]) is not passing through the origin meaning that the choice of the fundamental mode is wrong and another branch has to be selected. Nevertheless, by a visual

analysis, it is not possible to find a clear concentration of energy moving towards lower frequencies and higher wavenumbers. Instead, a repetitive pattern is observed that will be explained in Chapter 6. Moreover, it is important to highlight that the condition for the tangent is valid only if an adequate high wavenumber is reached while for the Gjøa dataset the aforesaid branch is visible only till $k = 0.25 \text{ 1/m}$ which corresponds to a wavelength equal to $\lambda = 4m$ that is too high for being representative for the thickness of the top layer of the soil model. In conclusion, the available amount of data is not enough to exclude the picked mode from being the fundamental one on the basis of the tangent analysis, therefore the choice will stand on the original picked mode. To confirm its validity, a comparison has been performed with the choice made by [39] using the same dataset.

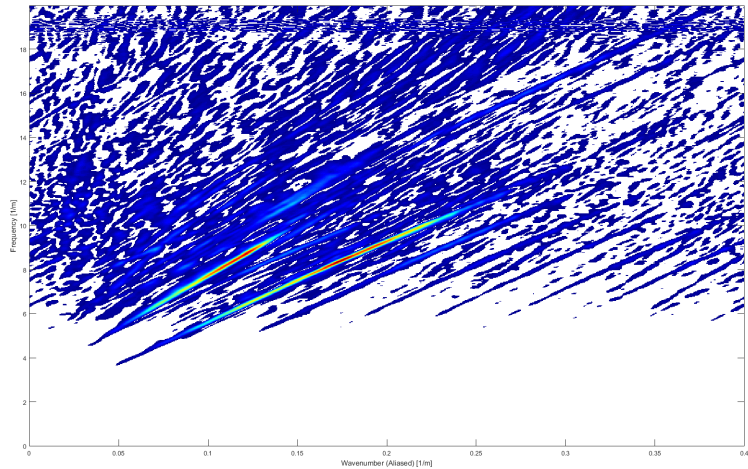


Figure 5.1: Gjøa response spectrum - In-line measurements, vertical direction - Fourier transform.

5.2 Love wave model

After having proven that the location of the modal roots has low sensitivity to damping [5], it was chosen to split the inversion for dynamic soil properties into 2 steps:

a damping independent method to find the stiffness profile, and then estimate the damping profile in a second step. Nevertheless, a correct stiffness profile is a requisite for estimating the damping profile. Therefore, a new stiffness profile has to be estimated by using the implemented Love wave model before performing a damping inversion since the previous work was not able to deal with Love waves. Moreover, it is interesting to compare the C_s profile obtained with both the models to attribute more reliability to the previous findings.

The run used the phase setting functionality implemented by [5] in the genetic algorithm. In the first phase only the fundamental mode is used and then, after 30 generations, a multimodal inversion started introducing two higher modes. The fundamental mode was given a weighting of 0.4 while both of the two higher modes have a weighting of 0.3. Re-ranging is applied every 10 generations and no layer stripping is used. The settings are shown in Table 5.1. The soil parameters and the C_s velocity ranges are shown in Table 5.2.

Table 5.1: Gjøa inversion Love wave model settings for the genetic algorithm.

N_{gen}	N_{Pop}	N_{Dad}	N_{Con}	p_{FM}
100	240	80	35	0.25

Table 5.2: Gjøa soil profile fixed parameters and C_s velocity search range for Love model inversion.

Layer	Thickness	C_p	ρ	C_s Min	C_s Max
1	1	1500	1650	20	300
2	2	1500	1700	20	300
3	4	1500	1800	20	300
4	4	1500	1800	80	400
5	4	1500	1900	80	400
6	4	1500	1900	80	400
7	4	1500	2000	80	400
8	4	1500	200	150	500
9	4	1500	2100	150	500
10	4	1500	2100	200	600
11	4	1500	2100	200	600
Halfspace	∞	1500	2100	200	700

Figure 5.2 shows an excellent convergence which is additionally accelerated by the introduction of the higher modes at generation 30. The C_s profile (Figure 5.3)

shows an overall linearly increasing trend with depth and the first three layers are estimated with a higher certainty with respect to the deeper layers. This can be attributed to the fact that the fundamental mode which feel the shallow layers is the dominant one in both the phases. Figure 5.4 shows the comparison between the theoretical modal roots (red dots) and the measured spectrum. The graph shows that the fundamental mode is matched very well and the two higher modes have a good visual shape agreement. Although the misfit error is very low, the higher modes do not line up with the ones of the response spectrum.

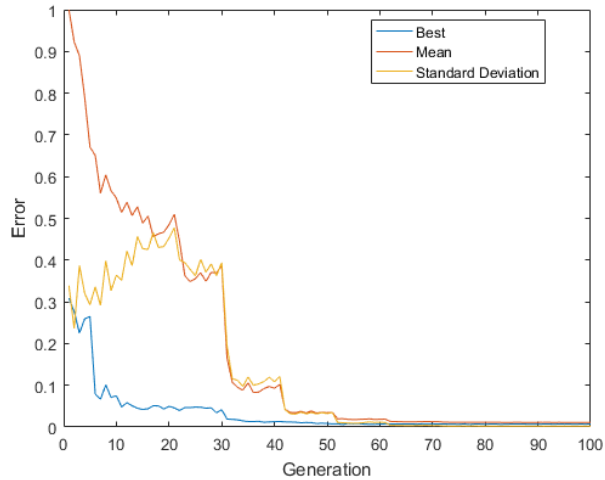


Figure 5.2: Error convergence for Love model Inversion of the Gjoa soil profile

5.2.1 Comparison of the stiffness profiles

The obtained stiffness profile is now compared to the Scholte model profile obtained by Armstrong [5]. Figure 5.5 show that there is good correspondence between the results of the two models. Both of them present an overall linearly increasing profile. The Love model estimates that the shallow layers are slightly stiffer than the ones estimated with the Scholte models and the opposite trend is instead observable for the deeper layers. The average difference between the two profiles is lower than 12%.

The predicted stiffness profiles agree well with the published results from Vanneste

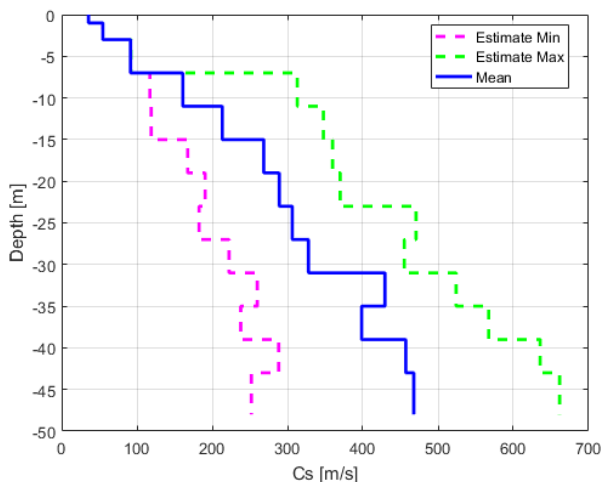


Figure 5.3: Gjøa C_s profile Love model - Range and mean of the estimated parameters based on the top 15% of the population.

[39] (Figure 5.6). Although there are several differences in the formulation of the inversion process (inversion algorithm, normalization of the determinant and stripping process [5]), the results are comparable both in terms of trend and magnitude. Moreover, the results proposed in this project show an higher degree of confidence for the shallow layers but much higher uncertainties for the deeper layers, especially for the halfspace.

5.3 Reduced profile

As mentioned in Chapter 4, the number of layers of the predicted profiles have to be reduced in order to perform the damping inversion in a reasonable amount of time. In this section, two stiffness inversions are run to estimate the new reduced stiffness profiles (both Scholte and Love waves) starting from the reference profile derived in Section 4.4 and reported in Table 5.3 along with the C_s velocity ranges for the two models. Clearly, in the 2D model for Love wave the water layer is not considered. Both the inversion are executed using the settings presented in Table 5.1 and the phase setting functionality is used. The first phase is performed considering only the

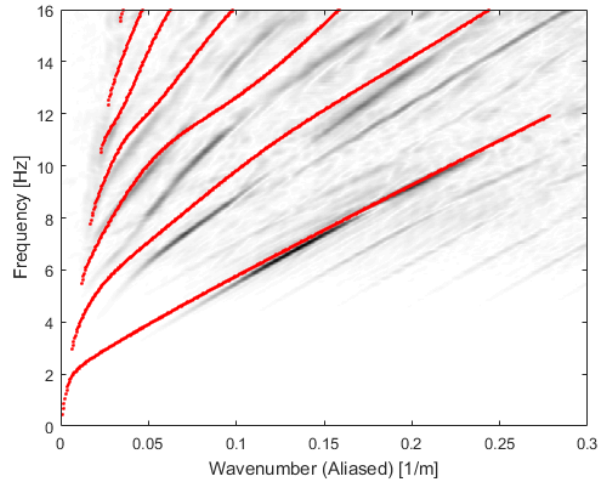


Figure 5.4: Love wave theoretical dispersion curves over the response spectrum of the cross-line measured Gjøa data.

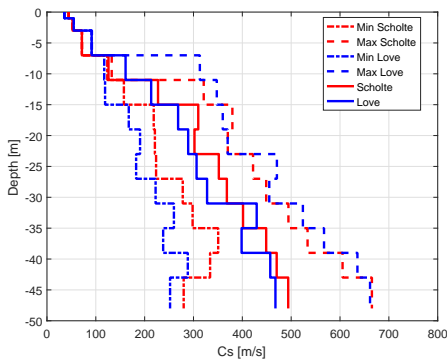


Figure 5.5: Scholte and Love stiffness profile estimate.

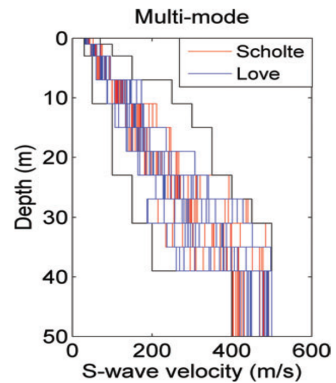


Figure 5.6: Published stiffness estimate [39].

fundamental mode while after 30 generation two higher modes are included with a weighting equal to 0.3 each.

Table 5.3: Gjøa soil profile fixed parameters and C_s velocity search range for Scholte and Love model for reduced inversion.

Layer	Thickness	C_p	ρ	Scholte		Love	
				Cs Min	Cs Max	Cs Min	Cs Max
Water	364.6	1500	1025	0	0	-	-
1	3	1500	1683	20	300	20	300
2	4	1500	1800	20	300	20	300
3	4	1500	1800	20	300	20	300
4	8	1500	1900	80	400	80	400
5	12	1500	2000	80	500	80	500
6	12	1500	2100	150	600	150	600
Halfspace	∞	1500	2100	200	700	200	700

5.3.1 Scholte waves

Figure 5.7 shows the comparison between the C_s velocity profile of the original and the new reduced layering and it also shows the dispersion curves obtained with the reduced model over the response spectrum of the Gjøa dataset. Although the very coarse resolution of the deeper layers, it is possible to observe that the reduced profile is able to capture the overall linearly increasing trend of the original one and also, in terms of magnitude, the two profiles show a good agreement especially for the first 30m. The confidence has slightly decreased for the shallow layers. Moreover, a perfect match of the fundamental mode is retrieved and the second theoretical mode is even closer to the measured one with respect to the results of the original profile. Table 5.4 show the soil profile that will be used in the damping inversion for Scholte waves.

Table 5.4: Gjøa reduced soil profile for Scholte model.

Layer	Thickness	C_p	ρ	Cs Mean
Water	364.6	1500	1025	0
1	3	1500	1683	50.5
2	4	1500	1800	74.5
3	4	1500	1800	96.5
4	8	1500	1900	268.3
5	12	1500	2000	338.5
6	12	1500	2100	347.2
Halfspace	∞	1500	2100	473.8

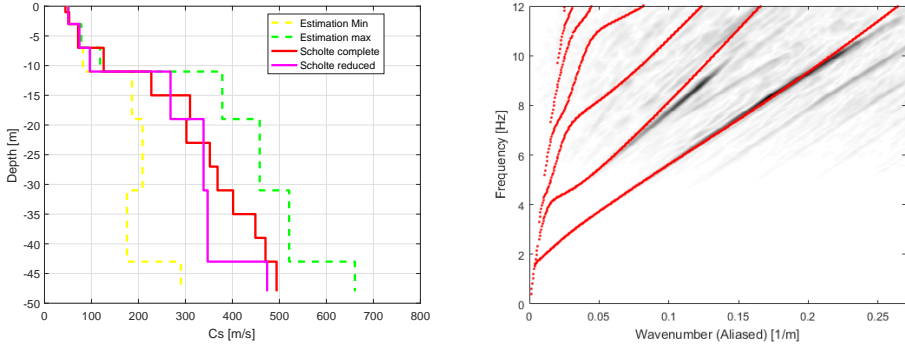


Figure 5.7: Scholte stiffness inversion results. Left panel: comparison of the shear wave velocity profiles (reduced model and original model). Right panel: reduced model dispersion curve over the response spectrum of the in-line measured data.

5.3.2 Love waves

Figure 5.8 shows the comparison between the C_s velocity profile of the original and the new reduced layering for the Love model and the dispersion curves obtained with the reduced Love model over the correspondent response spectrum. Also in this case, the new profile approximates quite well the original one in terms of overall trend. The reduced profile predicts a stiffer behaviour of the layers in the range 5-15m but the linear increasing of the deeper layers is well retrieved. Nevertheless, a decrease in the confidence of the shallow layer is noticed. Finally, it can be observed that the fundamental mode is matched extremely well while the higher modes are quite far from even a visual agreement. This has to be taken in consideration for the damping inversion. Indeed, a multimodal damping inversion is not performable with this model since, if the roots do not match, it is not possible to find the theoretical roots corresponding to the ones picked from the measured spectrum. A better result may be reached by improving the normalization technique of the determinant or combining the actual objective function with a location based one. Table 6.4 show the final reduced soil profile that will be used in the damping inversion for Love waves.

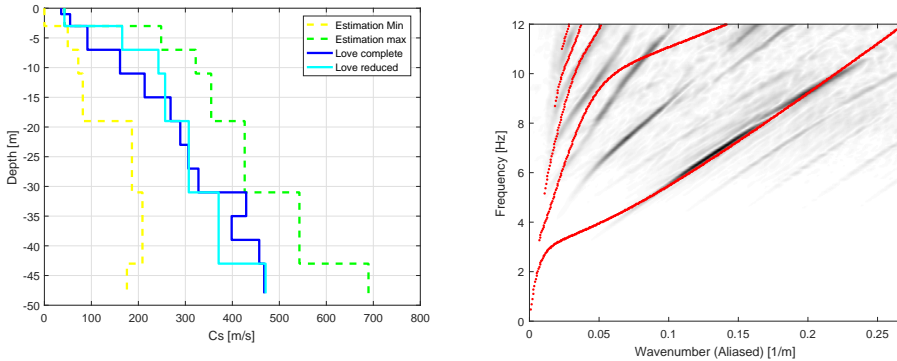


Figure 5.8: Love stiffness inversion results. Left panel: comparison of the shear wave velocity profiles (reduced model and original model). Right panel: reduced model dispersion curve over the response spectrum of the in-line measured data.

Table 5.5: Gjøa reduced soil profile for Love model.

Layer	Thickness	C_p	ρ	C_s Mean
1	3	1500	1683	42.57
2	4	1500	1800	165.56
3	4	1500	1800	242.67
4	8	1500	1900	256.90
5	12	1500	2000	307.28
6	12	1500	2100	370.79
Halfspace	∞	1500	2100	470.67

5.4 Conclusions on the stiffness inversion

In this chapter, the stiffness inversion method has been applied for estimating the C_s profile by using the new implemented Love wave model. It has shown a good agreement with the profile estimated by [5]. The comparison with the published profile retrieved by [39] has also proven the validity of the developed tool. The stiffness inversion tool has been also applied to reduce the number of layers of the Gjøa profile. Satisfying results have been achieved in terms of profile trend and roots location. Nevertheless, further improvements and investigations are still needed because the actual method is only able to perfectly line up the fundamental mode

of the dispersion domain; this misfit of the higher branches compromises the good result of the damping inversion and especially prevent the possibility to perform a multimodal analysis.

Chapter 6

Damping Inversion

This chapter focuses on the identification of the material damping properties of soil. The goal is to apply the damping inversion tool described in Chapter 3 to in-situ measured data. First, the dataset is presented and the data post-processing is described. Then, the measured attenuation curve is estimated and finally, the results of the damping inversions (both Scholte and Love waves) are presented and discussed.

6.1 Gjøa dataset: collection and processing

The Gjøa dataset is a unique and high-quality measured dataset which has been made available for this research through a collaboration with the Norwegian Geotechnical Institute (NGI). Pure shear wave data are rarely available for offshore site investigation. The measurement was carried out in the North Sea in 364 m water depth. By using shear wave propagation, the goal was to characterize the soil profile of the Gjøa reservoir which is located on the eastern flank of the Norwegian Channel. In the present experiment, a prototype shear wave vibrator has been applied (Figure 6.1). This uses a 3.25m diameter suction caisson which penetrates 2.5m into the soil and contains a linear hydraulic actuator with a 3700kg mass. The working range of frequencies is 2-60Hz which gives rise to a 10-55Hz flat power spectral density penetrating the subsurface. The receivers were placed on a 600m long array on which dragging is applied to achieve an effective receiver spacing of 2.5m. Sweeps were generated in both in-line and cross-line directions to the cable orientation in order to produce respectively Scholte and Love waves on the seabed. Specific details can be found in the paper by Vanneste [39].

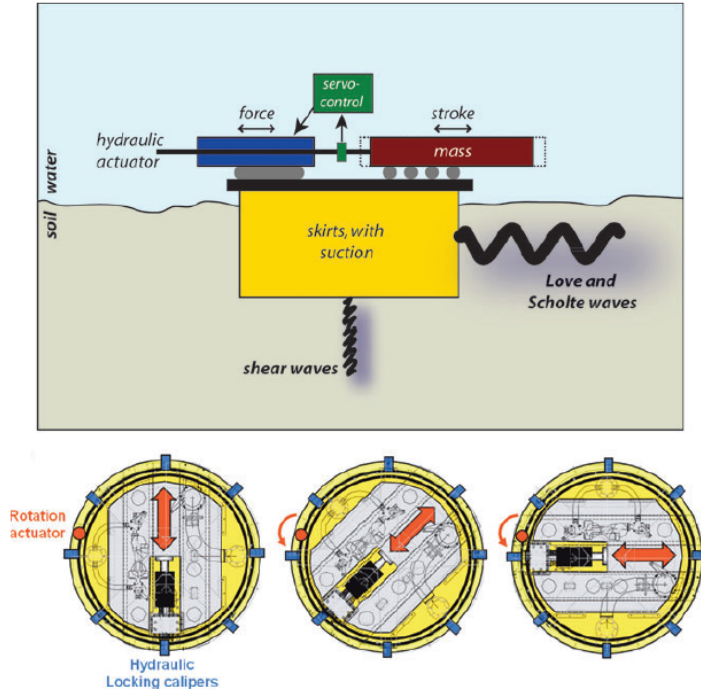


Figure 6.1: Overview of the NGIs prototype seabed vibrator. Top panel: sketch (not in scale) of the most relevant components of the vibrator. Bottom panel: sketch of the possible orientations of the actuator [39].

In order to use the presented experiment for the damping inversion, the data need to be taken in the frequency domain and processed. The results of the MASW experimental measurements are obtained in the space-time domain as shown in Figure 6.2, where each vertical trace represents the displacement (or velocity or pressure) of the respective receivers as function of time. In this response graph, it is possible to observe several types of events. In the upper part, the fast events are captured. They can be classified as body waves or pressure waves travelling in the water. When considering events with larger shapes, i.e. with lower propagation velocity, it is possible to observe the higher modes of the surface waves and the slowest event is classified as the fundamental mode. In this case, it is also possible to observe a large amount of noise in the region $x = [-50,0]$ m due to the local effects of the

source.

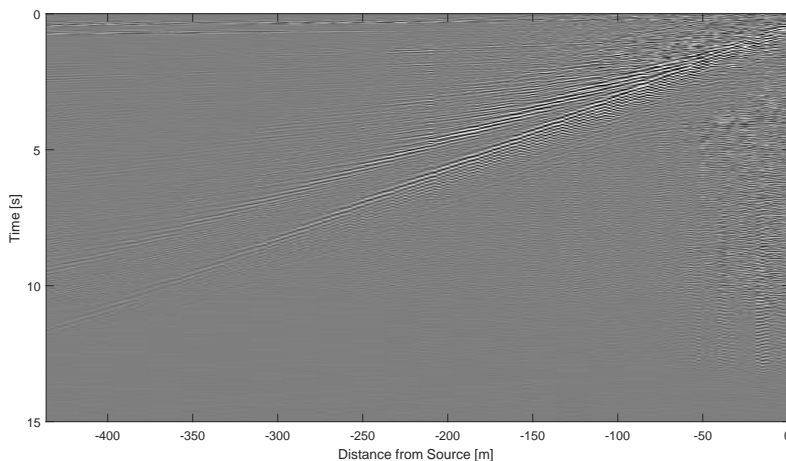


Figure 6.2: Gjøa shot record for vertical displacement of the in-line sweeps.

In order to take the data into the wavenumber domain, the Hankel transform has been chosen. This transform uses the Bessel functions which are able to automatically incorporate the geometric spreading since they are in the form of a combination between a sinusoidal function and an exponential decay. Therefore, the resulting frequency-wavenumber spectrum contains informations only about the material damping which can be retrieved from the width of the peaks of the different branches of the dispersion curves (see Section 3.4.2). The general expression of the Hankel transform is defined as:

$$\tilde{f}^{H_n}(\kappa_r, x_3, \omega) = \int_0^\infty \tilde{f}(r, x_3, \omega) r J_n(r \kappa_r) dr, \quad (6.1)$$

where r is the radial coordinate, \tilde{f} denotes the data in the space-frequency domain, J is the Bessel function and n denotes the order of the Bessel function and the Hankel transform itself. Different orders of the Bessel functions need to be used depending on the type of the source and the direction of the considered displacement. For example, for vertical sources and vertical displacement, the zero order Bessel function is applied. In the present dataset, the source is horizontal (shear vibrator), so a different order is requested. For vertical displacements, the order

of the transform should be equal to 1, while for the horizontal displacement in the cross-direction (identified in a 3D problem as u_θ) the order is equal to 2. Appendix B shows the derivations which determine the order of the Bessel function to be used for the different measurements. Once these orders are defined, the transform can be applied to the data in the space-time domain after having performed a zero padding in the wavenumber domain (reached by using a Fourier transform) in order to increase the spatial resolution. The resulting spectrum for the in-line measurements for the vertical displacement is shown in Figure 6.3.

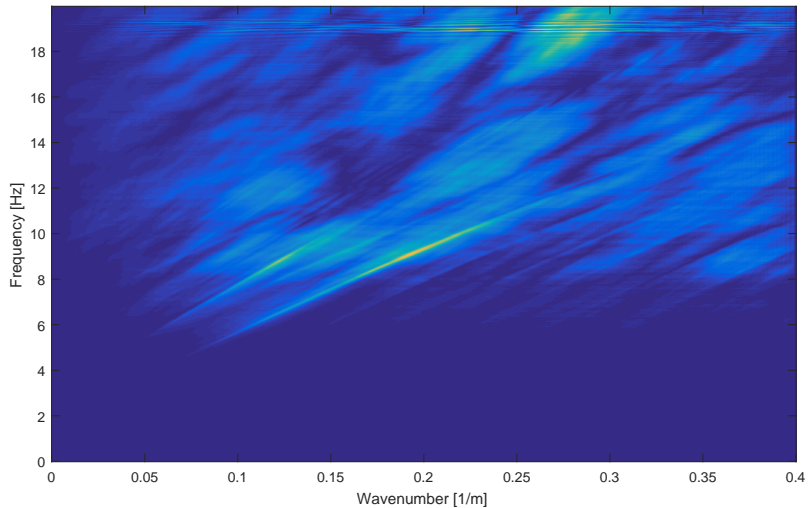


Figure 6.3: Gjøa data f-k spectrum obtained by using the Hankel transform for vertical displacement of the in-line sweeps.

Then, in order to isolate the branches of the dispersion curves which are the valuable information to stand out, the data are processed to remove the noise from the raw dataset. First of all, as said in Chapter 5, it is possible to observe a repetitive trend in the bottom right angle of the f-k response (Figure 6.3). This continues also in the region of the interest of the present research, i.e. the branches of the dispersion curves. A repetitive behaviour is generally attributed to aliasing. In this case, the spatial sampling appears to be executed in a proper way and this specific repetitive trend does not fully recall the one of the traditional aliasing. Moreover, in the space-time domain, a blocky behaviour is observable for specific offsets meaning

that the pulling of the array could have generated local irregularities such as the mismatch of the localization of the receivers due to a deviation of the cable with respect to the ideal straight line. This means that the true locations of some of the wave receivers are not correct as they were supposed to be. In addition, the data are obtained as combination of several separate source experiment, via dragging the cable. This can also create spatial inconsistencies between the signals. Therefore, a first correction is applied by reconstructing the signal smoothing the blocks found in the space-time domain. The data are transformed in the linear Radon domain and a reduction of the number of the parameters is performed. With these first operations, the repetitive pattern is highly reduced as can be observed in Figure 6.4. Also, muting is applied to better highlight the region of interest setting to zero the amplitude of very fast events (body waves) and the repetitive noise pattern.

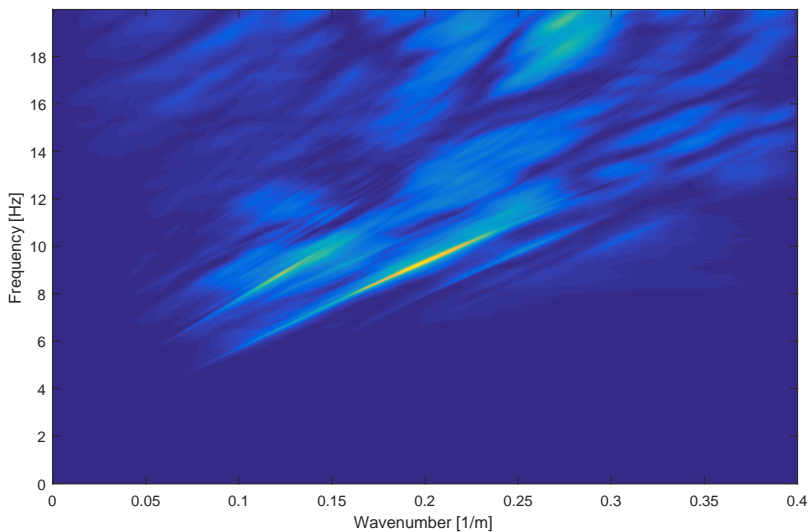


Figure 6.4: Gjøa data f-k spectrum obtained by using the Hankel transform for vertical displacement of the in-line sweeps. Muting and smoothing are applied to the spectrum.

In addition to that, it has been found that the amplitude does not decrease regularly with the distance as expected. Therefore, a rigorous inversion-type Radon transform is applied for fitting the data. The so-called “sparse Radon transform”

[37] tries to fit the original data with the least number of Radon coefficients. Two parameters need to be set in this operation. One refers to the fitting to the original data, while the other one controls the sparseness in the Radon transform domain. By increasing the latter parameter, it is possible to obtain a smoother solution in which the inconsistencies present in the collected data are reduced since they do not belong to the real data information. The best solution can be found by properly tuning the aforementioned parameters. After several tests, it has been found that the best result is retrieved for the data fitting parameter equal to 0.06 and the sparse parameter to 0.4. The result is shown in Figure 6.5. Finally, it is necessary to highlight that the damping inversions presented in the following sections of this chapter have been performed by partially using the given processing (only the reduction of the repetitive trend is used) since the corrections introduced by the latter Radon transform seem to heavily affect also the amplitude of the branches of the dispersion curves. It is difficult to directly evaluate the effects of this operation on the validity of the processed data. Further research and tests are needed to assess whether this processing is functional for the damping inversion.

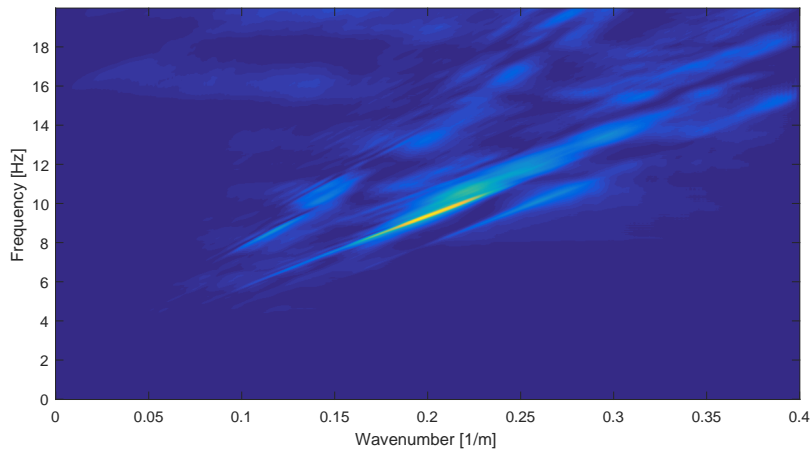


Figure 6.5: Gjøa data f-k spectrum obtained by using the Hankel transform for vertical displacement of the in-line sweeps. Data fitting parameter = 0.06. Sparse parameter = 0.4. Muting and smoothing are applied to the spectrum.

6.2 Gjøa damping inversion

In the next sections, the damping inversion tool is applied to the Gjøa dataset to retrieve the estimation of the material damping profile by using in-situ measurements. In this dataset, both in-line and cross-line measurements are present meaning that both Scholte and Love model can be used in the process. Moreover, the in-line measurements include vertical (generally used with Scholte models) and horizontal components. In principle, the results can be compared in order to reduce the uncertainties. Nevertheless, the quality of the horizontal measurements is not as high as the one of the vertical component so, in first instance, these measurements will not be used.

As mentioned in Chapter 5, the damping inversion will be applied only to the fundamental mode. Indeed, during the stiffness inversion, it has been found that only the theoretical fundamental mode lined up perfectly with the measured one while the others do not guarantee such a good agreement. This means that if they are used in a damping inversion the roots considered in the model would be artificial with limited correspondence with the roots picked from the collected data. This would introduce an error that prejudices the use of the higher modes at this point of the research without any other specific investigation.

6.2.1 Measured attenuation curve

The goal of the damping inversion is to find the best match between the measured attenuation curve and the ones computed from the different members of the population. The attenuation coefficient estimated from the measurements acts as the reference for the computation of the misfit function in each iteration of the inversion algorithm. An accurate estimation of the extracted curve is therefore needed to obtain reliable results. Once the measured attenuation curves are defined, the damping inversion follows the steps described in Section 3.5.

The fundamental measured attenuation curve is computed from the response spectrum by using the Half-power Bandwidth Method reported in Section 3.4.2. The curves are estimated by using a γ value equal to $1/\sqrt{2}$ in order to have a representative result with the actual resolution; a lower γ value gives smoother attenuation curves and signal to noise ratio is smaller. Moreover, it has been found that the overlap of the modes is not an issue in the present problem. The attenuation curve for the in-line measurements is shown in Figure 6.6. The experimental data are fitted with a third order polynomial which gives a root mean square error equal to $1.4 \times 10^{-4} 1/m$. It is noticed that the fitted curve presents an increasing trend in the

attenuation coefficient for increasing frequencies. The higher is the frequency, the higher is the material attenuation.

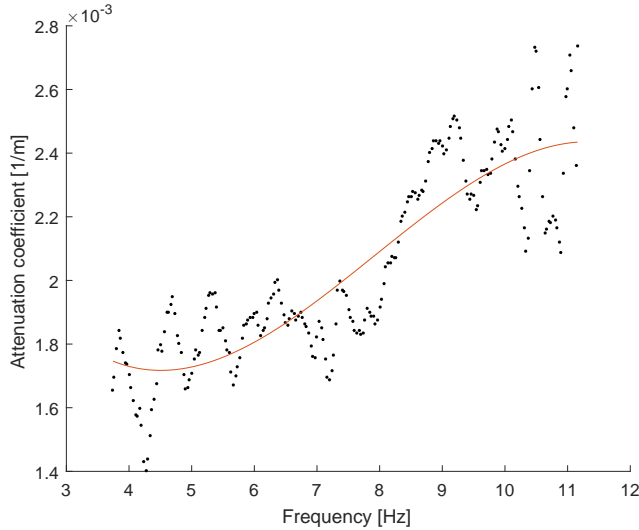


Figure 6.6: Attenuation curve estimated from in-line response Gjøa spectrum.

Figure 6.7 shows the attenuation curve for the cross-line measurements. In this case, to better capture the evident trend, the data are fitted with a fourth order polynomial having a root mean square error equal to $8.9 \times 10^{-5} \text{ 1/m}$. The increasing trend can be noticed also for the Love wave data. Moreover, it is possible to observe that the real measured data (black dots) present a gap in frequency range 8-9Hz. This is due to an amplitude discontinuity in the fundamental mode in the cross-line response spectrum. The repetitive pattern which can be observed in the region of low frequencies-high wavenumbers continues also in the region of the interest and the interference between this noisy pattern and the true results creates a prominent drop in the amplitude which gives rise to erroneous estimations of the attenuation curves that are not taken into account. Comparing this last curve with the one obtained from in-line measurements, it is possible to state that the data are reasonably fitted without altering the final result.

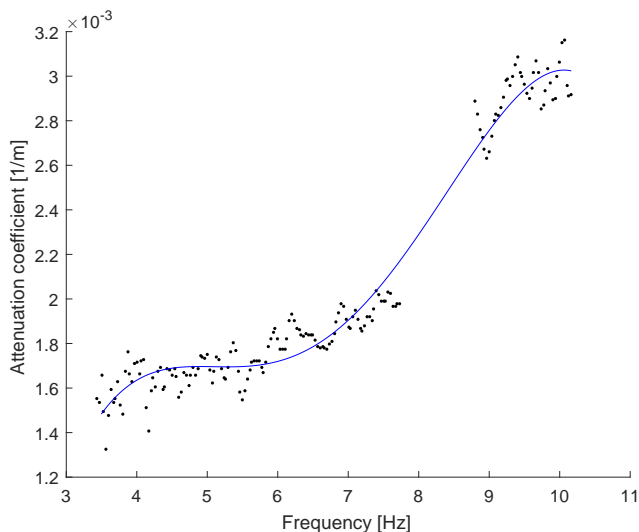


Figure 6.7: Attenuation curve estimated from cross-line response Gjøa spectrum.

6.3 Scholte waves inversion

The Scholte damping inversion is performed using the stiffness profile presented in Table 5.4. The inversion settings and the final indicative time are shown in Table 6.1. In order not to affect the results, a blind guess is chosen as a starting point. For each layer, the searching domain is defined by the range 0 – 10% material damping ratio. Unless otherwise indicated, the presented results refer to the Top 3% of the final population.

Table 6.1: Gjøa inversion Love wave model settings for the genetic algorithm.

N_{iter}	N_{memb}	Iteration estimated time
12	78125	40 mins

Figure 6.8 shows that an excellent convergence is reached already after 6 iterations. The final misfit error for the best profile is equal to 2.5%. More iterations can be performed in order to further decrease this error. Figure 6.9 shows that the damping profile has an increasing trend in the shallow layers till 20m while for the

deeper layers, it presents a constant value slightly lower than 4%. A small inversion in the behaviour is presented between layer 4 and 5. The trend of the profile perfectly agrees with the qualitative considerations reported in Section 4.6. Indeed, a combination between an increasing and a uniform profile has been predicted in the aforesaid section. The confidence interval of the shallow layers are very narrow while for the deeper layers the range is about 10%. The high level of certainty derives directly from re-ranging functionality of the searching domain. Indeed, in each iteration the new searching domain is defined by the standard deviation of the previous iteration. This means that the width of searching domain is highly reduced in each iteration. On the other hand, the top 3% includes almost 2500 members which can be considered as a representative number of samples. Table 6.2 presents the final resulted soil profile.

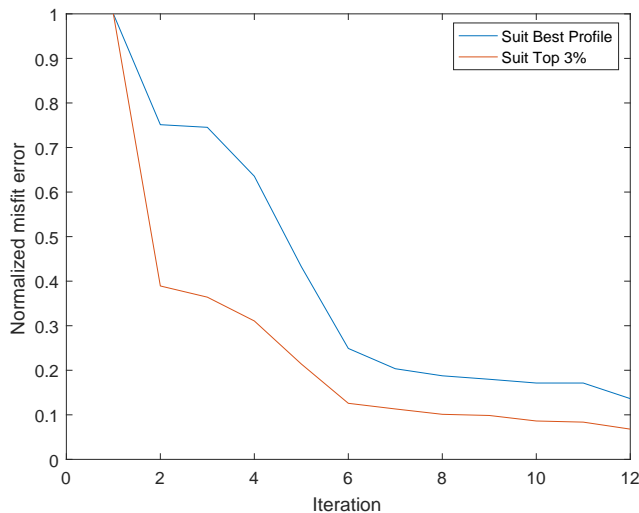


Figure 6.8: Error convergence Scholte model damping inversion Gjøa dataset.

Figure 6.10 shows the comparison between the attenuation curve obtained by the Top 3% of the final population of the inversion process and the measured one. The average error is about 2.9% while the maximum misfit is found for the lowest frequency and it is equal to 7.8%. Small differences can be observed also for in the medium range, but the overall trend is well matched. The theoretical curve oscillates around the measured one without highlighting a particular tendency. This

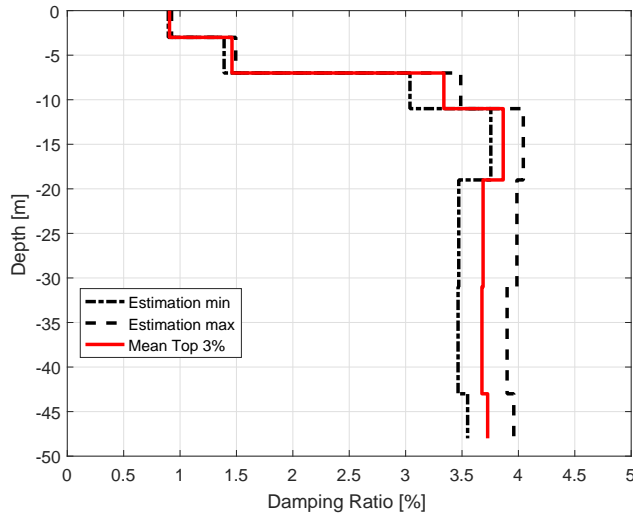


Figure 6.9: Range and mean for the Scholte waves of the Top 3% Gjøa spectrum.

Table 6.2: Gjøa reduced profile for Scholte model - Damping values for the Top 3%.

Layer	Thickness	C_p	ρ	Cs Mean	$D_p = D_s$ [%]
Water	364.6	1500	1025	0	0
1	3	1500	1683	50.52	0.91
2	4	1500	1800	74.45	1.46
3	4	1500	1800	96.49	3.34
4	8	1500	1900	268.25	3.87
5	12	1500	2000	338.50	3.69
6	12	1500	2100	347.24	3.68
Halfspace	∞	1500	2100	473.83	3.73

trend will be more investigated in Chapter 7. Moreover, it is important to mention that the measured curve is derived as an approximation of the attenuation coefficient extracted from the data spectrum, as shown in Section 6.2.1. This fitting needs to be further tested in order to evaluate its effect on the shape of the experimental curve. In conclusion, the presented results underline a good level of precision of both the damping inversion process and the reference stiffness profile derived previously. This

comparison will be used in Chapter 7 for retrieving the independence of the material damping from frequency.

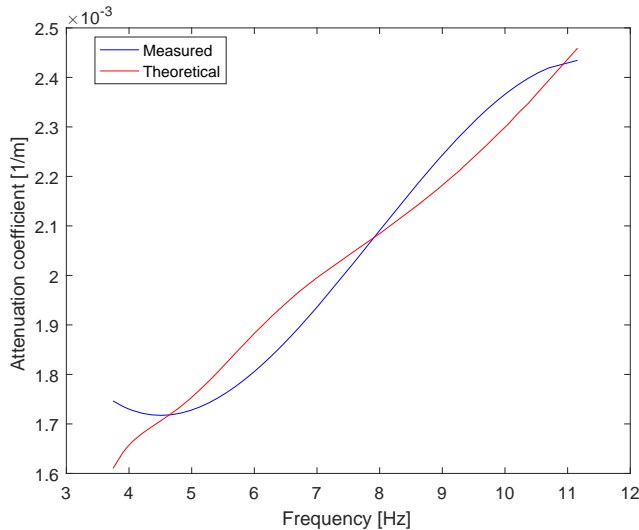


Figure 6.10: Comparison between the measured and the Scholte theoretical (Top 3%) attenuation curve.

6.4 Love waves inversion

For the Love model inversion the reference profile is presented in Table 6.4. The inversion settings are equal to the ones used in the previous inversion but the indicative time is lower (Table 6.3). Since the settings are the same and the number of roots kept is very close to the Scholte case, the cause of this reduction of time should be attributed to the computation of the coefficients of the governing matrix which is much smaller in the 2D Love waves model with respect to the Scholte model. The blind guess (0 – 10%) is newly applied.

Also for this inversion, a good convergence has been reached after few iterations (Figure 6.11). The final misfit error of the best profile is equal to 5.5%. The inversion has been stopped after 11 iterations no further improvements of the error were observed. Even if the convergence is reached, the error of the final iteration is bit

Table 6.3: Gjøa inversion Love wave model settings for the genetic algorithm.

N_{iter}	N_{memb}	Iteration estimated time
11	78125	35 mins

higher than the one obtained with the Scholte model. This could be attributed to the small misfit present in the lining up of the fundamental theoretical roots and the measured ones in the stiffness inversion. Moreover, the visual agreement of the higher modes was worse than the one for the Scholte model. This could mean that the plane model could be a poor representation of the actual reality and a perfect correspondence cannot be reached. Nevertheless, in terms of profile trend (Figure 6.12) the result is in a good agreement with the qualitative analysis of Chapter 4. Indeed, also in this case, it is possible to observe an initial increasing trend and then for depth below 20m an almost constant value for the damping is found. The confidence intervals are quite similar to the ones of the previous case.

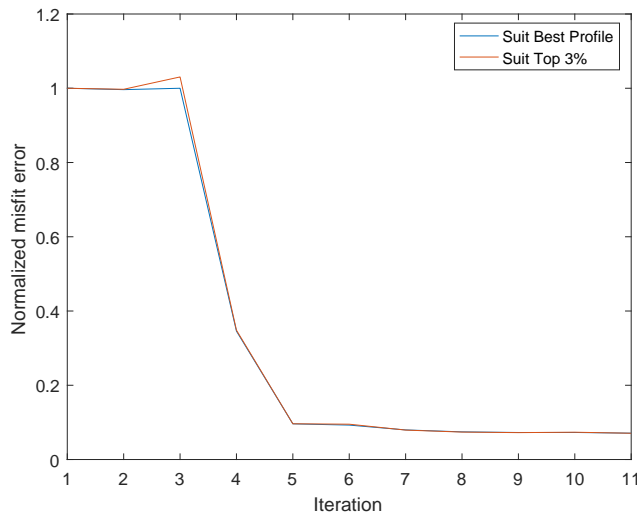
**Figure 6.11:** Error convergence Love model damping inversion Gjøa dataset.

Figure 6.13 shows the comparison between the attenuation curves. The average misfit error of the Top 3% is about 6.15% and this can be observed in the separation

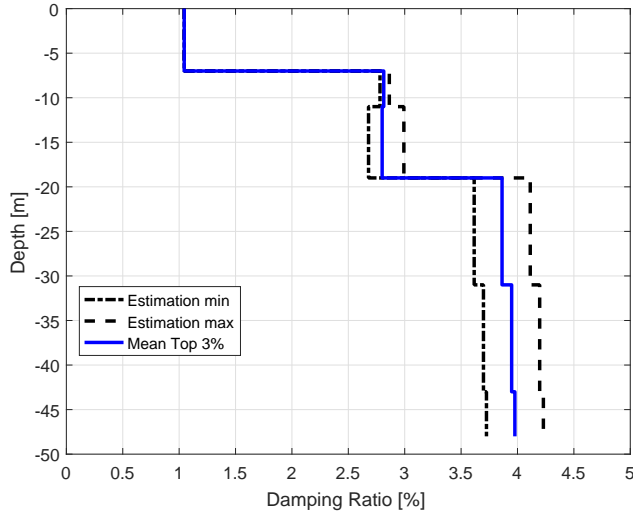


Figure 6.12: Range and mean for the Love waves of the Top 3% Gjølø spectrum.

Table 6.4: Gjølø reduced profile for Love model - Damping values for the Top 3%.

Layer	Thickness	C _p	ρ	C _s Mean	$D_p = D_s$ [%]
1	3	1500	1683	42.57	1.05
2	4	1500	1800	165.56	1.04
3	4	1500	1800	242.67	2.81
4	8	1500	1900	256.90	2.80
5	12	1500	2000	307.28	3.86
6	12	1500	2100	370.79	3.95
Halfspace	∞	1500	2100	470.67	3.98

of the curves especially high frequencies where the highest error is present and for $f=9.95\text{Hz}$ the misfit is about 14%.

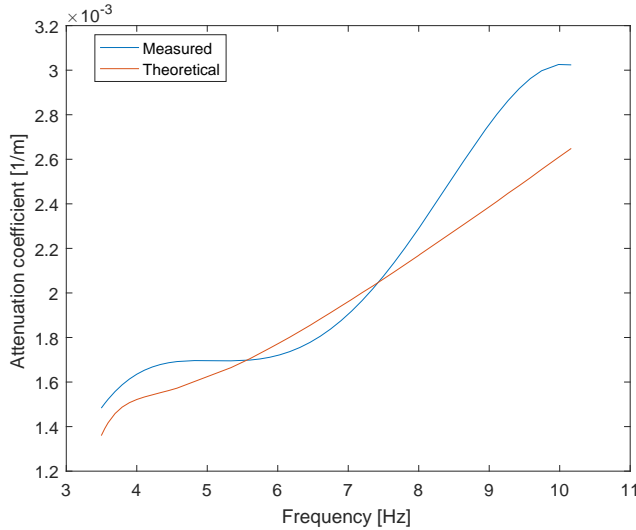


Figure 6.13: Comparison between the measured and the Love theoretical (Top 3%) attenuation curve.

6.5 Overestimation of the material damping

As reported in Section 3.4.2, the limited amount of receivers determines a truncation of the transform integral and therefore a widening of the peaks in the f - k domain. This is reflected in an overestimation of the material damping profile while performing the inversion. This error needs to be corrected in order to get more reliable results. Unfortunately, the correction proposed by [7] by using an exponential window did not give satisfying results for the present research. The windowing was not able to sufficiently increase the measured attenuation curve for the lower frequencies and therefore the “true” one presented negative values for low frequencies.

Nevertheless, the estimation of this error can be performed by using the forward model and, in the f - k domain, computing the convolution between the response signal and the transform of a boxcar function (the sinc function) which represents the limited amount of receivers. See Appendix C for the full derivation. This rectangular window simulates the limited length of the array by setting to zero the signal out of the measured window identified as $x = [0 L]$, where L is equal to 435m. This operation provokes a widening of the peaks and an amplitude scaling of the spectrum

response.

The analysis is carried out by considering the material damping profile obtained in Section 6.3. The full waveform response is computed in the f-k domain with a spatial frequency resolution equal to $\Delta\kappa = 5 \times 10^4 1/m$. The window function is calculated by using the same resolution since it has been observed that this is sufficient to properly describe the sinc function. Moreover, the domain of the window function is extended to six times with respect to the one of the surface response in order to properly incorporate the tails and the negative part of the curve. It is worth to highlight that the sinc function is centred in $\kappa = 0$. Figure 6.14 shows the effect of the mentioned window on the response spectrum of the profile proposed in Table 6.2.

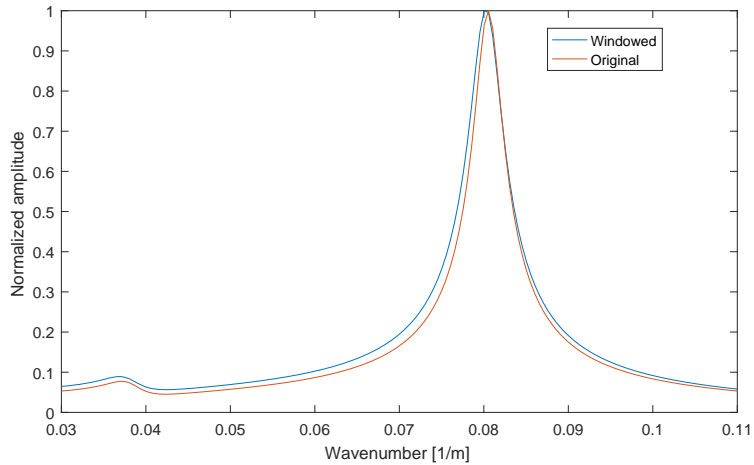


Figure 6.14: Comparison between the normalized amplitude spectrum of the original response and the windowed one. Slices obtained for $f = 4.9$ Hz.

The difference between the original attenuation curve and the one obtained with the windowed spectrum is used to compute the reduced curve which represent the true attenuation coefficient of the measured data if the truncation would have not been applied. In this analysis, a linear effect of the truncation is assumed meaning that it is possible to retrieve the “non truncated” attenuation curve (called here “reduced”) by evaluating the effect of the window on the overestimated profile. Figure 6.15 shows the comparison between the attenuation curve obtained with the forward model, the one obtained with the windowed response and the one obtained

by subtracting the effect of the windowing to the original attenuation curve. The reduced attenuation curve is then used as a reference for a new damping inversion performed using the Scholte wave model. Figure 6.17 shows the percentage effect of the windowing with respect to frequency. A percentage higher reduction can be observed for lower frequencies. The results of the inversion are presented in Figure 6.16.

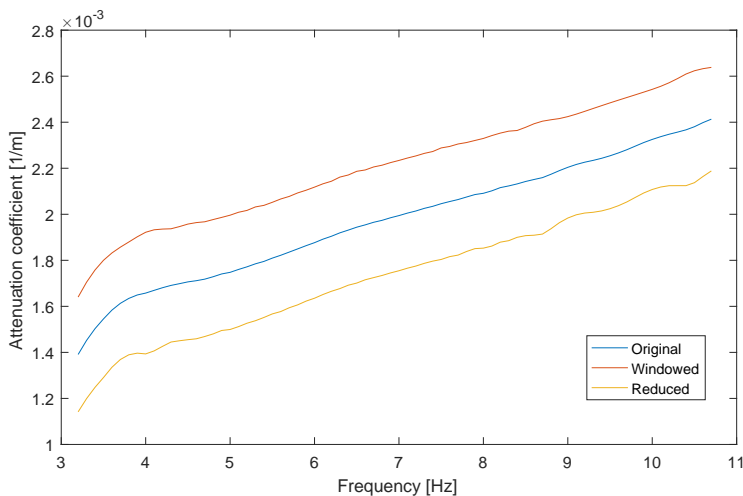


Figure 6.15: Comparison between the attenuation curves.

Also in this case, the predicted trend of the profile is well retrieved. The confidence intervals are wider with respect to the previous cases because the inversion has been stopped after 3 iterations since the misfit error of the best profile was lower than 2.5%. Figure 6.18 shows the comparison between the profile obtained in Section 6.3 and the one estimated in this section. As expected, the new estimate is lower for the entire considered depth. Figure 6.19 presents the percentage layer reduction of the new estimate with respect to the original one. The mean reduction is about 23% and it is possible to observe that the highest reduction is found for the deeper layers - the reduction is in the range 26 – 32%. This is in agreement with Figure 6.17 since lower frequencies are more sensitive to the deeper layers.

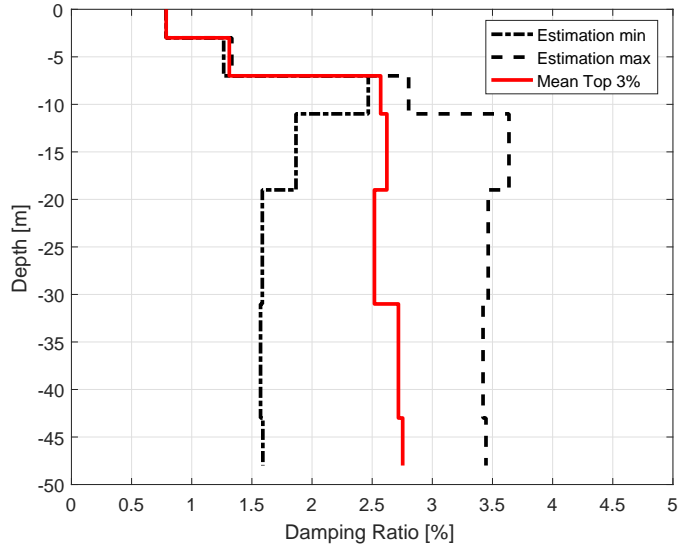


Figure 6.16: Range and mean for the Scholte waves of the Top 3% Gjøa spectrum for the reduced attenuation curve.

6.6 Conclusions on the damping inversion

In this chapter, the damping inversion method has been applied to measured data collected in the marine setting. Both the models (Scholte and Love waves, Figure 6.20) indicate a material damping profile which increases in the first 20m and is constant for the rest of the visible depth. The magnitude of the two profiles is comparable and Love model predicts a higher attenuation for the shallowest layer and in the range 20-50m while in the range 7-19m the Scholte model presents a higher damping value. Nevertheless, the trend is quite atypical since an increasing profile is traditionally retrieved - even if this would have been in contrast with the findings in Section 4.6 - because it is generally assumed that less consolidated layers should have higher damping ratio values rather than the deeper ones. Further investigations are needed to assess if there are specific site conditions which determine this trend or if the general accepted assumption cannot be extended to all the scenarios. Moreover, the results show a high level of confidence, especially for the shallow layers. This could be in part determined by the re-ranging function of the present method.

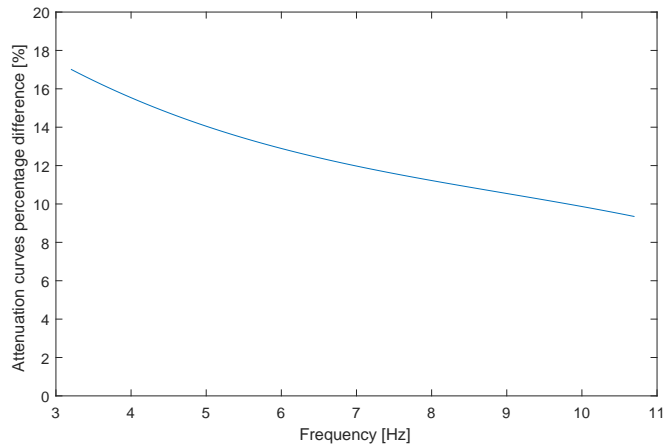


Figure 6.17: Percentage difference of the original and the reduced attenuation curve with respect to frequency.

Moreover, the overestimation analysis has shown that limited amount of receiver highly affects the estimation of the soil material damping profile. Indeed, it has been found that the estimate computed considering the truncation of the transform integral is in average about 30% higher with respect to the one obtained removing the rectangular window by using the theoretical model. The overestimation is higher for the deeper layers.

About the technical aspects, the damping inversion tool has proven a high level of reliability in terms of functionality and computational time. The Love model results in a lower execution time due to the dimension of the coefficient matrix. The generation of the population turned out to be the most expensive process since the input files have to be filled together with the batch running file.

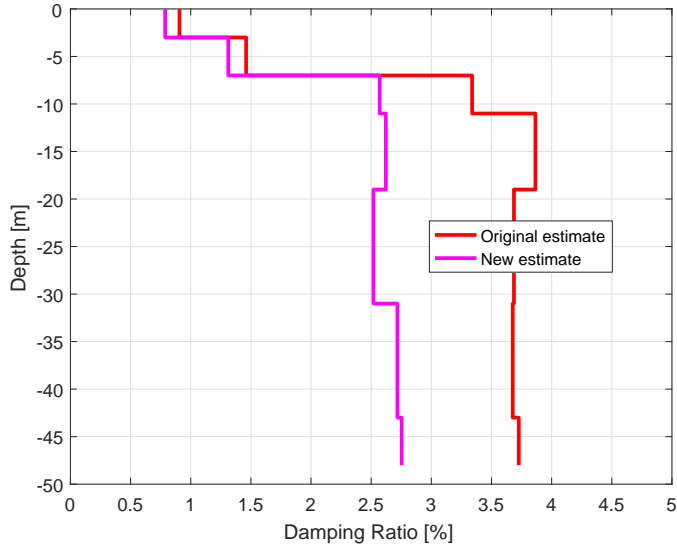


Figure 6.18: Comparison between the original damping profile and the one obtained considering the overestimation for Scholte model.

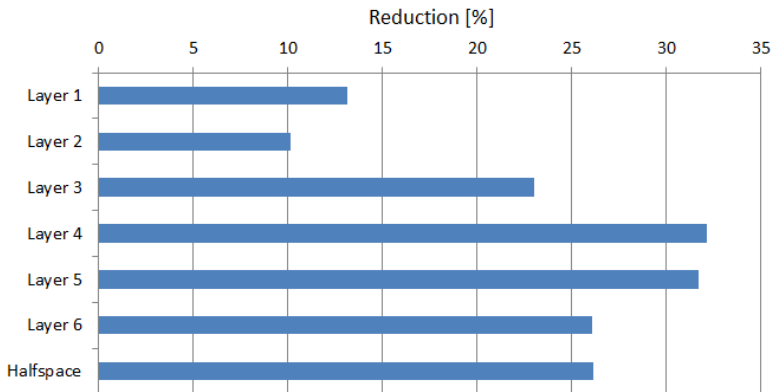


Figure 6.19: Soil damping material ratio percentage reduction per layer for Scholte model due to the computed overestimation.

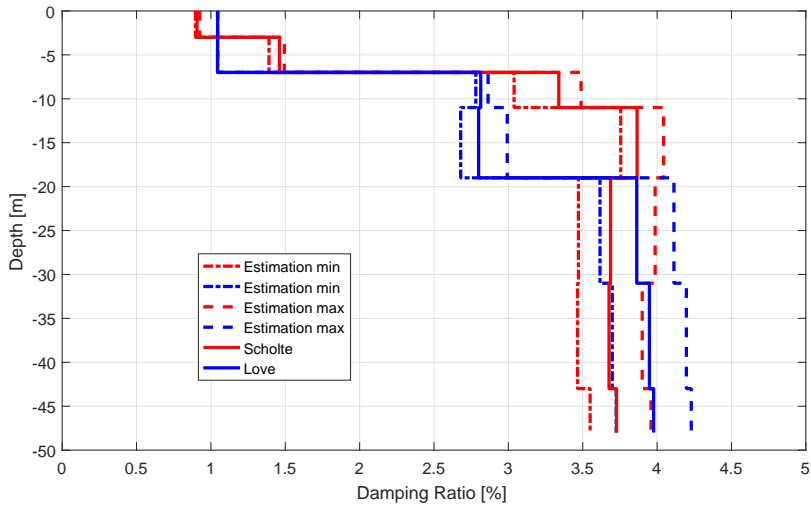


Figure 6.20: Ranges and means of the Gjøa damping profiles obtained with Scholte and Love wave models. The results refer to the Top 3% of the population.

Chapter 7

Frequency Dependence of Damping

This chapter focuses on the analysis of the relation material damping versus frequency by using surface wave measured data. A novel technique is proposed for retrieving this relation starting from the results of the damping inversion. Then, two new alternative approaches are reported and advantages and limitations are discussed.

7.1 Background

Limited literature is present for material soil damping at low frequencies. Retrieving information about the dependency of damping at very low frequency is very hard especially by using in-situ measurements like active MASW. The complexity lays in the generation of propagating waves at that low frequency, to such an extent that a combined method using active and passive source is recommended for filling the dispersion trend at lower frequencies [34]. Some material damping model as function of frequency are presented in literature. Liu et al. [28] used a continuous superposition of relaxation peaks to find out that Q^{-1} shows a constant trend in frequency range $10^{-4} - 10^2$ Hz within 1% error while out of this region two steep descendent paths are observed. The constant behaviour is also retrieved by Lai et al. [25] by using in-situ cross-hole seismic testing. Moreover, also [4] has mentioned that the soil material damping behaved as frequency independent for $0.1 < f < 10$ Hz which is also called hysteretic or rate-independent damping. Traditionally,

the resonant column (RC) device is also used to evaluate the dynamic properties of soils at low strains. Nevertheless, frequency dependent dynamic properties are difficult to get using RC as they would require significant changes in the geometry of the specimen. Non-resonance (NR) methods have been proposed to overcome this limitation [19]. In this study, it has been found that for sand-bentonite specimens the material damping ratio is frequency independent in the range 0.25-4Hz. This chapter aims to determine the frequency dependency of the material damping for the Gjøa measured data collected in the marine setting.

7.2 Novel technique

In this section, a novel technique for retrieving the independence of the material damping ratio from the frequency is presented. The method uses the results of the damping inversion on in-situ measurements to verify the hypothesis that, at least in certain ranges of frequency, the soil material damping has a hysteretic behaviour. It is important to remember here that the results presented in Chapter 6 are obtained by including in the theoretical surface wave model a frequency independent damping model as reported in 2. The idea behind the proposed method is that a frequency dependency results in direct a modification of the shape of the attenuation curve which varies with frequency. Indeed, the key process of the method lays on the idea of scaling the theoretical attenuation curve with a frequency dependent scaling factor which acts as a correction for the misfit error between the curves. The result indicator is identified as the frequency dependency relation of the material damping ratio.

The method is tested by using the results obtained from the Scholte damping inversion presented in Section 6.3. In fact, it has been shown that the quality of the findings using the in-line data is very high and then it is possible to uphold that the results of this analysis are not highly affected by the possible errors committed in the previous steps. Although subsequent, it is possible to assume that the damping inversion and the present analysis are uncoupled. Figure 7.1 shows again the comparison between the attenuation curve obtained by the Top 3% of the final population of the inversion process and the measured one for the Scholte wave model. As mentioned before, small differences can be observed in the curve especially at the lower frequencies. The method prescribes the computation of the correction factor as the ratio between the theoretical attenuation curve and the measured one. Figure 7.2 shows the tendency of the scaling factor versus frequency.

From the graph, it is visible that the scaling factor is independent from frequency.

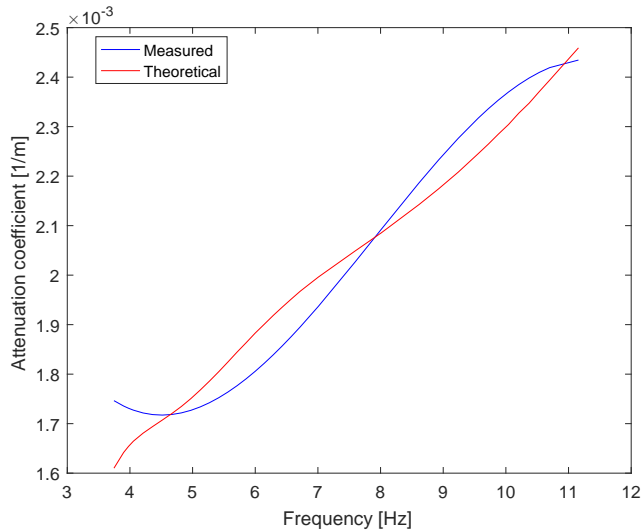


Figure 7.1: Comparison between the measured and the Scholte theoretical (Top 3%) attenuation curve.

As said, the relation between correction and frequency can be directly associated to the relation between the material damping ratio and the frequency. Therefore, it is possible to conclude that, in the frequency range of the present measurements, the material damping is frequency independent. Recalling the model proposed by [28], it can be said that the actual data highlight only the region associated to the constant part of the relation. At this stage of the research, it is not necessary to extrapolate this relation till very low frequencies with the available data, although in literature, it has been found that this modelling can be extrapolated till 0.25-0.5Hz [20].

Then, since some negligible oscillations can be noticed, as a check, the correction factor is introduced into the forward model acting as the frequency dependent relation of the material damping. For each layer, the damping value obtained in the damping inversion is kept constant and the derived relation is used as a scaling which gives a different correction at every frequency. Figure 7.2 shows the attenuation curve computed by introducing the scaling factor into the forward model of the result of the Top 3% and the measured one. As expected, the two curves match perfectly.

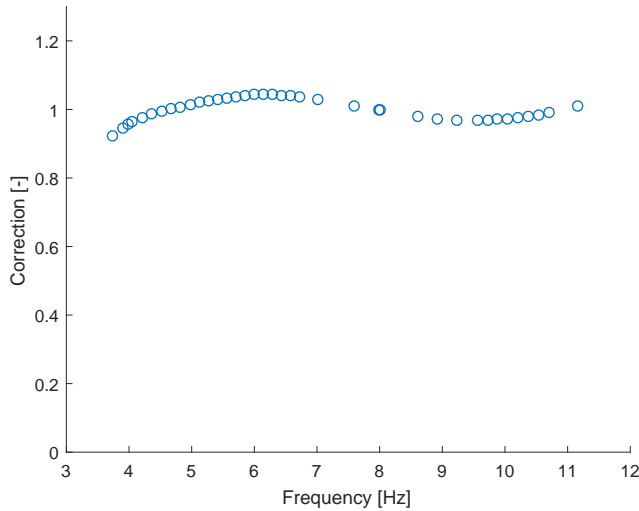


Figure 7.2: Correction factor obtained as the ratio between the theoretical and the measured attenuation curve.

The possible limitation of this approach resides into two aspects. First, the derived relation is unique for every layer. This means that the correction factor cannot take into consideration the material properties of each layer since the correction is computed as a modal relation and not directly depending on the material type. Second, the present analysis can only be performed a posteriori, meaning that its success depends on the good quality of the outcome of the damping inversion.

7.3 Two alternative techniques

Consider the potential limitations of the previous method which will be called "Scaling Factor Method", in this section, two new methods are presented. Both the techniques are based on the damping model introduced by Liu et al. [28]. In these approaches, a known relation damping ratio-frequency is hypothesized and the analysis aims to find the parameters that describe the aforesaid relation. For the proposed methods, the relation between the damping material and the frequency is approximated to a bilinear (first linear and then constant) model as shown as shown in

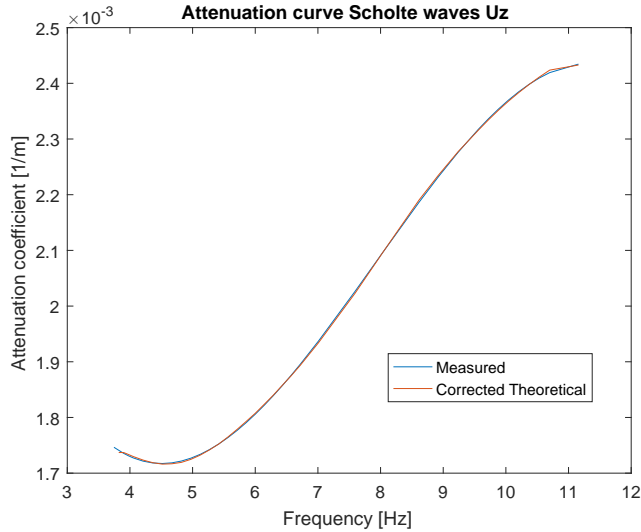


Figure 7.3: Comparison between the measured and the Scholte theoretical (Top 3%) attenuation curve corrected with the Scaling Factor Method.

Figure 7.4 which can be fully described by two parameters: the slope of the linear part ϕ and the value of the constant part D . In this two methods, the frequency dependency is estimated for each layer.

7.3.1 One parameter approach

In this first method, only the slope of the linear part ϕ is unknown. The value of the constant part is given by the material damping ratio estimated in the inversion process. The guessed damping model is introduced in the forward model and a new inversion is performed in order to find an estimation of the unknown value for each layer. The analysis has been carried out starting from the results of the Scholte wave inversion (see Section 6.3). The outcome of this first alternative approach is shown in Figure 7.5. It is clearly observable that, in the range of frequency that is available from the measurements, there is no frequency dependency for the material model.

In this method, the advantage is that only one parameter per layer has to be identified. Keeping the same amount of steps of the searching domain, the number of members of the population remains the same since also in the original inversion

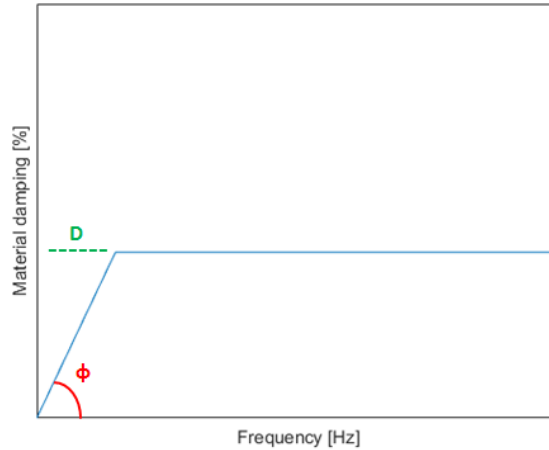


Figure 7.4: Identification of the two parameters in the simplified bilinear relation.

there was only one parameter per layer to be found. The drawback is that indeed an other inversion process has to be carried out. This takes a lot of time and the benefits that this method brings seem not to equalize the computational effort.

7.3.2 Two parameters approach

This second method gives the possibility of performing a joint analysis combining the damping inversion (which finds the reference damping profile) and the approach for retrieving the possible frequency dependency of damping. Indeed, the unknown parameters are now the slope of the linear branch ϕ and the value of the constant part D . The proposed damping model is again introduced in the forward model and the inversion is performed. The total number of unknown parameters is the number of layers times 2. Also, this method can be extended to other known relations such as polynomials increasing the number of parameters. Clearly, the advantage of this method is that a unique process is needed to get the solution in a direct way. But, unfortunately, this technique has not been tested because it has been resulted computationally very expensive for the available resources: the dimension of the population blows up because 2 parameters have to be estimated per layer. Three possible solutions are proposed. First, reducing the number of layers to decrease the total number of unknown variables. Nevertheless, this solution seems quite extreme

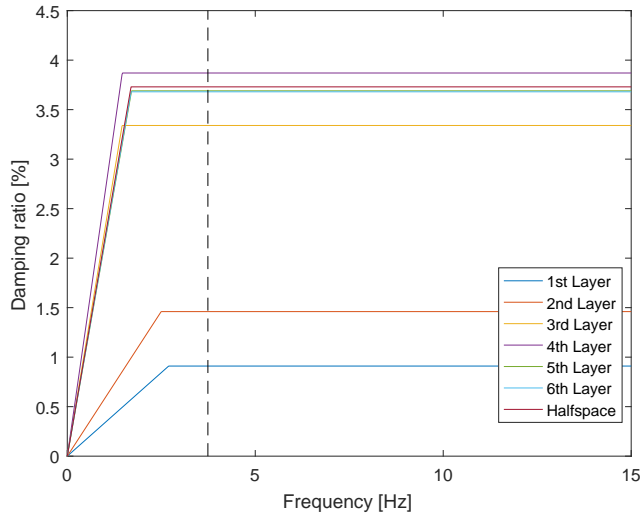


Figure 7.5: Results of the One Parameter Approach - Material damping modelling of each layer.

since the thickness of the layers (especially the deeper ones) is already quite high. Second, reducing the depth of investigation keeping the same layering. Third, implementing a new inversion algorithm which can better handle this huge amount of combinations.

7.4 Conclusions on frequency dependence of damping

In this section, three novel methods have been proposed to retrieve the possible frequency dependency of the material damping ratio. Two of them have been used with the results of the Scholte wave damping inversion and they have shown that, in the considered range of frequency, there is no dependency. Further investigations are needed to assess whether this modelling can be extrapolated to very low frequencies. The Scaling Factor Method is the most computationally cost-effective among the proposed methods. Indeed, a modal frequency dependent relation can be derived by a simple analysis performed after the damping inversion process. On the other

hand, the two parameters approach seems to be very promising if the computational issues can be overcome. In fact, it allows to perform a unique inversion process and retrieve possible informations about the trend of the damping material ratio at very low frequency thanks to the approximated bilinear relation.

In conclusion, it is necessary to highlight that the results obtained in this chapter are valid for the available amount of data and range of frequencies considered. In order to certainly assess whether the soil material damping ratio depends on frequency, the higher modes need to be included in the analysis. This would lead to a multimodal damping inversion which can be performed per frequency. Although in this experiment it has been found that the material damping is frequency independent, it is not possible to generalize this result for different frequency contents, settings, soil types and profiles.

Chapter 8

Conclusions and Recommendations

A new theoretical wave model was implemented to perform a damping inversion from measured data. A modal damping inversion method is introduced with a novel inversion algorithm and some functionalities are added to reduce the computational time. Firstly, sensitivity and qualitative studies are performed in order to get a better understanding of the proposed method and predict the experimental results. Secondly, the method is used to retrieve the material damping profile from a high-quality dataset collected in a marine setting. Finally, the frequency dependence of damping in the available frequency range is verified. In this chapter, the conclusions and the recommendations for further research are presented and discussed.

8.1 Conclusions

Stiffness inversion

- The Love wave model has been used with the previously developed stiffness inversion method. The results have confirmed the reliability of the tool and the obtained shear wave velocity profile is in agreement with the Scholte profile reported by [5] and shows a perfect line up of the roots of the fundamental mode for both the considered models.
- The resulting stiffness profiles have shown an excellent agreement with the published results both in terms of trend and magnitude. The uncertainties of

the shallowest layers for the obtained profiles are lower than the ones proposed by [39].

- Excellent results have been found by reducing the number of layers of the soil profile. The new profiles show a good agreement with the original ones in terms of trend and present excellent location of the fundamental roots.

Damping inversion

- The damping inversion method has shown a high degree of reliability for both synthetic and experimental applications. The optimization method is able to highly reduce the number of the iterations re-ranging the searching domain in every iteration. The misfit errors of the best profiles are in all cases equal of lower than 5%.
- Different solutions have been found for reducing the computational time: wavelet compression, modified search algorithm, layering reduction and executable programming. All of them have shown excellent results during the performances and allowed to run much more simulations and iterations reducing the errors.
- The proposed objective function, which is defined as a normalized difference per frequency of the measured and the theoretical attenuation curves, has proven to be robust and handy to implement and use in the different applications. In most of the cases, the attenuation curve has resulted to be a smooth function which can be characterized by a small amount of points. Combined with the wavelet compression, this property is able to speed up the computation.
- The results of the damping inversion have shown a good agreement with the a priori qualitative analysis performed. Moreover, the two obtained profiles (Scholte and Love models) are comparable in terms of magnitude and trend (linearly increasing till 20m and then almost constant). The measured and the theoretical attenuation curves show a good match for both the cases and an overall error less than 7%.
- The analysis of the overestimation of damping has shown that a limited amount of receivers highly affects the estimation of the soil material damping profile. A technique is proposed to remove this overestimation by computing the full waveform response using the theoretical wave model introducing a boxcar function which simulates the experimental measurement window.

- The proposed novel technique has been able to determine the dependency of damping from frequency in considered range. It turned out that the material damping ratio is independent from the frequency content of the present analysis. The extrapolation till very low frequencies can be performed following the literature findings [19].

8.2 Recommendations

Stiffness inversion

- The stiffness inversion has shown that only the roots of the fundamental branch of the dispersion curve line up very well. It has also been found that this can have an implication on the damping inversion. The actual stiffness inversion method should be investigated more to find the cause of this misfit. It can be suggested to combine the suitability function proposed by [13] with the used one or verify the possible existence of other modes which are not highlighted by the available spectra.
- In order to reduce the computational time, a combination of the used genetic algorithm and a local one, once the solution is close to the global minimum, is recommended

Damping inversion

- A multimodal analysis is the next step of the proposed damping inversion method. Nevertheless, it can only be relied on if the stiffness inversion method improves the alignment of the roots.
- A better understanding of the halfspace sensitivity is recommended in order to reduce the uncertainties linked to it and its effective existence. Indeed, it is worthy to question whether the halfspace is a reliable model approximation (at a certain depth) and how this affects the final results. Different layering or a fixed bottom model could be implemented and tested with the actual measured data. Also, other investigation techniques (such as CPT) would be helpful in defining the layering.
- A modified random search method is applied as inversion algorithm. Other global minimization method can be tested such as a modified genetic algorithm (the one proposed by [5] was too random for this application), a gradient based algorithm or a flock based algorithm. It could be possible that a

combination of these methods leads to the best results in terms of accuracy and time.

- A systematic setting analysis of the method is recommended. Indeed, the inversion process includes a large number of actions in which many parameters play a fundamental role. Some key parameters are: the precision of the complex root finding tool, the amount of roots considered, the fitting of the measured attenuation curve, the number of members of the population and the re-ranging factor.
- It would be good to check the damping estimate via an independent measurement technique such as CPT, SCPT, borehole method or laboratory tests in order to verify the agreement in terms of trend and magnitude of the result soil damping profile. No alternative measurements are so far available for the present site.
- The re-ranging functionality of the proposed damping inversion tool has shown an excellent behaviour narrowing the searching domain down every iteration, highly reducing the computational time. Nevertheless, the implications of this function should be investigated in order to understand if it affects the quality of the results or it is only beneficial and if the actual confidence intervals can be considered as fully reliable.
- An extensive characterization of the uncertainties is recommended in order to assess the reliability and the errors associated to the presented estimate. Moreover, it can be used to attribute a proper weight to the different modes of the multimodal inversion.
- Alternative studies on the overestimation of damping need to be performed in order to assess the reliability of the obtained results. It is possible to work directly on the measured data to correct them for the widening of the peaks introduced by the truncation of the integral, as shown by [7]. This study could give fundamental indications for further experiments in terms of measurement setting, such as the length of the receiver array.
- The effects of the Hankel transform on the measured data need to be systematically characterized. It has been found that the the order of the Bessel function does not affect the amount of the material damping (i.e. the width of the peaks) in the f-k domain response. This should be tested by using different datasets or synthetic data.

- The results of the proposed Scaling Factor Method seem very promising in terms of quality and effort. Nevertheless, more cases have to be tested to assess the validity of the method.
- The results obtained for the frequency dependence of damping are valid for the available amount of data and range of frequencies considered. Although in this experiment it has been found that the material damping is frequency independent, it is not possible to generalize this result for different frequency contents, settings, soil types and profiles. In order to assess whether the soil material damping ratio depends on frequency, the higher modes need to be included in the analysis and a damping inversion per frequency needs to be performed.
- The “two parameter technique” for analysing the frequency dependency of damping seems very promising. Nevertheless, it was not possible to test it with the measured data due to computational requirements. Possibly, an optimization of the actual algorithm would make this computation possible with the present resources. Moreover, a different dependency relation could be implemented, as shown by [27].

Appendix A

Hysteretic Behaviour of a Visco-Elastic Material

This Appendix describes the hysteretic behaviour of a visco-elastic material. First, it is needed to get rid of the frequency dependence. Then, the amount of energy dissipated per cycle is defined and, finally, the material damping ratio is determined. The derivations are inspired by [18] and [7].

First of all, it is needed to recall the equations reported in Chapter 2. The harmonic shear stress and the complex shear stiffness can be expressed in the following forms:

$$\begin{aligned}\tau &= \tau_0 \sin(\omega t) \\ \gamma &= \gamma_0 e^{i(\omega t - \phi)}\end{aligned}\tag{A.1}$$

This two equations can be combined in order to eliminate the term ωt as shown by [18]:

$$\left(\frac{\tau}{\tau_0}\right)^2 - 2\cos\phi\left(\frac{\gamma}{\gamma_0}\right)\left(\frac{\tau}{\tau_0}\right) + \left(\frac{\gamma}{\gamma_0}\right)^2 - \sin^2\phi = 0\tag{A.2}$$

The solution to Equation A.2 can be expressed as:

$$\tau = \mu\gamma \pm \mu'\sqrt{\gamma_0^2 - \gamma^2} = \tau_1 + \tau_2\tag{A.3}$$

The term τ_1 represents a linear dependence between the strains and the stresses while, the term τ_2 can be expressed by using an elliptical form. The combination of these two stresses leads to a rotated ellipse in the plane $\gamma - \tau$, whose rotation depends on the stiffness μ of the material. The area enclosed by the ellipse, which is called hysteretic loop, is related to the amount of energy per unit volume which is dissipated in each cycle of the harmonic loading. The dissipated energy ΔW in a cycle of period T is expressed as following [18]:

$$\Delta W = \int_0^T \tau d\gamma = \mu' \pi \gamma_0^2 \quad (\text{A.4})$$

While, the maximum strain energy per unit volume stored per cycle is given by [18]:

$$W = \frac{1}{2} \mu \gamma_0^2 \quad (\text{A.5})$$

As defined by Borchardt (1973), the Q factor is “the ratio of the peak energy density stored per cycle of forced oscillation to the loss in energy density during the cycle” and combining this definition with Equations A.4 and A.5:

$$Q = 2\pi \frac{W}{\Delta W} = \frac{2\pi \mu \gamma_0^2}{2\mu' \pi \gamma_0^2} = \frac{\mu}{\mu'} \quad (\text{A.6})$$

Moreover, the Q factor can be related to the material damping ratio by the following expression [30]:

$$Q = \frac{1}{2D} \quad (\text{A.7})$$

Finally, by introducing the relation between the shear material damping and the shear damping ratio $D_s = \eta_s/2$, it can be found that:

$$D_s = \frac{\eta_s}{2} = \frac{1}{2Q} = \frac{\mu'}{2\mu} \quad (\text{A.8})$$

Appendix B

Bessel Functions and Hankel Transform

This Appendix shows the derivations and the considerations needed to determine the order of the Bessel function which has to be applied in the Hankel transform depending on the direction of action of the source with respect to direction of the considered displacement. This section is inspired by [40] and [1].

In the present work, the measured data used were generated by using a shear vibrator, i.e. an horizontal polarized source. This means that only one type of source is present and the different orders of the Bessel functions are determined in relation to the directions of the displacements. The full 3D formulation of the problem for a horizontal source presented in Chapter 2 is recalled here. The solution to the problem is obtained by using the Helmholtz decomposition to express the displacements in terms of potentials. The displacements for the j -th layer are expressed in the following form [40]:

$$\begin{aligned}\tilde{u}_{r,j} &= \frac{\partial \tilde{\phi}_j}{\partial r} + \frac{1}{r} \tilde{\psi}_{z,j} - \frac{1}{2} \frac{\partial(\tilde{\psi}_{r\theta,j}^+ - \tilde{\psi}_{r\theta,j}^-)}{\partial z} \\ \tilde{u}_{\theta,j} &= -\frac{1}{r} \tilde{\phi}_j + \frac{1}{2} \frac{\partial(\tilde{\psi}_{r\theta,j}^+ + \tilde{\psi}_{r\theta,j}^-)}{\partial z} - \frac{\partial \tilde{\psi}_{z,j}}{\partial r} \\ \tilde{u}_{z,j} &= \frac{\partial \tilde{\phi}_j}{\partial z} - \frac{1}{r} \tilde{\psi}_{r\theta,j}^- + \frac{1}{2} \frac{\partial(\tilde{\psi}_{r\theta,j}^+ - \tilde{\psi}_{r\theta,j}^-)}{\partial r}\end{aligned}\tag{B.1}$$

where for $\tilde{\phi}_j$ and $\tilde{\psi}_{z,j}$ the order of the transform should be equal to 1, for $\tilde{\psi}_{r\theta,j}^+$ to 0 and for $\tilde{\psi}_{r\theta,j}^-$ to 2. The relative inverse Hankel transform are given as:

$$\begin{aligned}\tilde{\phi}_j &= \int_0^\infty \xi \tilde{\phi}_j^{H_1} J_1(\xi r) d\xi \\ \tilde{\psi}_{r\theta,j}^+ &= \int_0^\infty \xi \tilde{\psi}_{r\theta,j}^{+H_0} J_0(\xi r) d\xi \\ \tilde{\psi}_{r\theta,j}^- &= \int_0^\infty \xi \tilde{\psi}_{r\theta,j}^{-H_2} J_2(\xi r) d\xi \\ \tilde{\psi}_{z,j} &= \int_0^\infty \xi \tilde{\psi}_{z,j}^{H_1} J_1(\xi r) d\xi\end{aligned}\tag{B.2}$$

In the following two sections the analysis is differentiated for the vertical (\tilde{u}_z) and the transversal displacement (\tilde{u}_r).

B.1 Vertical displacement

The vertical displacement $\tilde{u}_{z,j}$ is then expressed in terms of potentials as:

$$\tilde{u}_{z,j} = \frac{\partial \tilde{\phi}_j}{\partial z} - \frac{1}{r} \tilde{\psi}_{r\theta,j}^- + \frac{1}{2} \frac{\partial (\tilde{\psi}_{r\theta,j}^+ - \tilde{\psi}_{r\theta,j}^-)}{\partial r}\tag{B.3}$$

In order to define the order of the Bessel function needed for the transformation, it is necessary to evaluate Equation B.3 using the Equations B.2. Each member has its own relative Bessel function, the goal is to find out which is the order of the Bessel function of the final vertical displacement. Considering the first term, it is possible to find that:

$$\frac{\partial \tilde{\phi}_j}{\partial z} = \frac{\partial}{\partial z} \int_0^\infty \xi \tilde{\phi}_j^{H_1} J_1(\xi r) d\xi\tag{B.4}$$

Since the differentiation along the vertical direction does not modify the order of the Bessel function, the transform stands with the order 1. The second and the third terms are combined in order to analyse at the same time the potential $\tilde{\psi}_{r\theta,j}^-$. From this partial combination, it is possible to obtain the following:

$$-\frac{1}{r} \tilde{\psi}_{r\theta,j}^- - \frac{1}{2} \frac{\partial \tilde{\psi}_{r\theta,j}^-}{\partial r} = \int_0^\infty \left(-\frac{1}{r} \tilde{\psi}_{r\theta,j}^{-H_2} J_2(r\xi) - \frac{1}{2} \frac{\partial \tilde{\psi}_{r\theta,j}^{-H_2}}{\partial r} J_2(r\xi) \right) \xi d\xi\tag{B.5}$$

The compatibility equation of the potentials states that [40]:

$$\frac{1}{r}\tilde{\psi}_{r\theta,j}^{-H_2} + \frac{1}{2}\frac{\partial}{\partial r}(\tilde{\psi}_{r\theta,j}^{+H_0} + \tilde{\psi}_{r\theta,j}^{-H_2}) + \frac{\partial}{\partial z}\tilde{\psi}_z^{H_1} = 0 \quad (\text{B.6})$$

which can be rewritten as:

$$\frac{1}{r}\tilde{\psi}_{r\theta,j}^{-H_2} + \frac{1}{2}\frac{\partial}{\partial r}\tilde{\psi}_{r\theta,j}^{-H_2} = -\frac{1}{2}\frac{\partial}{\partial r}\tilde{\psi}_{r\theta,j}^{+H_0} - \frac{\partial}{\partial z}\tilde{\psi}_z^{H_1} \quad (\text{B.7})$$

Equation B.5 is then expressed as:

$$\int_0^\infty \left(+\frac{1}{2}\frac{\partial}{\partial r}\tilde{\psi}_{r\theta,j}^{+H_0} J_0(r\xi) + \frac{\partial}{\partial z}\tilde{\psi}_{r\theta,j}^{H_1} J_1(r\xi) \right) \xi d\xi \quad (\text{B.8})$$

In Equation B.8, the second term of the integral is again differentiated along the vertical direction and therefore the order of the Bessel function is conserved and it is equal to 1. The first term can be recombined with the first addend of the third term of Equation B.3 in order to analyse the potential $\tilde{\psi}_{r\theta,j}^+$ as following:

$$\frac{1}{2}\frac{\partial}{\partial r}\tilde{\psi}_{r\theta,j}^+ + \frac{1}{2}\frac{\partial}{\partial r}\tilde{\psi}_{r\theta,j}^+ = \int_0^\infty \frac{\partial}{\partial r}\tilde{\psi}_{r\theta,j}^{+H_0} J_0(r\xi) \xi d\xi \quad (\text{B.9})$$

By recalling, the differentiation rule of the Bessel functions:

$$\frac{\partial}{\partial r}J_0(r) = -J_1(r) \quad (\text{B.10})$$

A differentiation along the radial coordinate provokes an increase of the order of the of the Bessel function by a unit. Also for this term, the order of the relative Bessel function is therefore equal to 1. In conclusion, as derived, it is possible to conclude that, for a vertical displacement measurement generated by a horizontally polarized source, the order of the Bessel function of the Hankel transform needs to be equal to 1.

B.2 Transversal displacement

As presented by [40], the order of the Bessel function for the transversal displacement is not unique. Both the orders 0 and 2 are present. Nevertheless, in this particular situation, some qualitative conclusions can be drawn starting from the equations presented by [40]. In principle, when the interest is focus on the transversal

displacement generated by cross-line sweeps of the source, the horizontal longitudinal displacement is equal to 0, since only pure shear surface waves are propagating (Love waves). In this setting, it is possible to state that:

$$\tilde{u}_{r,j} + \tilde{u}_{\theta,j} = 0 + \tilde{u}_{\theta,j} = \tilde{u}_{\theta,j} \quad (\text{B.11})$$

The expression of the horizontal displacements are reported by [40]:

$$\begin{aligned} \tilde{u}_{r,j} &= \frac{1}{2} \int_0^\infty \xi \left\{ \left[\xi \tilde{\phi}_j^{H_1} + \xi \tilde{\psi}_{z,j}^{H_1} - \frac{2}{\xi} \frac{\partial^2}{\partial z^2} \tilde{\psi}_{z,j}^{H_1} - \frac{\partial}{\partial z} \tilde{\psi}_{r\theta,j}^{-H_2} \right] J_0(\xi r) \right. \\ &\quad \left. + \left[-\xi \tilde{\phi}_j^{H_1} + \xi \tilde{\psi}_{z,j}^{H_1} + \frac{\partial}{\partial z} \tilde{\psi}_{r\theta,j}^{-H_2} \right] J_2(\xi r) \right\} d\xi \\ \tilde{u}_{\theta,j} &= \frac{1}{2} \int_0^\infty \xi \left\{ - \left[\xi \tilde{\phi}_j^{H_1} + \xi \tilde{\psi}_{z,j}^{H_1} - \frac{2}{\xi} \frac{\partial^2}{\partial z^2} \tilde{\psi}_{z,j}^{H_1} - \frac{\partial}{\partial z} \tilde{\psi}_{r\theta,j}^{-H_2} \right] J_0(\xi r) \right. \\ &\quad \left. + \left[-\xi \tilde{\phi}_j^{H_1} + \xi \tilde{\psi}_{z,j}^{H_1} + \frac{\partial}{\partial z} \tilde{\psi}_{r\theta,j}^{-H_2} \right] J_2(\xi r) \right\} d\xi \end{aligned} \quad (\text{B.12})$$

Combining Equation B.11 with Equation B.12, it can be found that:

$$\tilde{u}_{\theta,j} = \frac{1}{2} \int_0^\infty \xi \left[-\xi \tilde{\phi}_j^{H_1} + \xi \tilde{\psi}_{z,j}^{H_1} + \frac{\partial}{\partial z} \tilde{\psi}_{r\theta,j}^{-H_2} \right] J_2(\xi r) d\xi \quad (\text{B.13})$$

Therefore, it is possible to state that, for pure Love waves, it is necessary to use a second order Bessel function in the Hankel transformation for transversal displacements.

Moreover, it has been found that the the order of the Bessel function does not affect the amount of the material damping (i.e. the width of the peaks) in the f-k domain response. Further analysis should be carried out to check this result with different datasets. In conclusion, it is possible to observe that the wave potentials considered in this analysis are plane potentials which intrinsically do not include the geometric attenuation. This shows that the results of the Hankel transform do not include the geometric spreading but only the material damping.

Appendix C

Rectangular Windowing

This Appendix shows the derivations needed for computing the response of the theoretical model while a boxcar window is applied in the space domain.

In order to simulate the limited amount of receivers of the measured experiment and evaluate the effects of this truncation on the width of the peaks in the f-k domain, a boxcar window is introduced in the forward model in the space domain as following:

$$\tilde{f}(\kappa_1, x_3 = 0, \omega) = \int_{-\infty}^{\infty} \tilde{f}(\kappa_1, x_3 = 0, \omega) e^{i\kappa_1 x_1} [H(x_1 - x_a) - H(x_1 - x_b)] dx_1 \quad (\text{C.1})$$

By defining, $f(x_1) = \tilde{f}(\kappa_1, x_3 = 0, \omega) e^{i\kappa_1 x_1}$ and $g(x_1) = [H(x_1 - x_a) - H(x_1 - x_b)]$, it is possible to rewrite Equation C.1 as:

$$\tilde{f}(\kappa_1) = \int_{-\infty}^{\infty} f(x_1) \times g(x_1) dx_1 \quad (\text{C.2})$$

where, the function $g(x)$ is defined as the rectangular/boxcar function which is equal to 1 within the measurement window (from x_a to x_b) and equal to 0 otherwise. It is now possible to recall the convolution property for which a multiplication in the space domain corresponds to a convolution in the wavenumber domain:

$$f(x_1) \times g(x_1) = F(\kappa_1) * G(\kappa_1) \quad (\text{C.3})$$

Where the convolution integral is defined as:

$$F(\kappa_1) * G(\kappa_1) = \int_{-\infty}^{\infty} F(\bar{\kappa}_1 - \kappa_1)G(\bar{\kappa}_1)d\kappa_1 = \int_{-\infty}^{\infty} F(\bar{\kappa}_1)G(\bar{\kappa}_1 - \kappa_1)d\kappa_1 \quad (C.4)$$

In the present research, the wavenumber transform of the first function is response in the f-k domain of the layered halfspace computed at $x_3 = 0$ and it is denominated as $\tilde{u}(\kappa_1, x_3 = 0, \omega)$. While, the boxcar function in the wavenumber domain is the sinc function:

$$G(k_1) = \int_{-\infty}^{\infty} g(x_1) = \frac{\sin(\kappa_1 L)}{\kappa_1 L} = \text{sinc}(\kappa_1 L) \quad (C.5)$$

Equivalently, since the measurement window of the present experiment goes from the position of the source $x_a = 0$ and $b = L$, the transform of the boxcar window can be defined as:

$$G(k_1) = \int_{-\infty}^{\infty} g(x_1)e^{-i\kappa_1 x_1} dx_1 = \int_0^L e^{-i\kappa_1 x_1} dx_1 = -\frac{1}{i\kappa_1} [e^{-i\kappa_1 L} - 1] \quad (C.6)$$

Therefore, it is possible to determine the convolution integral in the following form:

$$F(k_1) * G(k_1) = \int_{-\infty}^{\infty} \tilde{u}(\bar{\kappa}_1, x_3 = 0, \omega) \frac{\sin[(\kappa_1 - \bar{\kappa}_1)L]}{(\kappa_1 - \bar{\kappa}_1)L} d\bar{\kappa}_1 \quad (C.7)$$

Finally, the convolution can be also summarized in the following form:

$$\tilde{u}(k_1, x_3 = 0, \omega) *_{k_1} \frac{\sin(k_1 L)}{k_1 L} \quad (C.8)$$

The kernel of the integral is the final response in the f-k domain subjected to the rectangular window. This convolution integral provokes a widening of the peaks of the original response $\tilde{u}(k_1, x_3 = 0, \omega)$ simulating the effect of limitation of the receivers. The present analysis is used in Section 6.5 in order to give an estimation of the overestimation of the material damping profile due to the aforementioned widening of the peaks.

Bibliography

- [1] J.D. Achenbach. *Wave Propagation in Elastic Solids*. North-Holland Publishing Company/American Elsevier, 1973.
- [2] U.S. Energy Information Administration. International energy outlook 2017. Technical report, September 2017.
- [3] Siemens AG. Offshore brochure. Technical report, 2016.
- [4] Keiiti Aki and Paul G. Richards. *Quantitative Seismology*. University Science Books, 2 edition, 2002.
- [5] Michael Armstrong. Seismic inversion for identification of soil stiffness and damping for offshore wind turbines, August 2016.
- [6] A.K. Ashmawy, R. Salgado, S. Guha, and V.P. Drnevich. Soil damping and its use in dynamic analyses. *1995 - Third International Conference on Recent Advances in Geotechnical Earthquake Engineering Soil Dynamics*, 1995.
- [7] S.A. Badsar, Mattias Schevenels, Wim Haegeman, and Geert Degrande. Determination of the material damping ratio in the soil from sasw tests using the half-power bandwidth method. *Geophysical Journal International*, 182(3):1493–1508, 2010.
- [8] Ingmar Bolderink. Identification of dynamic soil properties relevant for offshore wind turbines through full waveform inversion of in situ measured seismic data. Msc thesis report, September 2015.
- [9] Jeffrey Brooks and David Hibler. The genetic flock algorithm. *Procedia Computer Science*, 20:71 – 76, 2013.

- [10] José M Carcione, Dan Kosloff, and Ronnie Kosloff. Wave propagation simulation in a linear viscoelastic medium. *Geophysical Journal International*, 95(3):597–611, 1988.
- [11] GWEC Global Wind Energy Council. Global wind 2016 report. Technical report, 2016.
- [12] World Energy Council. World energy resources wind — 2016. Technical report, October 2016.
- [13] Corine de Winter. Inversion of near surface seismic measurements to estimate soil stiffness relevant for offshore wind turbines. Msc thesis report, October 2014.
- [14] Hefeng Dong, Jens M. Hovem, and Prof. *Interface Waves, Waves in Fluids and Solids*. InTech, 2011.
- [15] Sebastiano Foti, Carlo G. Lai, Glenn J. Rix, and Claudio Strobbia. *Surface Wave Methods for Near-Surface Site Characterization*. CRC Press, 2015.
- [16] Lingli Gao, Jianghai Xia, Yudi Pan, and Yixian Xu. Reason and condition for mode kissing in masw method. *Pure and Applied Geophysics*, 173(5):1627–1638, 2016.
- [17] Paul Holscher. *Lecture Notes: Soil dynamics in urban areas*, April 9, 2016.
- [18] K. Ishihara. *Soil Behaviour in Earthquake Geotechnics*. 1996.
- [19] Z. Khan, M.H. El Naggar, and G. Cascante. Frequency dependent dynamic properties from resonant column and cyclic triaxial tests. *Journal of the Franklin Institute*, 348(7):1363 – 1376, 2011.
- [20] Z. Khan, M.H. El Naggar, and G. Cascante. Frequency dependent dynamic properties from resonant column and cyclic triaxial tests. *Journal of the Franklin Institute*, 348(7):1363 – 1376, 2011.
- [21] Steven L. Kramer. *Geotechnical Earthquake Engineering*. Prentice-Hall, Inc, 1996.
- [22] Peter Kravanja and Marc Van Barel. *Computing the Zeros of Analytic Functions*. 03 2000.
- [23] Eln sta lafsdttir. Multichannel analysis of surface waves for assessing soil stiffness. Msc thesis report, January 2016.

- [24] Carlo G Lai and Glenn J Rix. Solution of the rayleigh eigenproblem in viscoelastic media. *Bulletin of the Seismological Society of America*, 92(6):2297–2309, 2002.
- [25] C.G. Lai and A.G. zcebe. Non-conventional lab and field methods for measuring frequency-dependent low-strain parameters of soil dynamic behavior. *Soil Dynamics and Earthquake Engineering*, 91:72 – 86, 2016.
- [26] Adam Lichtl and Stephen Jones. Full scale simulation of spacex’s mars rocket engine. 14:00-24:00 min, 2015.
- [27] Meei-Ling Lin, Tsan-Hwei Huang, and Jeng-Chie You. The effects of frequency on damping properties of sand. *Soil Dynamics and Earthquake Engineering*, 15(4):269 – 278, 1996.
- [28] Hsi-Ping Liu, Don L. Anderson, and Hiroo Kanamori. Velocity dispersion due to anelasticity; implications for seismology and mantle composition. *Geophysical Journal International*, 47(1):41–58, 1976.
- [29] Andrei Metrikine. *Lecture notes: Structural Dynamics - CIE 4140 Structural Mechanics*, 2017.
- [30] Amr S Misbah and Claudio L Strobbia. Joint estimation of modal attenuation and velocity from multichannel surface wave data. *Geophysics*, 79(3):EN25–EN38, 2014.
- [31] A.N Norris and B.K. Sinha. The speed of a wave along a fluid/solid interface in the presence of anisotropy and prestress. *1995 Acoustical Society of America*, 1995.
- [32] TKI Wind op Zee. Cost reduction options for offshore wind in the netherlands fid 2010-2020. Technical report, October 2015.
- [33] C.B. Park, Miller R.D., and J. Xia. Multichannel analysis of surface waves, May-June 1999.
- [34] Choon Park, R D. Miller, Nils Ryden, Jianghai Xia, and Julian Ivanov. Combined use of active and passive surface waves. 10:323–334, 09 2005.
- [35] Dieter Rauch. *Seismic Interface Waves in Costal Waters: A Review*. SACLANT ASW Research Centre, 1980.
- [36] Nick Rawlinson. *Lecture notes: Surface waves and dispersion*, 2007.

- [37] Daniel Trad, Tadeusz Ulrych, and Mauricio Sacchi. Latest views of the sparse radon transform. *GEOPHYSICS*, 68(1):386–399, 2003.
- [38] Karel N. van Dalen. *Lecture Notes CIE5340 Soil Dynamics, part B: Body waves in an elastic continuum and Rayleigh waves at the free surface*, 2015. June 2015.
- [39] M. Vanneste, C. Madshus, V. L. Socco, M. Maraschini, P. M. Sparrevik, H. Westerdahl, K. Duffaut, E. Skomedal, and T. I. Bjørnar. On the use of the norwegian geotechnical institute's prototype seabed-coupled shear wave vibrator for shallow soil characterization - i. acquisition and processing of multimodal surface waves. *Geophysical Journal International*, 185(1):221–236, 2011.
- [40] A.V. Vostroukhov, S.N. Verichev, A.W.M. Kok, and C. Esveld. Steady-state response of a stratified half-space subjected to a horizontal arbitrary buried uniform load applied at a circular area. *Soil Dynamics and Earthquake Engineering*, 24(6):449 – 459, 2004.

